Title

Structural and Compositional Control of Steel and Aluminum Alloys via Laser Powder Bed Fusion Processing

Author

Fields, Brandon

Publication Date

2024

UNIVERSITY OF CALIFORNIA, IRVINE

Structural and Compositional Control of Steel and Aluminum Alloys via Laser Powder Bed Fusion Processing

DISSERTATION

submitted in partial satisfaction of the requirements
for the degree of

DOCTOR OF PHILOSOPHY
in Materials Science and Engineering

by

Brandon Fields

Dissertation Committee:
Professor Lorenzo Valdevit, Chair
Distinguished Professor Diran Apelian
Distinguished Professor Emeritus Enrique Lavernia

2024

DEDICATION

To my family and friends.

My father Mark, mother Christine, & sister Catherine. Without your unwavering love & support, we would not be able to accomplish this.

My reflections and commitment

Doubt stopped more dreams than failure ever did.

Don’t let the perfect be the enemy of the good.

To achieve something you have never done, you must do something you never did.

Actions speak louder than words.

And an inspiration

“When something is important enough, you do it even if the odds aren’t in your favor.”

(Elon Musk)

TABLE OF CONTENTS

LIST OF FIGURES

LIST OF TABLES

ACKNOWLEDGMENTS

I would like to acknowledge and thank my advisors, Dr. Lorenzo Valdevit and Dr. Diran Apelian. I first joined Lorenzo's group in 2019 which was a very exciting time. Shortly after joining, the pandemic started which was difficult for everyone. This combined with my background in physics rather than materials engineering caused me difficulties in making research progress in the early stage of my PhD, as learning through hands on work was unavailable. Once in-person research started up again, there were many times I was unsure which direction to pursue. Lorenzo was always there to guide me and work with me step-by-step throughout the process, so that I could grow and learn how to become a better scientist, engineer, and professional. Shortly after joining UCI, I became co-advised by Diran, who additionally facilitated me to reach my full potential. Observing how Diran led the ACRC helped me understand which aspects of research are truly impactful, and how to translate lab research towards innovative engineering developments. Having full support from both Lorenzo and Diran enabled me to make significant research progress, but more importantly develop a mindset that is focused on the impact of the many years beyond my PhD. Thank you both for believing in me and helping provide the resources to enable me to accomplish all that we've done as a team in the past years. I view both Lorenzo and Diran not only as great advisors, but as mentors. The most valuable insights I have gained throughout my PhD are not solely about materials science, but additionally insights of how to conduct oneself as a leader, as a professional, as a hardworking creative engineer, and most importantly as a contributing teammate to a successful team.

In addition, many thanks to Dr. Enrique Lavernia on my dissertation committee, for providing valuable feedback on my research throughout the years. You have always been supportive through constructive criticism and encouragement in the direction I am going. I have made many friends with students in your group; and I have noticed their joy for materials science and engineering in general, which must mean that you have been very valuable to them as a mentor.

Sincere gratitude to Dr. Benjamin MacDonald and Dr. Julia Purstl for guiding me through different stages of my PhD. You both were always very enthusiastic about helping me make progress and see problems from multiple angles, even when I was persistent on going in my predetermined direction. You both helped me in many areas of research, experimentation, analysis, and writing. Your help and support were truly needed and is appreciated.

To all the students in the Valdevit and Apelian research groups, thank you for making my time here meaningful beyond research. Everyone in both groups: Mahsa Amiri, Jungyun Lim, Kate Ainger, Carl Soderhjelm, Vivek Verma, Calvin Belcher, Sakshi Bajpai, Shri Shankar, Cheolmin Ahn, Raquel Jaime, Kentaro Lunn, Jack Webster, Matt Foong, have all helped in many different aspects of my time here, and you all have helped me learn how to be a good teammate. Particularly, thank you to Mahsa Amiri who spent many hours in the TEM to help me get crucial data to get my first papers published.

I would also like to thank many staff: Darryl Mac, Don Fruta, Amy Ricks, Desiree Rios, Vivianna Saadalla, and the IMRI staff who have all helped me with many different aspects of my research regarding equipment training and logistics. A special thank you to Ben Dolan who first trained me on the SLM printer which made all of this research possible, and Mingjie Xu who spent many hours with me on the SEM. Ben is a wizard with all of the equipment in IDMI, and Mingjie helped save me days of SEM time with his expertise.

This work was partly supported by the Office of Naval Research (Program Manager: J. Wolk, Grant No. N00014-21-1-2570). All microstructural characterization work was performed at the UC Irvine Materials Research Institute (IMRI), using instrumentation funded in part by the

National Science Foundation Center for Chemistry at the Space-Time Limit (CHE-082913). In addition, we acknowledge the collaboration with Buehler and Evident Scientific (Olympus) for their support of the Buehler Center of Excellence and the Olympus microscopy suite at the Advanced Casting Research Center (ACRC).

VITA

Brandon Fields

Education

University of California, Irvine	June 2024
Ph.D., Materials Science and Engineering	GPA: 3.95
University of California, Irvine	June 2020
M.S., Materials Science and Engineering	GPA: 3.95
California Polytechnic State University, San Luis Obispo	June 2019
B.S., Physics	GPA: 3.93

Peer-Reviewed Publications.

1. B. Fields, M. Amiri, B. MacDonald, J. Purstl, C. Dai, X. Li, D. Apelian, L. Valdevit. Investigation of an additively manufactured modified aluminum 7068 alloy: *Mat Sci & Eng A*. (2024) 145901

2. B. Fields, M. Amiri, J. Lim, J. Purstl, M. Begley, D. Apelian, L. Valdevit. Microstructural Control of a Multi-Phase PH Steel Printed with Laser Powder Bed Fusion. *Adv. Mater. Technol.* (2024) 2301037

3. B. Fields, J. Purstl, D. Apelian, L. Valdevit. Controlling Phase Evolution of 17-4PH steel in Laser Powder Bed Fusion. *In-Progress*.

4. B. MacDonald, B. Zheng, B. Fields, X. Wang, S. Jiang, P. Cao, L. Valdevit, E. Lavernia, J. Schoenung. Influence of co-deposition strategy on the mechanical behavior of additively manufactured functionally integrated materials. *Additive Manufacturing* (2023) 103328

5. Y. Guo, M. Rosa, M. Gupta, B. Dolan, B. Fields, L. Valdevit, M. Ruzzene. Minimal Surface-Based Materials for Topological Elastic Wave Guiding. *Adv. Func. Mater.* (2022) 2204122

6. V. Perricone, B. Fields, D. Kisailius, et. al., The echinoid–Voronoi pattern: a functional geometry to sustain applied loads. *In-Progress.*

7. J. Purstl, B. Fields, D. Apelian, L. Valdevit, et. al. Processing and Mechanical Characterization of Thin-Wall Features in LPBF: The role of build orientation in LPBF of 17-4 Stainless Steel. *In-Progress*

Oral Presentations

1. B. Fields, M. Amiri, B. MacDonald, J. Purstl, C. Dai, X. Li, D. Apelian, L. Valdevit. Investigation of an additively manufactured modified aluminum 7068 alloy: *TMS 2022*, Anaheim, CA, USA

2. B. Fields, M. Amiri, B. MacDonald, J. Purstl, C. Dai, X. Li, D. Apelian, L. Valdevit. Investigation of an additively manufactured modified aluminum 7068 alloy: *PowderMet* 2022, Portland, OR, USA.

3. B. Fields, M. Amiri, J. Lim, J. Purstl, M. Begley, D. Apelian, L. Valdevit. Microstructural Control of a Multi-Phase PH Steel Printed with Laser Powder Bed Fusion. *TMS 2023*, San Diego, CA, USA.

4. B. Fields, M. Amiri, J. Lim, J. Purstl, M. Begley, D. Apelian, L. Valdevit. Microstructural Control of a Multi-Phase PH Steel Printed with Laser Powder Bed Fusion. *PowderMet 2023*, Las Vegas, NV, USA.

ABSTRACT OF THE DISSERTATION

Structural and Compositional Control of Steel and Aluminum Alloys via Laser Powder Bed Fusion Processing

by

Brandon Fields

Doctor of Philosophy in Materials Science and Engineering

University of California, Irvine, 2024

Professor Lorenzo Valdevit, Chair

Additive Manufacturing (AM) is an emerging disruptive technology that is rapidly expanding from its initial purpose of rapid prototyping towards the production of high-quality final products. Laser powder bed fusion (LPBF) has emerged as a market leader for producing small and medium sized parts among the various classes of metal AM. While LPBF holds much promise in multiple industries, many challenges remain, particularly related to the structural evolution of AM materials during printing and the resulting material properties in the final product. A material system that has primarily defied printability is the 7xxx family of aluminum alloys. Here, we thoroughly investigate a chemically modified nanostructured Al-7068 alloy and unveil the processing-microstructure-mechanical properties relations in LPBF that underscore its performance relative to conventional (wrought) Al-7xxx alloys. Another critical challenge related to AM processing in general (and LBPF in particular) is the complex and unique thermal history experienced by each localized tiny volume in the part domain, which often results in poorly controlled heterogeneous and anisotropic microstructures, and hence properties for LBPF components. At the same time, this challenge presents an opportunity whereby one could locally control the processing parameters to induce controlled and complex temperature histories within a single part, locally tuning the microstructure and effectively resulting in the fabrication of in-situ metal-metal composites. Here we demonstrate this understanding and control in a dual-phase stainless steel (17-4 PH), quantify the differences in mechanical properties between the available microstructures, and determine the ability and scale of microstructural control. Collectively, this work paves the ground for developing superior metallic alloys for LPBF, whereby microstructure and properties are carefully controlled through the print.

Executive Summary

Introduction

Additive Manufacturing (AM), colloquially known as 3D printing, is a developing technology that gained commercial relevance to prototype new part designs with unprecedented geometric flexibility rapidly. Today, after many engineering and material breakthroughs, AM is more often being utilized in the manufacturing of advanced final products[1], ranging from custom-printed titanium implants[2] to rocket-nozzle-tip fuel injectors[2]. Many of these technological and manufacturing advancements coincide with developing new and improved process-specific materials. Thus, additional alloy design opportunities exist through modifying composition, controlling phase evolution, and optimizing specific process controls unique to these advanced additive manufacturing processes.

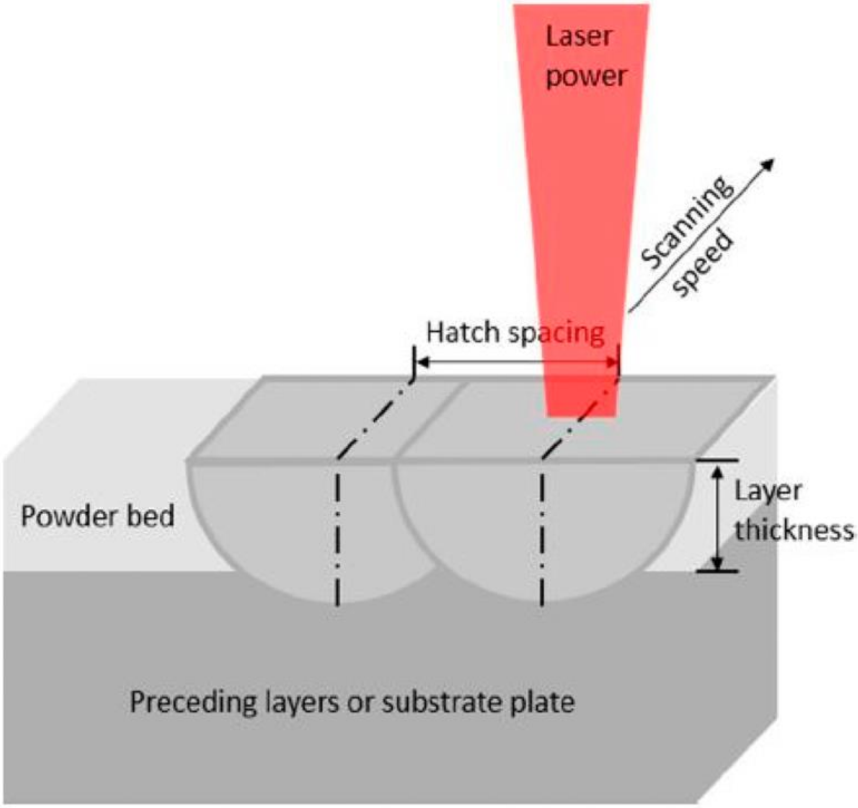

Figure 1. The laser powder bed fusion process and the most critical process parameters, including laser power, scan speed, layer thickness, and hatch spacing.[3]

Metal AM techniques include binder jetting[4], electron beam melting (EBM)[5], and laser powder bed fusion (LPBF) for small part production, wire arc additive manufacturing (WAAM)[6], direct energy deposition (DED)[7], and cold spray[8] for larger components and structural repairs. LPBF has emerged as the current market leader throughout the development of these metal AM techniques. LPBF is a process in which a thin layer of powder (20-100μm) is deposited onto a build substrate before a laser scans and melts/solidifies according to a 2D slice of a 3D part. Another layer of powder is deposited over the previous layer, and this process repeats when printing the entire 3D part. This process across a 2D layer, with the most critical printing parameters, is depicted in Figure 1.

Thanks to the combination of acceptable part resolution, high print density, high surface quality, and operating simplicity (no need for a vacuum environment or significant substrate heating), LPBF is poised to continue its lead in AM market penetration. Further innovations such as multiple lasers, larger build platforms, and most substantially improved LPBF process-specific materials will continue to provide LPBF with many scalability advantages over comparable metal printing processes[1,9]. Figure 2 emphasizes how AM will continue to be utilized across many sectors. With applications in medical, dental, industrial, automotive, and aerospace all being more prevalent than consumer products, it is evident that 3D printing overall has primary application in advanced manufacturing and no longer primarily for prototyping.

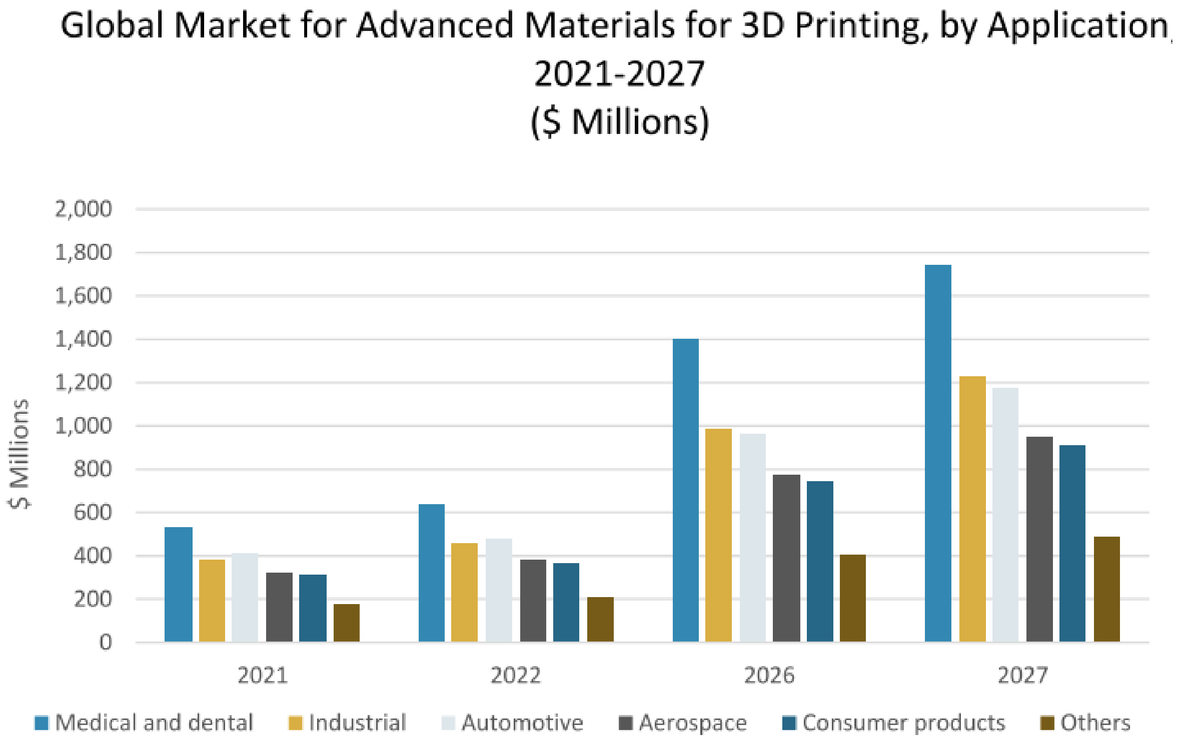

Figure 2. The primary industries comprising the advanced 3D printing market.[10]

In addition to the geometric design flexibility enabled, AM has a significant impact on the global supply chain through decreasing the overall capital expenditure from ideation to end-use, illustrated in Figure 3. Regarding the manufacturing of metallic components, this primarily consists of the elimination of costly tooling to manufacture parts. Additionally, pre-assembled components are printed directly, lower minimum order quantities are needed for prototypes, and end-users can outsource less frequently due to the ability to purchase lower-cost manufacturing equipment themselves[1,10].

With such a large impact and disruption across many sectors and their supply chains, it is important for materials scientists to recognize what material issues might limit the future applicability and growth of LPBF. Applications in this wide range of sectors demand a wide range of available materials. Many conventional alloys such as Al-Si alloys, 300 series stainless steels, Inconel, and Ti-6Al-4V are all commonly utilized materials throughout the global markets and are readily available for LPBF use[11,12]. However, this is not the case for all desired LPBF materials, as many alloys are subject to LPBF specific processing issues and therefore not commercially deployed to their full capacity. Therefore, these alloys must be either modified or completely redesigned for LPBF processing specifically. The purpose of this thesis is to illustrate: (1) How alloys can be designed specifically for the LPBF process, (2) How conventional material structures and properties can be tailored through detailed understanding of LBPF process control, and (3) How LPBF enables novel microstructures only possible due to the unique solidification of the LPBF process.

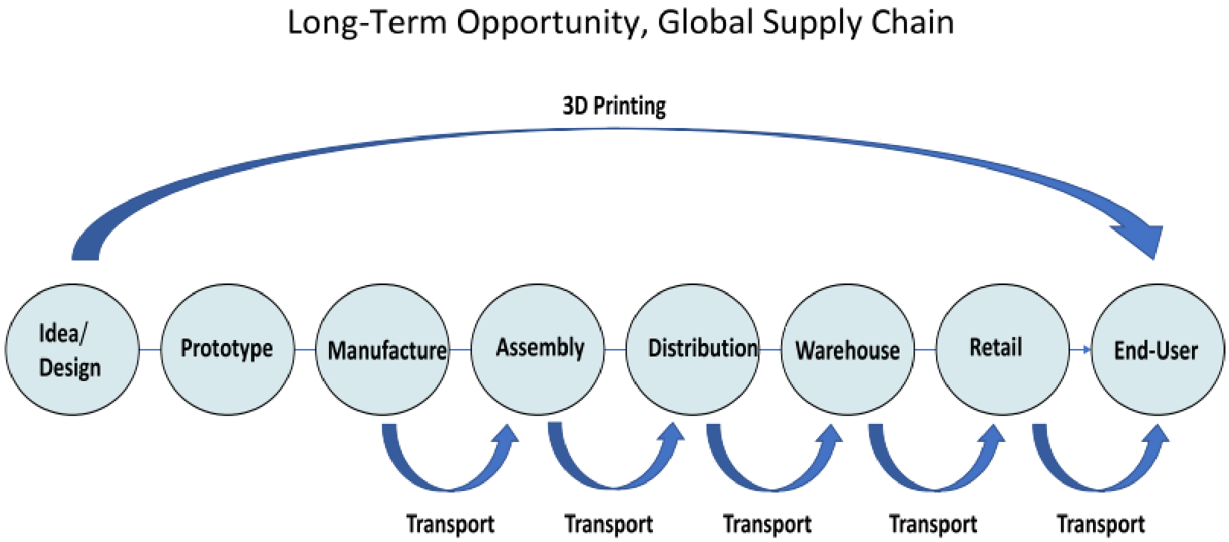

Figure 3. Traditional manufacturing supply chain, with multiple intermediary steps between ideation and end-use, compared to 3D printing.[10]

Alloy Systems and Experimental Methodology

This thesis investigates two alloys which are of the upmost importance for LPBF to be utilized at its full capacity. These alloys are Al-7068 and 17-4PH stainless steel, each with their own specific issues regarding LPBF processing. These are two notable alloys due to their excellent mechanical properties, cost-effectiveness, and use in various engineering applications and industrial processes. With Al-7xxx and 17-4PH steel already employed across aerospace, automotive, biomedical, and industrial manufacturing, LPBF can only be fully utilized if these alloys are capable of being processed straightforwardly and can meet and exceed the standards of their conventional counterparts. Thus, it is required that these alloys be redesigned and modified specifically for LPBF. Additionally, fine control of the LPBF process must be understood in detail to optimize the microstructural evolution of these materials throughout processing.

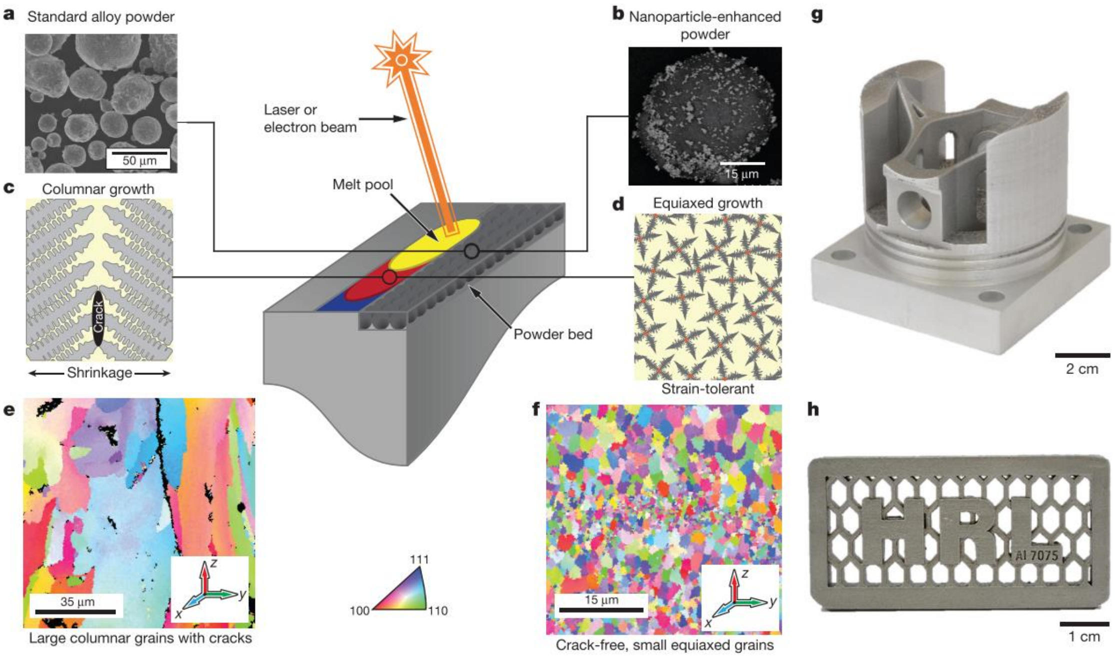

Figure 4. Challenges with printing Al-7xxx alloys (a,c,e) without inoculants leading to hot cracking with standard feestock Al-7075, compared to (b,d,f) Zr-nanoparticle enhanced powder altering nucleation from columnar to equiaxed.[13,14]

Chapter 1 focuses on the two fundamental challenges affecting printability of high-strength aluminum alloys: (i) the prevalence of hot cracking during solidification and (ii) the significant evaporation of the major strengthening elements during processing. Many structural alloys, such as nickel superalloys (e.g., Inconel-718), titanium alloys (e.g., Ti-6Al-4V), and stainless steels (e.g., SS-316), show a significant improvement in mechanical properties when printed via LPBF in comparison to their wrought counterparts[15–19]. This is due to the high cooling rates experienced in LPBF, ranging from 10^4-10^7 K/s, generally resulting in finer microstructures[20,21]. Conversely, LPBF-processed high-strength 6xxx and 7xxx series aluminum alloys consistently show a significant decrease in mechanical properties[14,22–26]. A limited number of successful LPBF-processed high-strength Al alloys have been reported. Early literature reviews primarily pertained to the Al-Si based alloy system, with only 11 of the 310 articles reviewed in ref [27], 2 of the 236 articles reviewed in ref [28], and 3 of the 168 articles reviewed in ref [29] focusing on 6xxx and 7xxx series Al alloys. The ubiquitous reporting of Al-Si alloys in the literature as well as the vast range of commercial applications of these alloys stem from their resistance to hot cracking, attributed to the narrow solidification range of the eutectic alloy and the low viscosity of the melt, which allows for inter-dendritic/cellular liquid flow[30–34]. By contrast, hot cracking occurs during rapid solidification of 6xxx and 7xxx series aluminum due to the large solidification range, the high viscosity of the inter-dendritic fluid, and the high thermal contraction during the latter stages of solidification[14,35,36].

However, recently, more work on the processability of high-strength aluminum has been conducted, utilizing inoculants to restrict columnar grain growth and, therefore, reduce hot-cracking susceptibility[37–51]. While hot cracking of high-strength Al alloys is also observed during welding, it is greatly exacerbated in LPBF due to the significantly higher cooling rates and the directionality of thermal gradients from the build substrate towards the laser source, leading to cracks between contracting large columnar grains during cooling[20]. This hot cracking mechanism is depicted in Figure 4a, 4c, and 4e; with the effect of inoculants altering the solidification mode shown in 4b, 4d, and 4f.

Additionally, Chapter 1 investigates the other significant issue of the unknown effects of printing conditions on the final as-printed chemistry of Al-7xxx. The Al-7xxx series are all precipitation strengthened alloys by Mg and Zn precipitates which respectively have boiling points of 1091°C and 901°C, nearly 1000°C lower than Al. The LPBF Al-7xxx literature has reported volatilities from 15% upwards to 50% of Mg and Zn in the as-printed condition[31,52], which from a manufacturing quality and a material property standpoint is an unacceptable variance. The fundamental physics regarding how much energy is being input into the material during the printing process, leading to changing amounts of vaporization and final composition needs to be carefully understood and meticulously controlled. Just a few wt% difference of Mg and Zn can drastically change the mechanical properties of this alloy system.

Chapter 1 addresses both issues by investigating a novel Al-7068 alloy, with (i) TiC nanoparticle inoculants added to the feedstock powders and (ii) increased amounts of Mg and Zn in expectation of significant vaporization. The printing parameters are systematically varied to measure how both composition and porosity change. It is determined under what conditions the alloy is optimally dense, has minimal defects, and has composition that falls in the required range. Key methodologies and techniques used are mass spectrometry to systematically quantity chemistry, microscopy and CT scanning to quantify porosity, mechanical testing, and scanning and transmission electron microscopy. Analytical models regarding evaporation occurring in the melt pool and microstructural strengthening mechanisms are both examined and compared with experimental observation. These models are examined to physically understand what mechanisms are dominating the evaporation and strengthening behavior, as well as a future tool for aluminum alloy development.

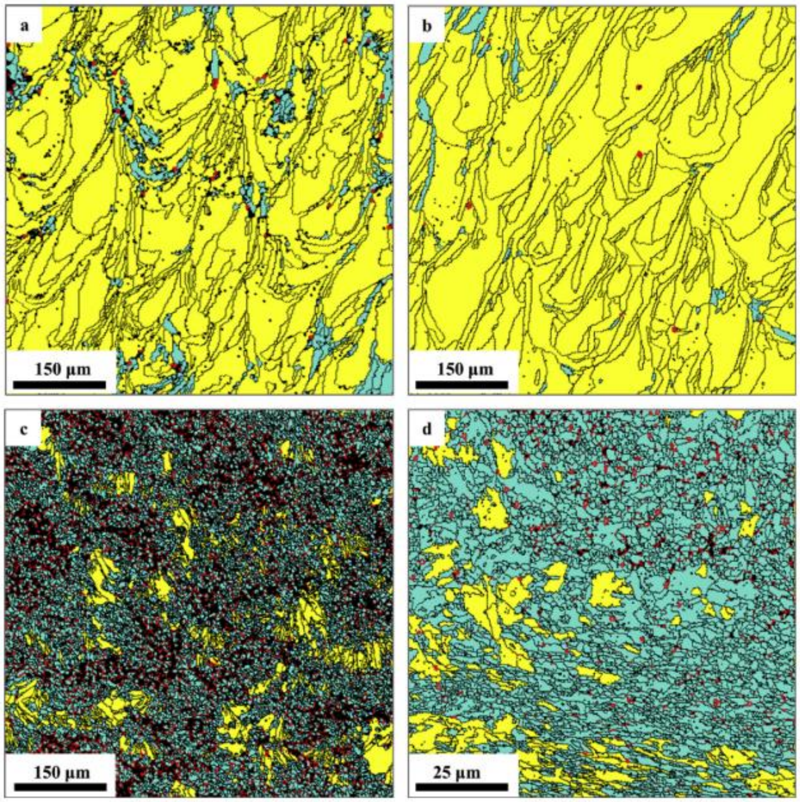

Figure 5. Microstructural variance across 3 different powder suppliers with the same specification for 17-4PH steel feedstock powder. (c) and (d) are the same powder. EBSD maps where green is martensite, yellow is ferrite, red is austenite, and black is unindexed.[53]

Chapters 2 and 3 focus on 17-4PH steel, understanding the microstructural evolution throughout LPBF processing, and utilizing this microstructural control to create parts with hybrid microstructures that are not possible to create with any other manufacturing process. Traditionally, 17-4PH is a martensitic steel. However, the LPBF literature has reported that the as-printed condition of 17-4PH varies greatly between prints[54–56]. When printed, 17-4PH presents very different and more complex microstructures, encompassing various fractions of martensite, austenite, and ferrite, depending on laser speed, power, printing strategy, and shielding gas[53,57–

71]. Most recently, Haines *et al*. observed austenite, ferrite, and martensite all present in 17-4PH[72], whereas An *et al.* observed mostly ferrite with little martensite[73]. Figure 5 further exemplifies this material problem. Three different supplier's feedstocks, printed in the same printer and parameters, result in vastly different microstructures from fully ferritic to fully martensitic. These structures can be practically homogenized and quenched back into their standard condition-A (fully martensitic) microstructure. However, such large differences in observed as-printed microstructures necessitates investigating the LPBF process control of 17-4PH and how 17-4PH microstructurally evolves during printing. It is essential to note that this problem of 17-4PH inconsistent microstructure across builds would impact quality and reliability for any future 17-4PH LPBF applications. This demanded the previous research focus of LPBF literature towards creating homogeneous microstructures most representative of their conventional wrought counterparts[74–76].

Nevertheless, this challenge with 17-4PH steel presents a significant and unique opportunity in that multiple phases and microstructures are desirable for different properties (i.e. ferrite is soft/ductile while martensite is strong/brittle). This is different for many conventional materials, where LPBF processing primarily results in either too little or too much energy input, causing excess porosity. With the exception of some recently introduced multi-material powder bed systems[77–79], most powder bed processes have uniform feedstock and do not allow compositional grading. Thus, the only possible route in LPBF is control of microstructural evolution is by local tailoring of the processing parameters. Recent progress in this field has shown significant ability to locally control the grain size, shape and texture, by manipulating the printing strategy in order to tune the direction of the temperature gradients upon cooling[80–85]. Mukherjee *et al*. have thoroughly reviewed and outlined the different methods for controlling the grain structure, phases, and defects in metal AM parts[86]. Most notably, Sofinowski *et al.* have introduced highly controllable layer-wise engineering of grain orientation (LEGO) microstructures, where the crystallographic grain orientation in LPBF 316L steel[87] and Ti-Nb[88] can be locally manipulated with great accuracy by using the laser scan speed and printing strategy to manipulate thermal gradients. This capability has recently been further refined by Gao *et al.* through careful selection of the hatch spacing and remelting the same location from multiple laser scans. This allows for controlling the grain orientation texture of LPBF 316L at a resolution of 125μm[89]. Similarly, Plotkowski *et al.* have shown the ability to control grain texture and morphology in EBM Inconel 718 by locally tuning the amount of time the material is above the melting point, generating equiaxed and columnar microstructures on a point-by-point basis[90]. These approaches indicate the feasibility of manipulating the processing parameters to affect the resultant microstructures. However, the work to date does not result in significant spatial gradation in mechanical properties nor the ability to generate local microstructures with competing properties (e.g., strong/brittle VS soft/ductile)[80,88,91]. A full understanding of this microstructural evolution will allow us to control the structure in a location-specific manner, which is only possible due to the unique localized point-by-point solidification occurring in LPBF.

Chapter 2 investigates the empirical relationship between processing parameters and microstructure, primarily between volumetric energy density and variations in the ferrite/martensite fractions and their corresponding mechanical properties. In agreement with a large body of literature, vastly different as-printed microstructures and properties are observed under different printing conditions. However, this issue of microstructural variance is transformed into the capability to locally control the structure and properties throughout a part. This leads to hybrid microstructures where ferrite and martensite are selectively placed to control the local deformation and the printed part's overall bulk properties. Additionally, Chapter 2 investigates the resolution of microstructural control, and whether the structure and properties are controllable at a voxel size of 1mm or 1µm. Ultimately, microstructural differences are observed at the scale of the melt pool, which are further investigated in Chapter 3. Key methodologies used in Chapter 2 are mechanical testing (primarily microhardness and tensile testing) to quantify differences in properties and resolution of control. SEM and TEM are utilized to characterize the different microstructures and their nano-precipitates. Finally, hybrid composite microstructures are printed by modulating the printing parameters within a single part; to exemplify an intermediary between the bounds of bulk properties and highlight the capability to locally control the microstructure. 3D Digital Image Correlation is used to measure full strain maps of samples during tensile testing.

Chapter 3 further investigates the thermodynamic and kinetic phenomena causing these differences in phase evolution. Detailed experiments are conducted and analyzed at the scale of the melt pool into how specific printing parameters (primarily hatch spacing and thus melt pool overlap) are responsible for differences in phase stability within the melt pool. Key methodologies such as Optical-Emission-Spectroscopy and X-ray-fluorescence are used to quantify small changes in the global and local chemistry of the samples. Differential Scanning Calorimetry is used to deconvolute the effect of thermodynamics from kinetics. Additionally, FEA models and CALPHAD calculations are utilized to estimate thermal histories from different printing parameters and understand the effect of cooling rate on phase evolution throughout samples printed under different conditions. With a thermodynamic understanding of how the Fe-Cr-Ni system behaves with slight variations in composition, combined with calculated kinetics effects from the extreme LPBF thermal history, a descriptive decision tree is created in which specific printing parameters can be chosen to fully design the microstructure in a location specific manner.

Although LPBF has enabled unparalleled geometric design and noticeable improvements in properties of certain alloys, certain material problems still limit the understanding, applicability, and advancement of LPBF technology. The overarching focus of this thesis is on understanding and solving these scientific problems in two important structural alloy systems, aluminum and steel. The specific problems and chapters of this thesis are: (Chapter 1) Printing of a novel modified 7xxx series aluminum alloy which is insensitive to hot cracking and accounts for compositional changes from evaporation, (Chapter 2) Developing strategies to tailor the microstructure and phase distribution of 17-4PH steel locally, and (Chapter 3) Understanding the thermodynamic and kinetic mechanisms driving LPBF 17-4PH microstructural evolution. With a focus on compositional and structural control of alloys in the two most important structural engineering material systems, aluminum alloys and steels, this dissertation elucidates how solving material specific problems enables structures and properties only possible and enabled through LPBF.

Key Results

Synopsis of Chapter 1 Results

The precise composition of Al-7068 alloy must be known for the various processing conditions. Otherwise, resulting structures and properties will vary from one print to another. Figure 6 demonstrates that the evaporation of Zn and Mg can vary from 25% upwards to 60% depending on the laser settings used during printing. Analytical calculations are conducted based on estimated melt pool temperatures and the vapor pressure of each individual element. The details of analytical calculations can be found in Appendix 1. It is important to note that the analytical calculations closely match the experimental measurements in the energy density range of 150 J/mm^3 to 200 J/mm^3, which is when the printed samples are fully dense (See Chapter 1 section 1.3.2 for porosity analysis showing optimized porosity in that energy density range). This is ultimately expected, considering that when samples suffer from a lack of fusion porosity from too little energy input or keyholing porosity from too much energy input, the heat transfer assumptions of the analytical melt pool model are much less accurate. Confirming that analytical predictions match experimental measurements of evaporation and composition, this will be a useful tool in future development of aluminum alloys.

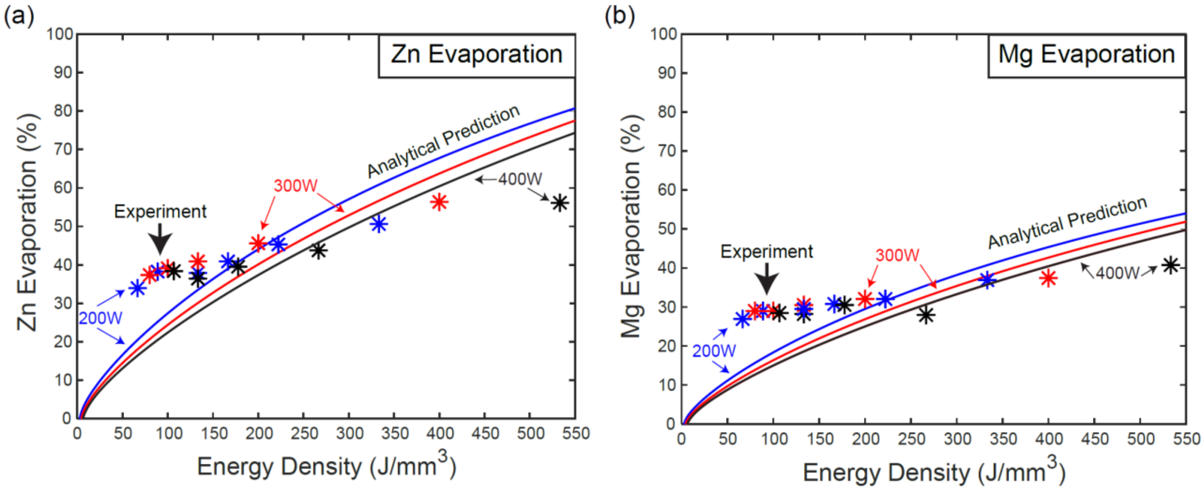

Figure 6. Analytical predictions and experimental measurements of (a) Zinc and (b) Magnesium evaporation.

With the post-print composition of Al-7068 now in an appropriate range, it is necessary to understand the phase evolution during processing and how the TiC nanoparticles affect solidification. Figure 7 shows equiaxed grains in the as-printed condition and thus elimination of hot cracking (see Chapter 1 section 1.3.2 for bulk micrographs, and Chapter 1 supplementary for grain orientation). Figure 7d STEM-EDS shows Ti (representing TiC nanoparticles) within the FCC-Al grain and not solely located at the grain boundaries. This indicates that TiC acts as a heterogenous nucleation site, altering the solidification mode from columnar (as commonly seen in LBPF) to equiaxed. Such change in solidification mode eliminates of hot cracking. Equiaxed grain formation and elimination of hot cracking is substantial, enabling printed samples to have improved ductility, reach ultimate strength, and not suffer from anisotropic mechanical properties.

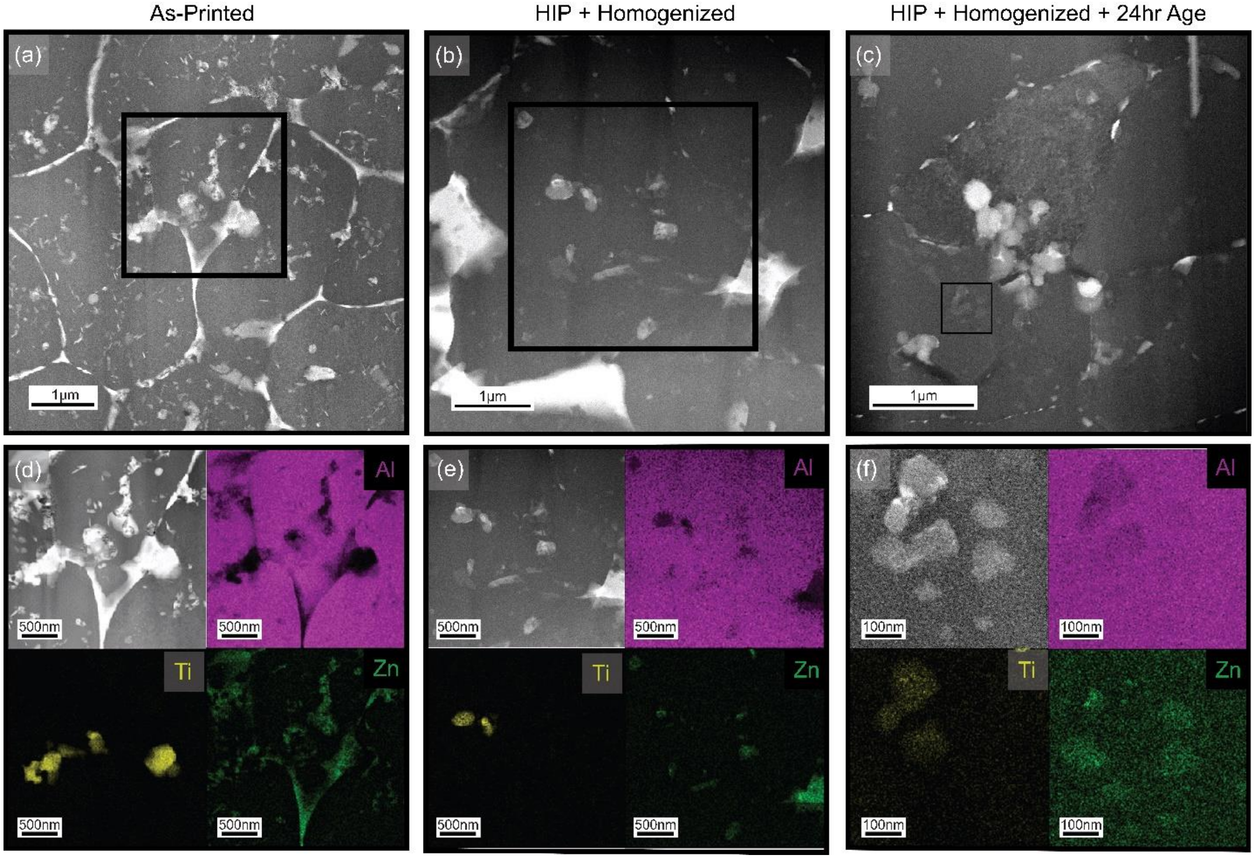

Figure 7. (a)-(c) STEM micrographs showing the phase distributions and (d)-(f) STEM-EDS measurements showing the TiC and $MgZn_2$ phases ,in the as-printed, HIP + homogenized, and HIP + homogenized + 24hr aged samples, respectively.

Many precipitates (colored white in Figure 7a) can be noted in the as-printed condition. This is due to the builds sitting on the 200°C preheated build substrate for multiple hours during printing, well above the 130°C aging temperature. Thus, the as-printed sample is essentially overaged. The necessary following homogenization treatment shown in Figure 7b and 7e is conducted to solutionize the $MgZn_2$ precipitates back into solid solution. However, due to Mg and Zn compositions noticeably above the Al-7068 standard range (see Chapter 1 Section 1.3.1 for full chemistry), the homogenized condition is fully saturated, and there remain some precipitates in the homogenized condition. Figure 7c and 7f show the microstructure in the aged condition. The precipitates' size and spacing are used in Orowan strengthening calculations in both the homogenized and peak 24hr aged conditions.

Figure 8 compares the experimentally determined yield strength with the calculated yield strength based on analytical strengthening mechanisms. See Appendix 2 for the details regarding the physical properties used for the calculations, Chapter 1, section 1.3.3 Figure 1.9 for the X-ray diffraction used in calculating the dislocation strengthening and solid solution strengthening, and Section 1.3.4 Figure 1.12 for the experimental stress-strain curves. Yield strengths are within 2% and 15% for the peak-aged and homogenized conditions respectively. It should be noted that the Orowan strengthening is primarily due to the $MgZn_2$ precipitates, and not the TiC nanoparticle strengthening. However, the TiC nanoparticles lead to extremely small equiaxed grains of ~1μm diameter. This results in a very high grain boundary strengthening of 95 and 92 MPa in the homogenized and aged condition respectively. Therefore, the TiC nanoparticles significantly reduce the grain size, increase the amount of grain boundaries, and indirectly strengthen the material. Additionally, enrichment of Mg and Zn lead to large precipitate and solid-solution strengthening, leading to the modified alloy reaching strengths competitive with conventional Al-7068.

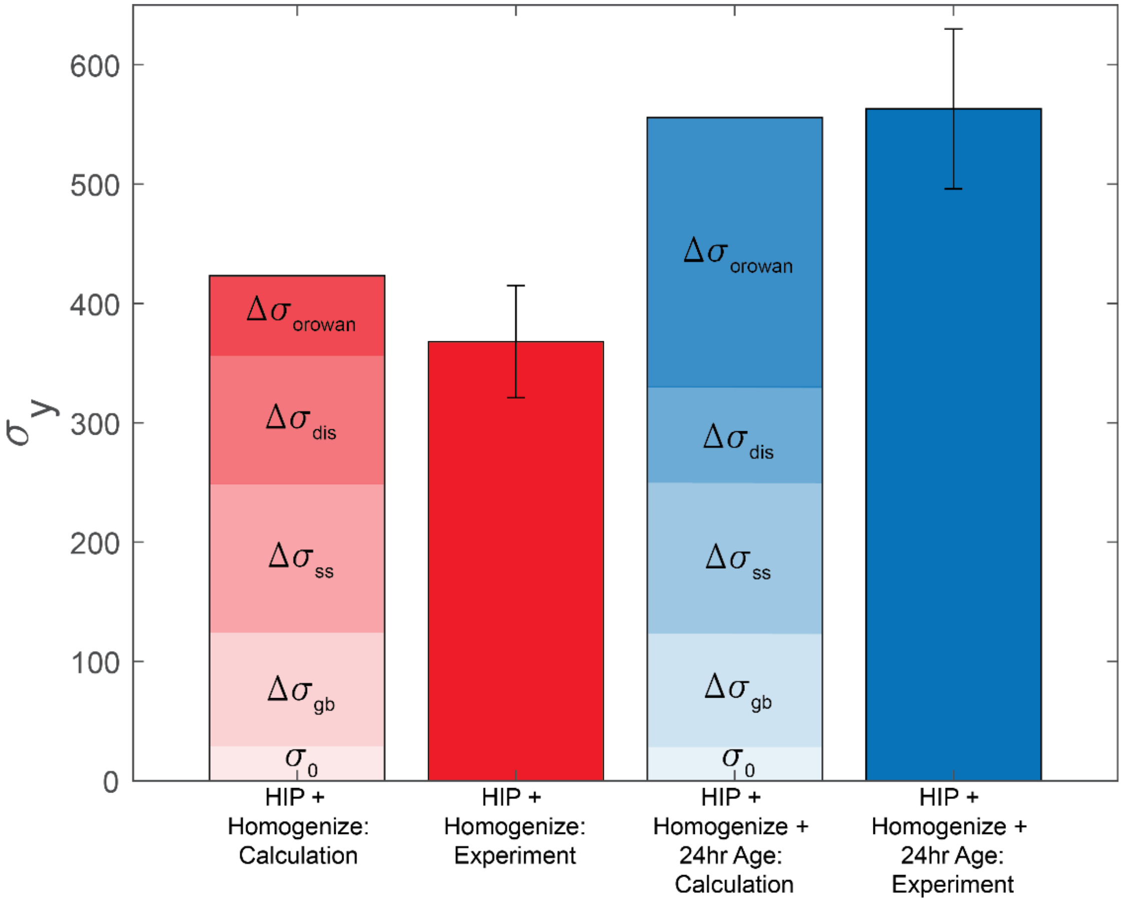

Figure 8. Comparison of the analytically estimated strengthening mechanisms with experimentally determined yield strength values, for the *400W* sample before and after aging.

Synopsis of Chapter 2 Results

For the properties of LPBF 17-4PH to be locally controlled, it is necessary to investigate what range of structures are printable thoroughly. This primarily consists of changing the volumetric energy density (expressing the energy deposited by the laser in a unit volume, and defined as laser power divided by the product of scan velocity, layer thickness and hatch spacing (see Fig. 1)), which will alter the thermal history. Thus, as seen in the literature [74–76], it is expected to observe substantial variation in microstructures between specimens. Figure 9 highlights the differences in phases observed from dual-phase ferrite/martensite (Fig 9a-9c) in the lower energy density (E_D = 100 J/mm^3) sample and fully martensitic in the higher energy density (E_D = 400 J/mm^3) sample. This can consistently be controlled across different part geometries and is utilized to create a gradient hybrid microstructure shown in Figure 9g, in which it can be toggled where ferrite and martensite are precisely located. Figure 9h-9j confirms the large columnar grains are ferrite. See Chapter 2 supplementary Figure S2.3 showing this same microstructure across multiple printed geometries.

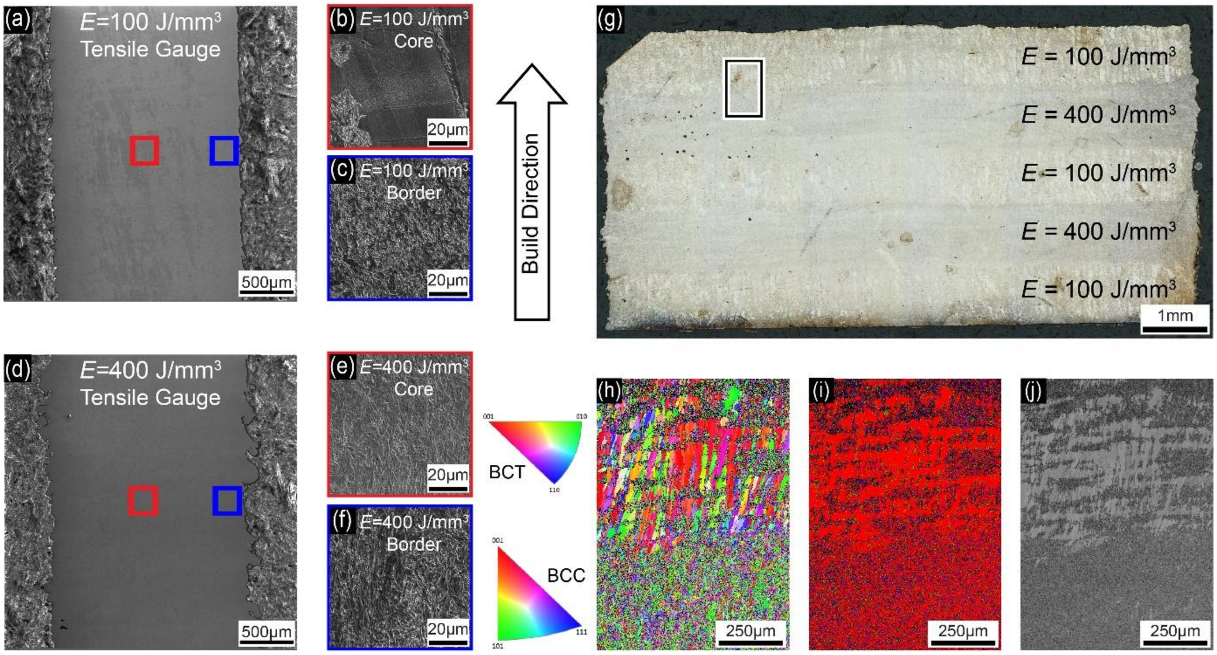

Figure 9. (a,d) SEM images of dual phase versus fully martensitic microstructures from gauge sections of dog bone specimens processed with E=100 J/mm^3 and E=400 J/mm^3, respectively. Microstructures of the inner core versus the outer border of the samples are shown in (b-c) for E=100 J/mm^3 and (e-f) for E=400 J/mm^3. (g) Optical image of an etched hybrid sample printed by alternating 1mm layers at E=100 J/mm^3 and 400 J/mm^3, with IPF-X maps, phase maps, and band contrast maps shown in (h-j) for the inset in (g), respectively. The build direction is upwards throughout the figure. (See Figure S2.1 for geometric details).

To utilize this microstructure control, Figure 10 shows parts printed with the gradient direction upwards (Figure 10a) and with the gradient direction in the plane with the build direction (Figures 10b-10c). Corresponding microhardness maps are shown in Figures 10d-10f. The properties can be controlled in both orientations. Notice that the E_D = 100 J/mm^3 regions have hardness of ~400HV on surfaces parallel to the build direction (Figure 10d), and ~450HV on surfaces parallel to the build platform (Figures 10e-10f). This anisotropy in mechanical properties is attributed to the columnar nature of the ferritic grains, which dramatically elongate along the printing direction (Figure 9i): when hardness is measured parallel to the build plate, more grains are indented, resulting in higher hardness.

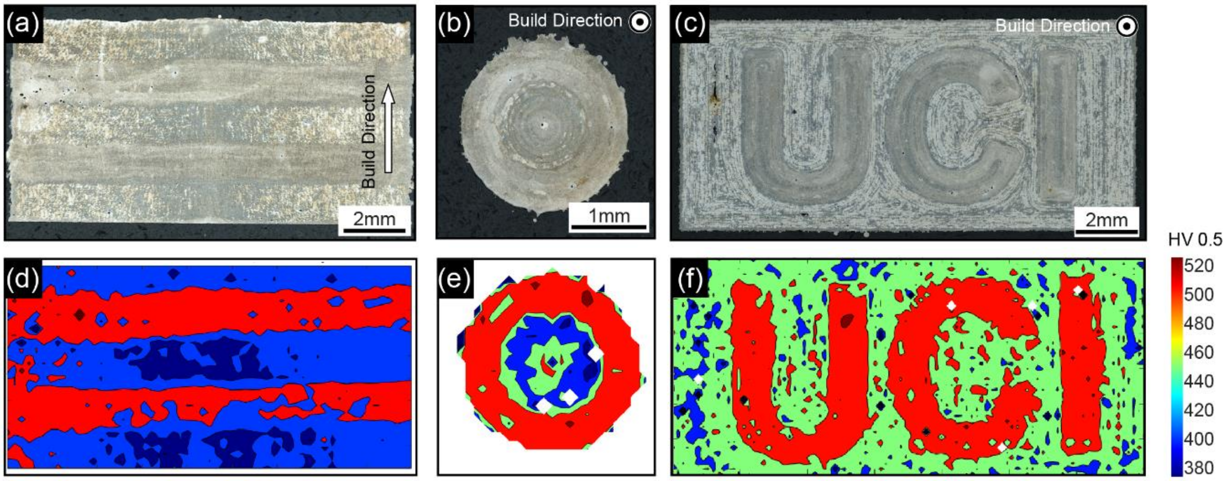

Figure 10. Optical images (a-c) and Vickers HV0.5 hardness maps (d-f) of etched hybrid samples: (a,d) a block printed by alternating 1mm-thick layers processed with E=100 J/mm^3 and 400 J/mm^3; (b,e) a cylinder printed with an E=100 J/mm^3 core and a 400 J/mm^3 outer shell; and (c,f) a block printed at 100 J/mm^3 encompassing the UCI logo printed at E=400 J/mm^3. (See Figure S2.1 for geometric details).

To investigate this property control more convincingly, a hybrid brick-and-mortar microstructure is printed with harder E_D = 400 J/mm^3 bricks placed within a softer E_D = 100 J/mm^3

matrix. The tensile properties of these hybrid specimens are compared with the experimental bounds of E_D = 100 J/mm^3 and E_D = 400 J/mm^3 samples in Figure 11a. Digital image correlation strain maps of the hybrid composite specimen are shown in Figure 11b. Notice how at every point during the tensile test, from initial yield to final fracture, the hybrid composite is locally deforming in the softer E_D = 100 J/mm^3 region. Such control of local deformation enables significant design improvements in mechanical properties for different structures, particularly regarding energy absorption. This level of phase grading, previously only achievable with AM techniques such as DED using multiple hoppers, is now being demonstrated for LPBF of dual-phase alloys.

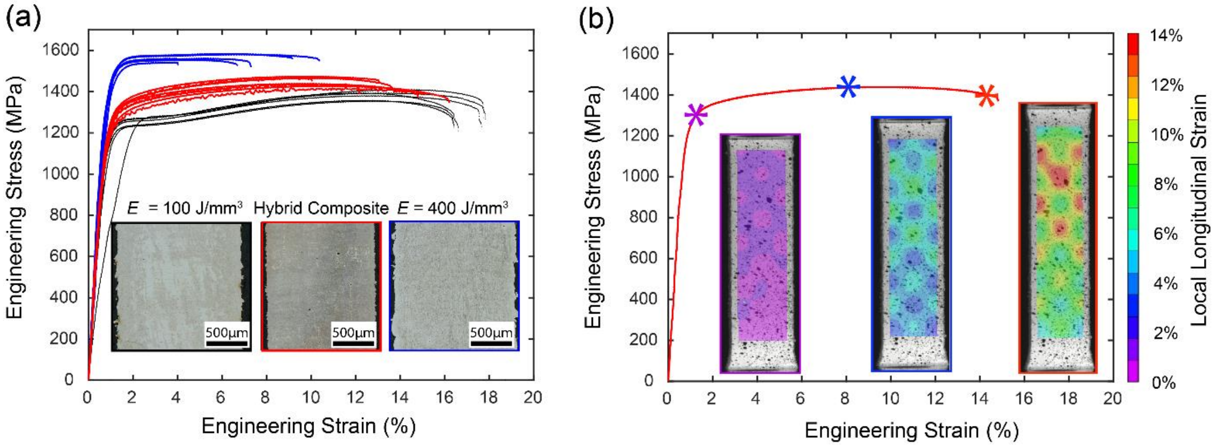

Figure 11. (a) Engineering stress-strain curves from tension tests on dog bone specimens printed with differing processing strategies: (i) uniformly low energy density of 100 J/mm^3 (black); (ii) uniformly high energy density of 400 J/mm^3 (blue), and (iii) a ‘brick-and-mortar’-inspired architecture, embedding prismatic domains (bricks) printed at 400 J/mm^3 in a matrix (mortar) printed at 100 J/mm^3 (red). (b) Stress-strain curve with DIC strain maps for a ‘brick-and-mortar’-inspired sample, clearly showing localized plastic deformation in the softer regions printed at E=100 J/mm^3. (See Figure S2.1 for geometric details).

To fully utilize such microstructural control, it is necessary to understand the cause of microstructural formation as a function of printing conditions. An intriguing observation is revealed in the dual phase ferritic/martensitic E_D = 100 J/mm^3 samples: regardless of part geometry or build orientation, the outer border of the sample (which, in our “Borders Inside-Out” scan strategy, is always the last one to be printed) is always fully martensitic (See Figure 9d-9f and

Chapter 2 supplementary). By contrast, ferrite grains seem to appear almost exclusively in the hatch region between scans. Figure 12 shows single-track walls and dual-track walls printed with E_D = 100 J/mm^3 and E_D = 400 J/mm^3 parameters. All conditions are fully martensitic except for the E_D = 100 J/mm^3 dual wall in Figure 12c. This further reveals that reheating from an adjacent scan is causing previously formed martensite to transform back into ferrite in the hatch region between scans, for the E_D = 100 J/mm^3 sample. However, this is not the case for the E_D = 400 J/mm^3 sample, which remains martensitic under each condition. These observations are currently unexplained and require further investigation, motivating the research conducted in Chapter 3.

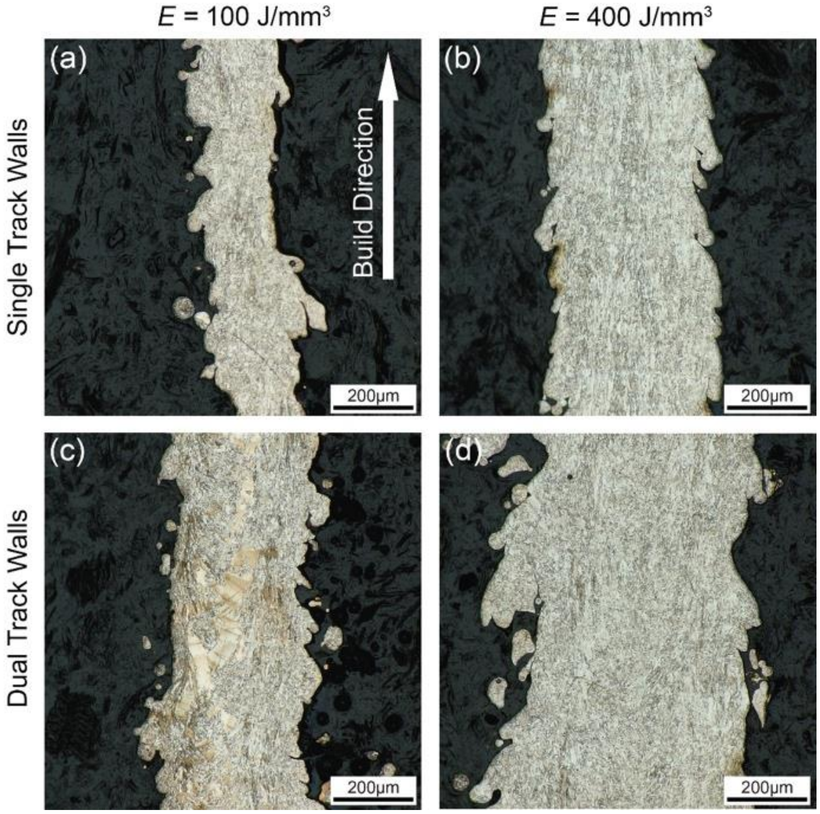

Figure 12. Single-track walls printed with (a) E=100 J/mm^3 and (b) E=400 J/mm^3. Dual-track walls printed with (c) E=100 J/mm^3 and (d) E=400 J/mm^3. Notice that ferritic grains are only present in the inter-hatch spacing in dual-track walls printed with the lower energy density.

Synopsis of Chapter 3 Results

Observations from Chapter 2 on the existence of large ferrite grains exclusively in the *in-hatch* regions of the low volumetric energy density (E_D = 100 J/mm^3) samples motivate a deeper study on the separate effects of hatch spacing and Linear Energy Density, LED (representing the energy deposited by the laser per unit length of melt pool, and defined as laser power divided by scan velocity). Figures 13a-13f illustrate that samples with the higher LED are always fully martensitic, a phenomenon that we can attribute to the higher evaporation of BCC stabilizing elements (see Chapter 3, sections 3.3.2 and Chapter 3, supplementary for full chemical analysis). However, lower LED samples are dual phase only under specific hatch spacings and thus certain volumetric energy densities (VED) (Figure 13g-13h).

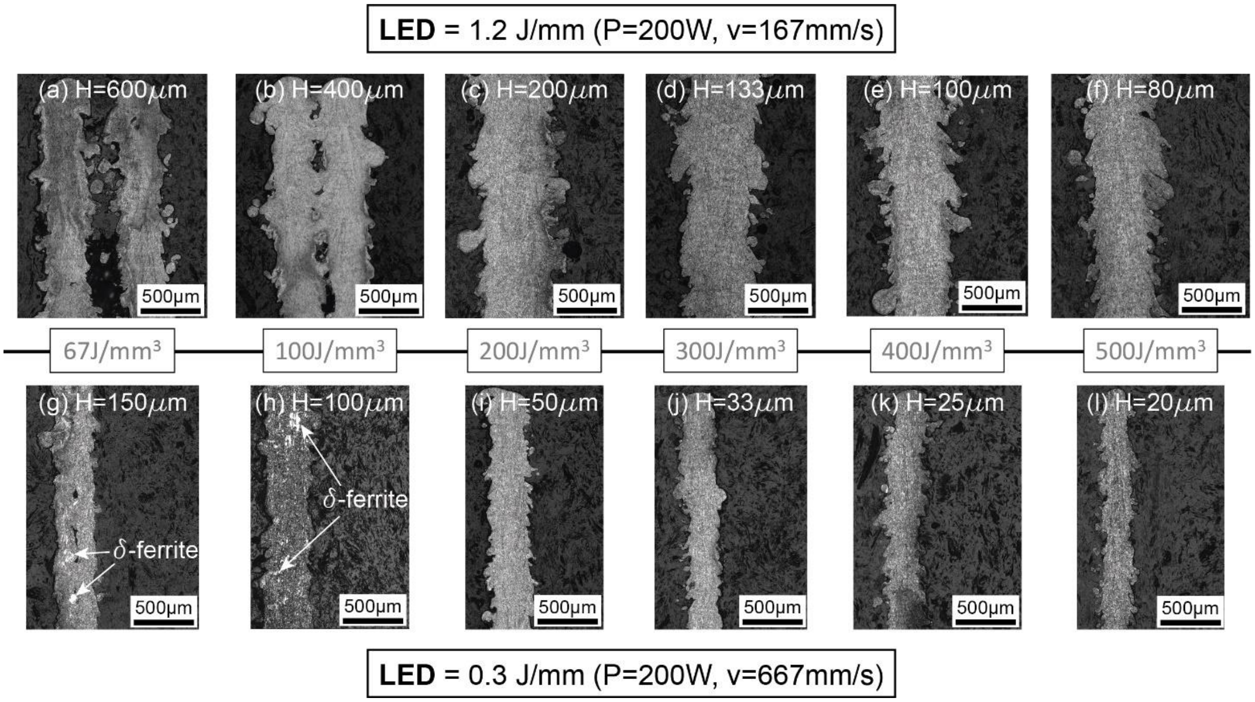

Figure 13. Effect of hatch spacing, and thus VED on dual walls with (a-f) LED = 1.2 J/mm resulting in no columnar ferrite under any printing condition. (g-l) LED = 0.3 J/mm resulting in columnar ferrite forming under hatch spacings of (g) 100µm and (h) 150µm.

As large columnar ferrite grains are only being observed in lower LED samples with hatch spacings lower than 100μm (Figure 13h), further analysis of these samples is warranted. An XRF chemistry map of this dual wall sample is shown in Figure 14. Figure 14c shows Cr segregation within the *in-hatch* region, where ferrite is located. Ni depletion is also observed (Fig 14d). Given that Cr is a δ-ferrite/BCC stabilizing element and that Ni is a γ-austenite/FCC stabilizing element (γ is formed prior to the martensite), these local chemical differences are likely responsible for the observed difference in phase evolutions. Figures 14e-14f show CALPHAD equilibrium calculations of the Cr-enriched and Cr-depleted regions. These equilibrium diagrams confirm that the observed compositional differences across the *In-Hatch* and *In-Track* regions are significant enough to thermodynamically stabilize δ-ferrite in the Cr enriched region (Figure 14f) and eliminate δ-ferrite in the Cr depleted region (Figure 14e).

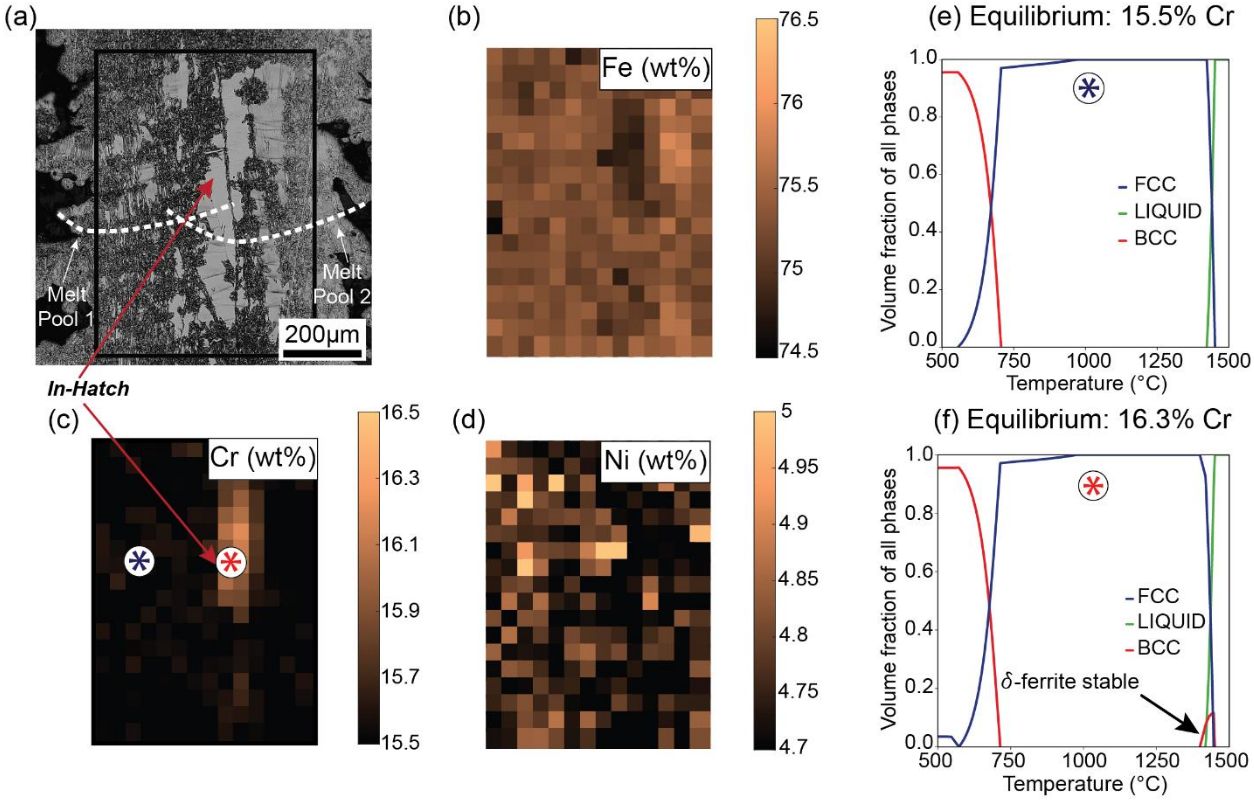

Figure 14. (a) Optical micrograph of LED = 0.3 J/mm & VED = 100 J/mm^3 sample with the boxed region to be XRF'd. XRF measurements of (b) Fe, (c) Cr segregation, and (d) Ni depletion in the ferrite region. Thermodynamic

equilibrium step diagrams calculated for the (e) *In-Hatch* Cr enriched (16.3 wt%) regions and the (f) *In-Track* Cr depleted (15.5 wt%) regions. Notice δ-ferrite is only thermodynamically stable in the Cr enriched region.

Having demonstrated that δ-ferrite can thermodynamically form from the melt in the Cr-enriched region, important kinetics questions still remain, to justify the observed room-temperature microstructures. Scheil solidification calculations consistent with a simulated cooling rate of 5x10^5 ^{o}C/s during solidification (See Chapter 3 Figure 3.6 for the full simulated LPBF thermal history and Appendix 3 for FEA simulation thermophysical details) are shown in Figure 15.

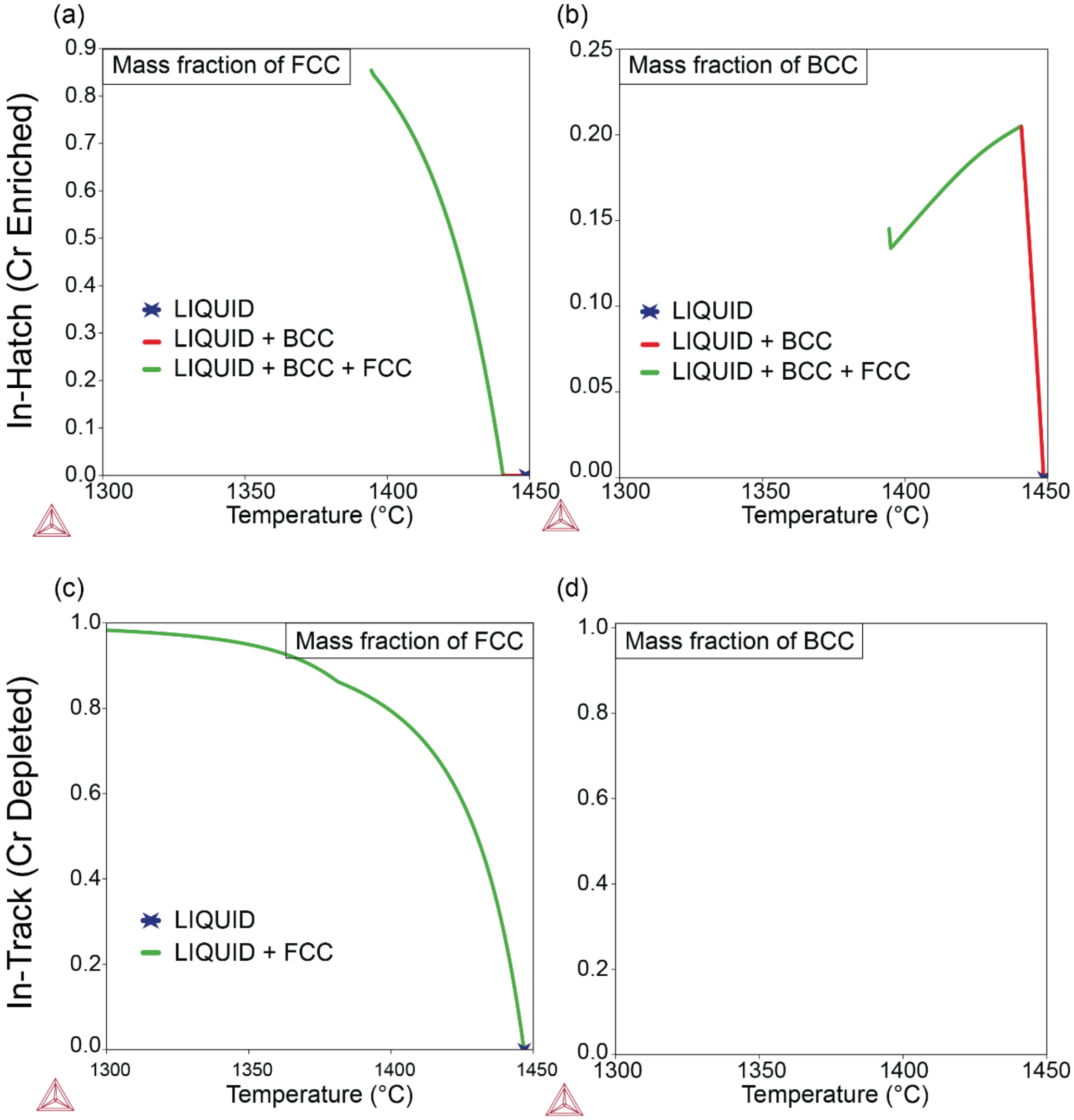

Figure 15. Scheil solidification calculations accounting for both back diffusion into the primary phase, and the δ to γ transformation for the LED = 0.3 J/mm & VED = 100 J/mm^3 sample. The mass fraction during solidification of (a) FCC and (b) BCC for the Cr enriched region. The mass fraction during solidification of (a) FCC and (b) BCC for the Cr depleted region.

Figure 15b shows the mass fraction of δ-ferrite in the Cr-enriched *In-Hatch* region during solidification. Although some of the δ-ferrite is predicted to transform back into γ-austenite, there remains ~15% δ-ferrite upon solidification. In the Cr-depleted *In-Track* region, δ-ferrite is never stable and thus never forms upon solidification. Thus, even with a propensity of δ-ferrite to transform back into γ-austenite (and sequentially transform to martensite upon extremely fast cooling), δ-ferrite remains stable to room temperature.

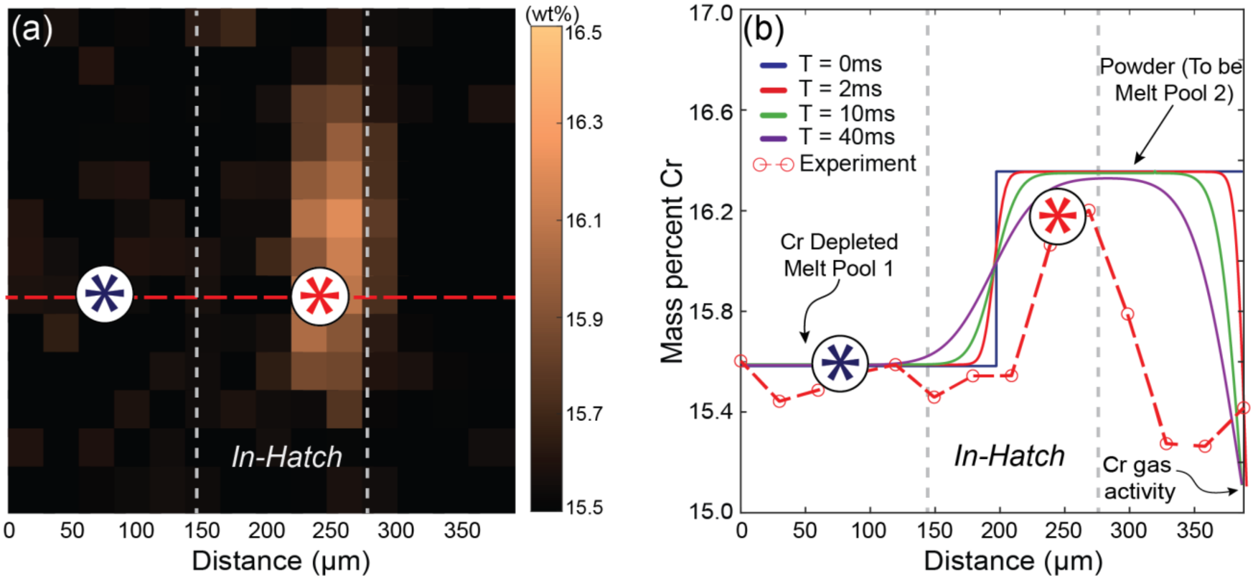

Figure 16. (a) XRF Cr segregation in the *In-Hatch* region. (b) CALPHAD liquid diffusion calculation with a 1% chromium concentration gradient across a 380um region. The diffusion kinetics are fast enough that under a few ms solidification time (as in LPBF), segregation of Cr across the melt pools can be induced.

While the analysis above justifies the room-temperature presence of δ-ferrite in Cr-enriched regions, the origin of Cr segregation in the *In-Hatch* region is still unexplained. Figure 16 shows the 1D Cr line profile of the experimental sample, compared with diffusion calculations from ThermoCalc. The calculations correspond to diffusion in the liquid during solidification, from a Cr-rich virgin powder to a Cr-depleted melt pool. The right boundary condition in this 1D diffusion calculation models the evaporation during printing. Realistically, this model is extremely simplistic, neglecting three-dimensional evaporation patterns, Marangoni convection causing turbulence in the melt pool, and chemical variability across individual powder particles. Nonetheless, this simple 1D model, which accounts for the two major physical mechanisms occurring during melting (diffusion and evaporation), closely matches the experimental 1D Cr profile, and may explain Cr segregation in the *In-Hatch* region of the sample. (See Chapter 3, section 3.3.3, for more details).

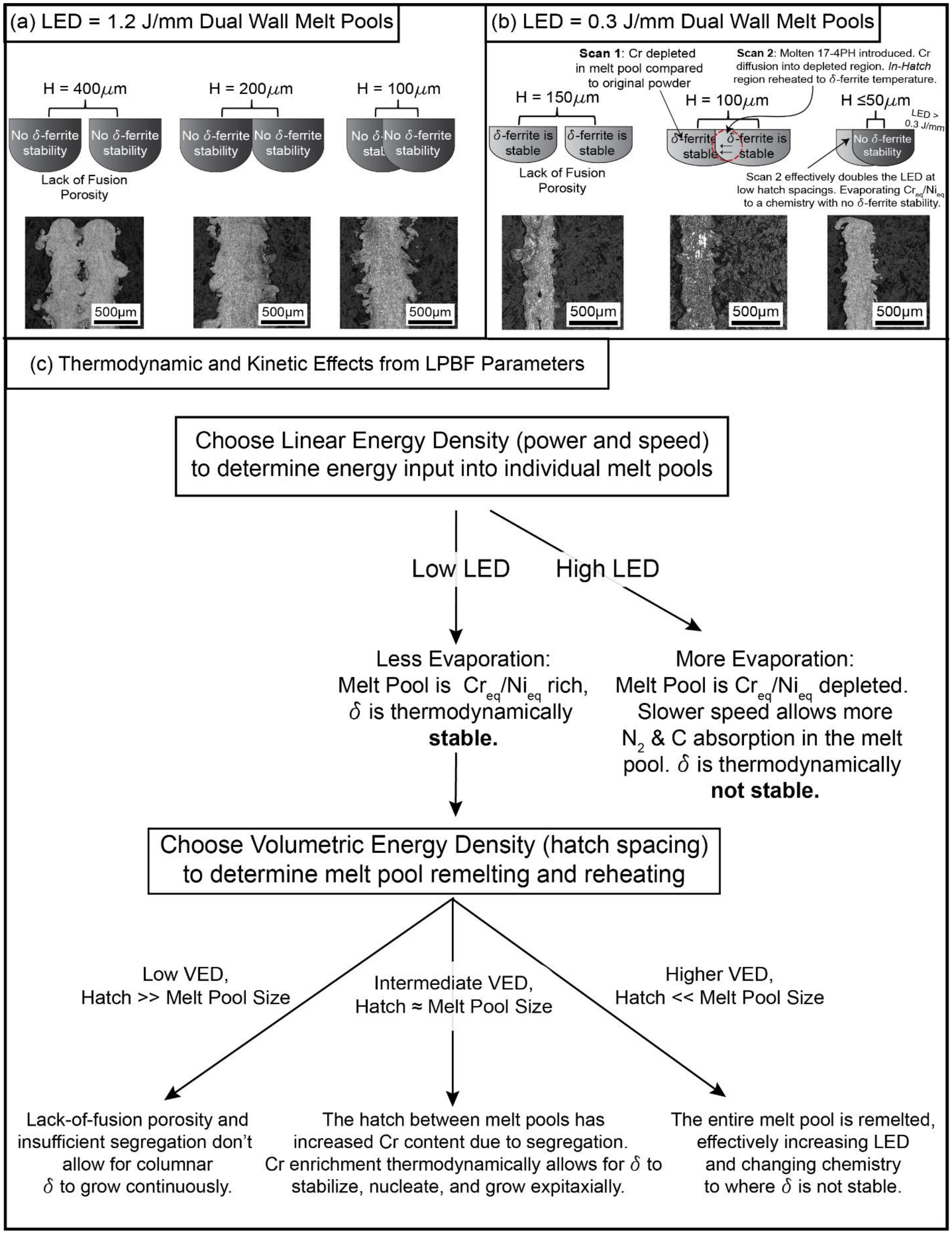

Figure 17. (a) Dual wall melt pools of LED = 1.2 J/mm with various hatch spacings. (b) Dual wall melt pools of LED = 0.3 J/mm with various hatch spacings. (c) Thermodynamic and Kinetic effects from LPBF process parameters.

A comprehensive illustration summarizing the microstructural evolution as a function of processing parameters is shown in Figure 17, corresponding to experimental observations of LPBF 17-4PH microstructures. This manifests into a decision tree, which provides materials designers a useful tool to tune microstructural evolution by independent control of LED and VED. This framework explains how thermodynamics and kinetics individually affect the microstructural evolution of 17-4PH during printing, and can be qualitatively generalized to a wide range of dual phase alloys.

Conclusions of the Dissertation

The research conducted in this PhD thesis establishes a framework for chemical and structural control in aluminum and steel alloys via LPBF. For additive manufacturing to reach its full potential across multiple industries, the complex relationships between processing parameters and microstructural evolution – and ultimately mechanical and physical properties, must be deeply understood and controlled.

In the first part of this thesis (Chapter 1), a rigorous framework for LPBF of aerospace-quality, precipitation-strengthened Al-7xxx alloys is introduced. The proposed approach uses evaporation models to predict the optimal feedstock composition as a function of processing parameters and desired alloy chemistry, and the introduction of TiC nanoparticles to break dendrite formation and limit hot cracking, while also strengthening the alloy by grain size reduction. It is shown that an Al-7068 alloy can be successfully printed and heat treated, reaching mechanical properties on par with those of Al-7068 wrought parts.

In the second part of this thesis (Chapters 2-3), a unique feature of LPBF manufacturing, namely the extremely localized nature of the solidification process, is exploited to demonstrate spatial control of microstructural evolution and hence mechanical properties. 17-4PH steel, one of the most widely utilized high-strength steels in the market, is used for this study, thanks to its extreme sensitivity to chemical variations and cooling rates. In Chapter 2, it is demonstrated that when printed at high energy density (400 J/mm^3), the material develops a fully martensitic microstructure; by contrast, when printed at lower energy density (100 J/mm^3), a dual phase microstructure ensues, with martensitic laths interspersed with large ferritic grains, which largely populate the inter-hatch regions of the samples. The two microstructures exhibit significantly different mechanical properties, with ~20% differences in strength and ~150% differences in ductility. Local microstructural control with a resolution of ~100 microns is demonstrated in samples of different shapes and sizes. In Chapter 3, a combination of multiple experimental techniques and modeling approaches is used to unveil the thermodynamical and kinetic phenomena responsible for the complex phase evolution presented in Chapter 2. The results provide a mechanistic understanding of microstructural evolution of 17-4PH steel processed in LPBF, and explain the origin of complex spatially heterogeneous two-phase microstructures that were observed in Chapter 2 (as well as multiple previous studies from the literature). While these results can be used for intentional local design of specific microstructures in 17-4 PH steel, the physical mechanisms discussed in Chapter 3 provide a general mechanistic framework for microstructural evolution, which can be applied to other dual phase systems such as Nitinol, Fe-Mn-Si shape memory alloys, Ti-6Al-4V, and Fe-Cr reduced activation ferritic/martensitic steels.

Recommendations for Future Work

Regarding future scientific investigations, the development of in-situ experimental techniques to better understand the formation of 17-4PH and similar dual-phase alloys during printing is recommended. In-situ experiments are often cost-prohibitive, leading to volumes and sample sizes not representative of the manufacturing process in practicality. Development of these methods would allow for a stronger literature base to be built up. Additionally, from a stronger literature of in-situ experimentation, developing simulation techniques created specifically for LPBF is critical. There are currently some options available on the market. However, they are often (i) cost-prohibitive, (ii) unable to be calibrated/compared with experiments (thus necessitating the development of in-situ techniques), and (iii) unable to simulate realistic part sizes. The issue of small parts sizes and long simulation times will be inevitably solved with the development of general purpose GPUs. However, it should be particularly focused on by materials scientists to develop LPBF physics specific software and in-situ experimental techniques for the further development and study of these alloys.

Additionally, the use of analytical evaporation models in future modified design of aluminum alloys is recommended. From the work conducted in Chapter 1, the Zn should be dropped by ~5% in the powder to 12.5% for Al-7068 alloys. This will improve ductility by allowing a full homogenization window. Analytical models should also be further matured regarding their applicability in more complex alloys. Particularly, in alloys with multiple components that don’t have such large variations in vapor pressure, such as complex steels or high entropy alloys.

Regarding future engineering applications, the microstructural control demonstrated in this thesis needs to be confirmed and utilized in the printing of other dual-phase alloys, particularly Ti-

6Al-4V and Nitinol shape memory alloys. These are two important alloys that already have many engineering applications and still have potential for further development and optimization. Additionally, the investigation of emergent properties through hybrid microstructures should be thoroughly conducted. This would need to be a property not dominated by the rule of mixtures, such as energy absorption or fracture toughness. This thesis demonstrates how to control the strength and ductility of LPBF 17-4PH as an intermediary between two bounds; i.e. a stronger fully martensitic structure and a more ductile dual-phase ferrite/martensite structure. A significant improvement would be to have an emergent property better than properties from either single microstructure alone. This would open up many innovations in microstructural design, to be used across engineering applications.

1. Chapter 1. A Modified Aluminum 7068 Nanostructured Alloy

1.1. Introduction and background

Martin *et al.* first demonstrated that incorporating Zr nanoparticles (NPs) as inoculants in the Al alloy powder feedstock eliminated hot cracking in LPBF-processed parts. The Zr nanoparticles promoted heterogeneous nucleation from in-situ formed Al_3Zr inoculants within the melt pool, resulting in refined equiaxed grains[14]. Molecular dynamics simulations have verified the amount of low-mismatch lattice planes between the inoculant and the matrix phase to be a good predictor on how well heterogenous nucleation prevails[92,93]. Additionally, Sistiega *et al.* have shown that increasing the silicon content up to 4% in Al-7075 reduces the tendency to hot crack, due to an increase in latent heat and decreased solidification range, enabling to successfully print nearly fully dense parts. However, Si stabilizes the β-$MgSi_2$ phase, which has a decreased strengthening effect compared to the desired η-$MgZn_2$ phase in 7xxx alloys, resulting in lower mechanical properties[94]. Spierings *et al.* printed a novel aluminum-scandium alloy (Scallmalloy™) via LPBF; formation of $L1_2$ Al_3Sc precipitates led to heterogenous nucleation, resulting in an equiaxed grain structure, and mechanical properties competitive with those of wrought Al-7075[95]. Scandium inoculants have been consistently shown to eliminate hot cracking and provide improved high temperature strength from the ordered FCC $L1_2$ Al_3Sc precipitates; however, scandium is not economically viable compared to other traditional inoculants such as Zr and Ti[96–104]. TiC and TiB_2 inoculants have been previously shown to improve the processability of high-strength aluminum castings, weld filler, and LPBF powder[105–107], and additionally provide grain refinement, in a cost-effective manner[108–111]. Recent work has shown that TiC's low lattice mismatch with the α-Al matrix makes it effective in increasing nucleation rate and restricting grain growth during processing of 2xxx, 6xxx, and 7xxx series Al[112]. However, varying results in terms of the TiC phase stability and strengthening effect have been reported[45,106,107,113,114], warranting further studies.

Evaporation of volatile elements, such as Mg in 6xxx and Mg and Zn in 7xxx Al alloys, has been observed during LPBF processing[14,31]. R. Mertens *et al.* enriched an Al-7050 + 1% Zr alloy with an additional 7% Zn to counteract evaporation and observed over 50% loss in Zn[115]. Additionally, A. Martin *et al.* varied the Zn composition in the feedstock powders, and observed less than 15% loss in Zn[116]. The literature continues to show varying results in terms of elemental vaporization in multiple aluminum alloys[23,100,117–121], warranting further investigation on the role of processing parameters on post-print composition, and specifically the influence of the energy input into the melt pool on compositional changes. These insights will enable alloy design and control of the constituent elements with different volatilities during LPBF processing.

Al-7068 possesses excellent strength but is prone to hot cracking as well as compositional changes during LPBF processing[122–125]. This study presents a modified Al-7068 aluminum powder with two key features: (i) the addition of TiC nanoparticles to prevent hot cracking by promoting heterogenous nucleation within the melt pool and restricting grain growth during solidification; and (ii) a significant enrichment of highly volatile elements (Zn and Mg) to counteract evaporation during LPBF processing, to achieve the desired target composition in the LPBF printed parts. The influence and effect of LPBF processing parameters (laser power, scan speed, and energy density) on the resultant composition, microstructure and mechanical properties of the printed alloy are carefully investigated and discussed.

1.2. Methods

1.2.1. Materials Preparation

The powder feedstock used in this study was produced by MetaLi™ via Argon gas atomization of the alloy ingot with dispersed TiC nanoparticles[114]. The metal charge of ~18.5 kg was held at 820°C (180°C superheat) in a vacuum furnace for one hour before atomization. The powder was sieved through 15-53µm sieves prior to printing. The powder has an oxygen content of 349.2 ppm and a Carney Flow Rate of 13.4s/50g. The feedstock powder particle size distribution and chemical composition of the alloy are shown in Figure 1.1 and Table 1.1, respectively.

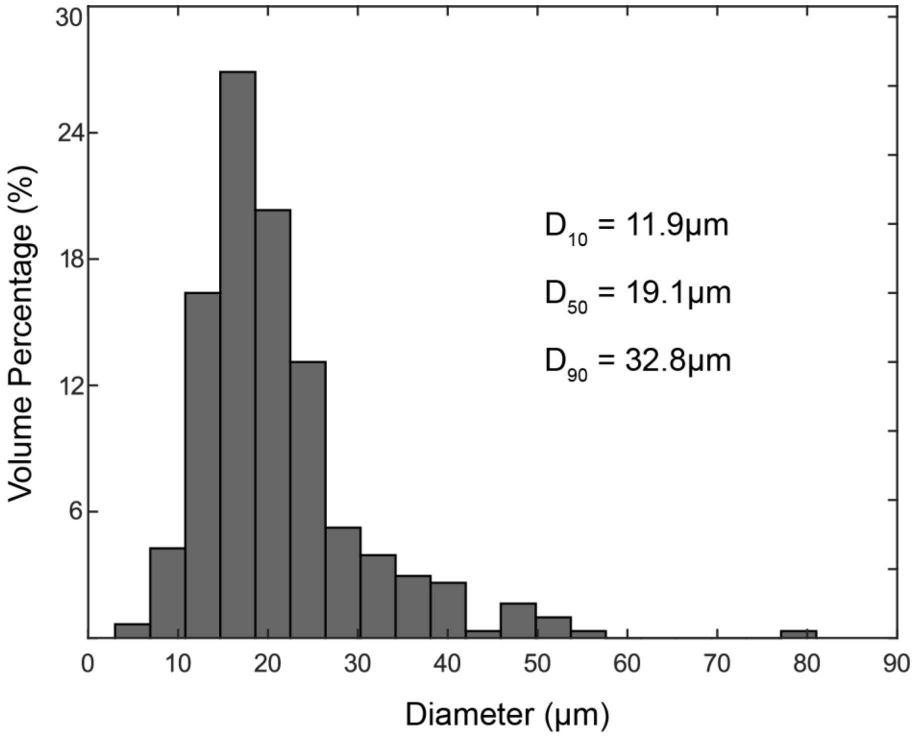

Figure 1.1. Particle Size Distribution (PSD) of the Al-7068+TiC feedstock powder.

Table 1.1. Chemical composition (wt%) obtained from ICP-MS, with TiC percentage provided by MetaLi™.

	Al	Zn	Mg	Cu	TiC
Al-7068 (this study)	Bal.	17.4	3.9	2.0	1.5
Wrought Al-7068 (allowable range[126])	Bal.	7.3 – 8.3	2.2 – 3.0	1.6 – 2.4	-

An SLM 125HL printer with a Yb-fiber 400W maximum output laser was used to print the specimens for this study. Small 5x5x10mm blocks were printed for density and compositional measurements, with laser power and laser scanning speed varying as described in Figure 1.2 and Table 1.2. Samples are printed with laser powers of 200W, 300W, and 400W. Laser scan speed was varied from 250 mm/s to 1250 mm/s. Hatch spacing and layer thickness are kept constant at 100μm and 30μm, respectively. A stripe scan pattern was used, with laser raster parallel to the recoating direction. All additional printing parameters and scan strategy were kept constant through all builds.

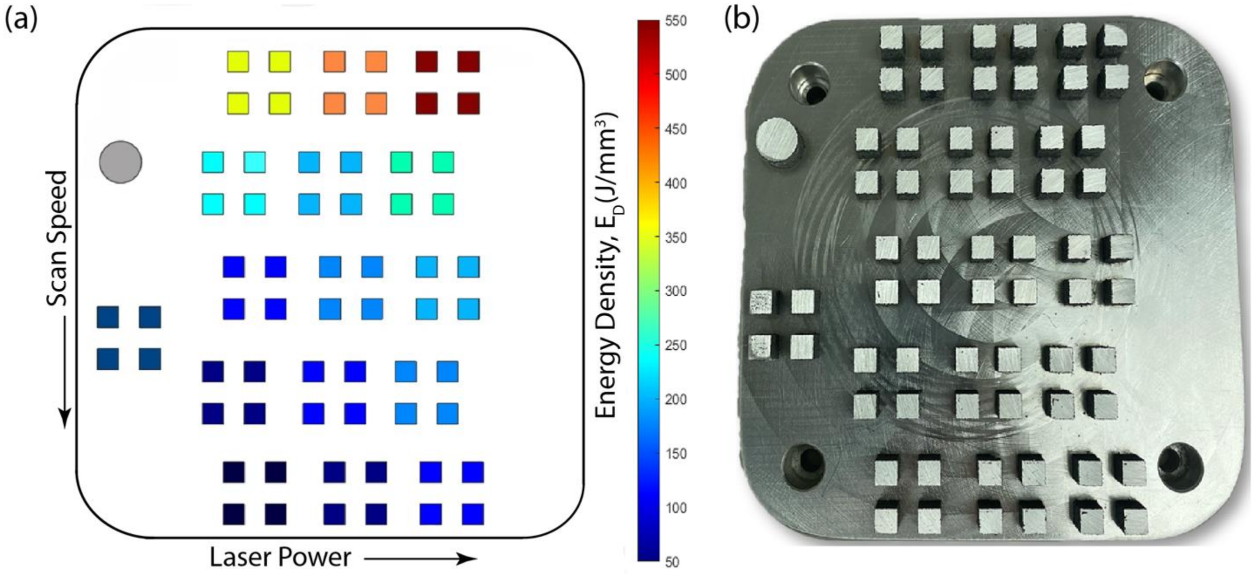

Figure 1.2. Parametric sweep of laser power and laser scan speed, covering a wide range of energy density (E_D), 66 J/mm^3 to 533 J/mm^3. Each set of four 5x5x10mm blocks has nominally identical processing conditions. (a) CAD design file. (b) Printed samples on the build plate, with top surfaces ground.

Table 1.2. Processing parameters for all 5x5x10mm blocks.

Laser Power (W)	**Scan Speed (mm/s)**	**Energy Density (J/mm^3)**
200	200	333
200	300	222
200	400	167
200	500	133
200	750	89
200	1000	67
300	250	400
300	500	200

300	750	133
300	1000	100
300	1250	80
400	250	533
400	500	267
400	750	178
400	1000	133
400	1250	107

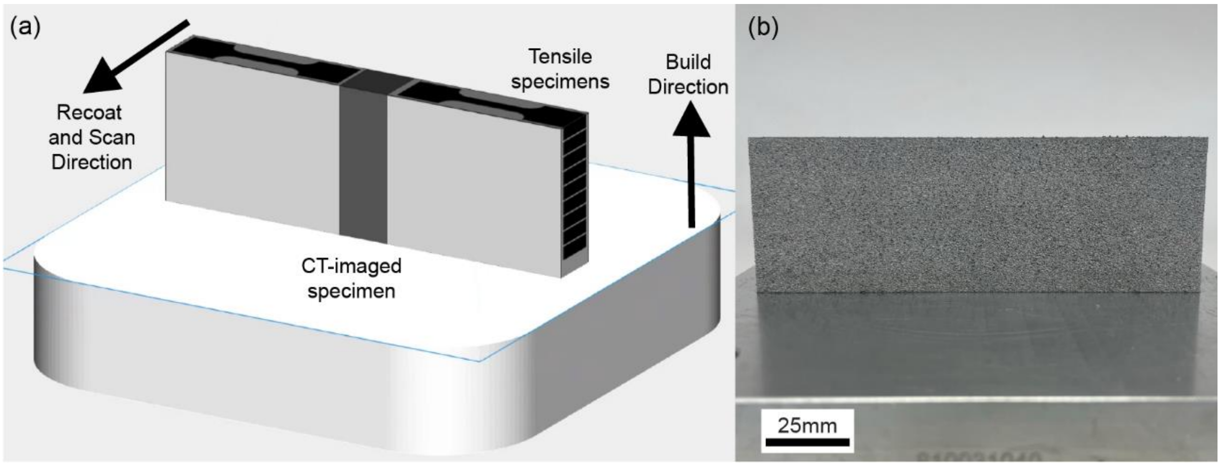

Figure 1.3. Large build geometry used to assess mechanical behavior and porosity distribution: (a) Schematic of the build, highlighting the orientation of tensile coupons and the portion used for CT porosity analysis, and (b) image of the as-printed block to demonstrate build surface finish.

These parameters resulted in volumetric energy density (E_D, defined as the laser power divided by the product of scan speed, layer thickness and hatching distance) varying by an order of magnitude, from 66 J/mm^3 to 533 J/mm^3. Recent studies on LPBF Al report that both Al-Si alloys and high-strength Al alloys (6xxx and 7xxx series) print with >99% relative density with E_D in the 100-200 J/mm^3 range. The addition of ceramic particle inoculants at small volume fractions have shown to not substantially vary this optimal E_D range[42,106,127,128]. However, in this study we decided to investigate a much broader E_D range, in order to to more comprehensively capture the effect of processing parameters on material evaporation. The build chamber was purged with nitrogen down to oxygen levels of 0.01%; the build plate was heated to 200°C during the print. The powder was re-sieved before each print. All samples were printed directly on the build substrate, with electrical-discharge-machining (EDM) used to remove the parts from the substrate.

For tensile tests, larger rectangular blocks with cross-sectional dimensions of 100mm X 12mm were printed, as shown in Figure 1.3. Two different processing settings were used: [200W, 400mm/s] and [400W, 750mm/s], henceforth referred to as *200W* and *400W*. These settings were determined to be optimal from a parametric sweep of the small builds, as discussed in Sec. 3.2. The rectangular blocks were printed with heights ~30mm. The printed tensile blocks were then machined into rectangular tensile coupons via EDM according to ASTM E8[129]. The tensile coupons were cut parallel to the build substrate, with their gauge length perpendicular to the build direction (Figure 1.3a). Material was sectioned via EDM adjacent to the gauge section of the larger blocks and used for metallographic and x-ray diffraction (XRD) analyses. The middle section of the larger block was removed via EDM across the entire build direction and examined for structural integrity via CT imaging.

Post-processing of the samples consisted of homogenization and aging heat treatments. Additionally, select samples were treated with hot isostatic pressing (HIP) before further heat treatments. Samples were homogenized at 465°C for 30 minutes in an MTI GSL-1100X tube furnace in ambient atmosphere with a heating rate of 10°C/s, and then water quenched. Aging treatments were carried out under the same conditions at 130°C, with peak aging being 24 hours. HIP treatments were carried out in a Quintas MIH-9 Hot Isostatic Press at 400°C for 4 hours, with a 2-hour simultaneous pressure and temperature ramp-up from ambient conditions.

1.2.2. Chemical Analysis

Inductively-coupled-plasma mass spectrometry (ICP-MS) was conducted with a ThermoFisher Scientific iCAP RQ system using a single quadrupole detector. The feedstock powder and hand-ground sections from the small blocks were digested using 15ml of trace metal grade 70% nitric acid (HNO_3), and further diluted 150x into 1% HNO_3 solution. Calibration standards for concentration analysis was carried out using the multi-element standard IV-ICPMS-71A from Inorganic Ventures (VA, USA), with a 10 mg/ml analyte concentration in a 3% volume HNO_3 solution.

1.2.3. Microstructural Characterization

The Archimedes method was used for density measurements. Each surface of the small blocks was mechanically ground to 1200 grit, and then polished to 0.05μm using colloidal silica. The weight of the small blocks (w) was measured in air, and the apparent weight submerged in pure ethanol (w_a) measured using a Mettler Toledo AG204 Archimedes scale. The temperature of the ethanol after submerging was allowed to equilibrate, allowing an accurate estimate of the density in ethanol (ρ_f). The density of the alloy (ρ) was calculated as $\rho = \rho_f w/(w - w_a)$. The relative density of the samples was obtained as the measured density divided by theoretical density of the material; the theoretical density was determined using CALculated PHAse Diagram (CALPHAD) equilibrium calculations with ThermoCalc Software's TCAL8 database from known post-print compositions measured by ICP-MS. We emphasize that theoretical densities depend on scan parameters, as rates of evaporation and hence part composition vary.

Four samples were imaged using a VJ Technologies VedaPro X-ray Computed Tomography (CT) platform with a 200μm pixel pitch digital detector array and a microfocus X-ray source with maximum voltage up to 225kV: two small builds with optimal densities (200W-400mm/s, and 400W-750mm/s), and two middle sections EDM'd from the larger builds printed with the exact same parameters. 20μm and 45μm voxel sizes were used for the small and large builds, respectively. Analysis of the pore distribution was conducted in the VGSTUDIO MAX software package.

For powder cross-sectional analysis, the feedstock powder was mounted in an epoxy mix with conductive graphite. The powder was sequentially polished down according to standard metallurgical polishing procedure, with a final polish using 0.05μm colloidal silica. Microstructural analysis was performed using a TESCAN GAIA-3 scanning electron microscope (SEM). Micrographs for particle size distribution analysis were captured using a secondary electron (SE) detector, whereas cross-section micrographs of phase distribution were captured using a back-scattered-electron (BSE) detector. For microstructural analysis of the as-printed builds, the small blocks were mounted in an epoxy mixture and polished down to a 0.05μm colloidal silica finish. Phase-distribution micrographs were obtained in BSE mode, and Energy-Dispersive-Spectroscopy (EDS) elemental maps were acquired with an Oxford Aztec Energy Advances EDS Microanalysis system with a X-MAX 150mm^2 silicon drift detector. Phase fractions were calculated using ImageJ Software (NIH)[130].

Higher resolution microscopy and characterization of the lattice structures and precipitates were conducted with a JEOL JEM-2800 scanning/transmission electron microscope (S/TEM) equipped with a Gatan Oneview camera, operating at a beam voltage of 200 kV. The JEM-2800 is equipped with dual 100 mm^2 silicon drift detectors (SDD) for energy-dispersive X-ray spectrometry (EDS) for elemental characterization. The TEM lamellae samples were extracted using a focused ion beam (FIB) in a Quanta 3D FEG dual beam SEM/FIB (Thermo Fisher Scientific Inc.).

XRD patterns were collected using a Rigaku Ultima X-ray diffractometer equipped with a Cu K_α ($\lambda = 0.154$nm) radiation source configured in Bragg-Brentano geometry. 40kV and 30mA emission was used, and scans were conducted varying 2θ in the range 15-90° with 0.01° step size and scan speed of 0.5 °/s. Each pattern was normalized for comparison.

1.24. Mechanical Testing

Tensile tests were conducted on an Instron 5985 load frame equipped with a 250kN load cell. An AVE2663-901 video extensometer with a Fujinon HF16HA-1S lens was used to track the strain of the gauge section. Tests were conducted according to ASTM E8 standards at quasistatic strain rate of $0.001 s^{-1}$. The printed tensile blocks were machined via EDM into rectangular tensile coupons with gauge dimensions of 20mm in length, 6mm in width, and 3mm in thickness. Vickers hardness measurements were taken with a 50g load held for 10s averaged across 10 measurements, using a Buehler Wilson VH3300 instrument. Hardness was used as a metric to identify the peak aging condition.

1.3. Results & Discussion

1.3.1. Composition Analysis and Selective Elemental Evaporation

As the boiling points of Zn and Mg (907°C and 1091°C, respectively) are much lower than the boiling points of Al and Cu (2470°C and 2562°C, respectively) and not much higher than the solidus of Al-7068 (~465°C), selective evaporation of Zn and Mg during LPBF processing is expected. As $MgZn_2$ is the strengthening precipitate in 7xxx alloys, it is critical to determine the loss of Zn and Mg during processing accurately. At low Zn:Mg ratios, other intermetallic phases, e.g. S-phase and T-phase, become stable and the strengthening contribution from precipitation hardening is reduced[131,132]. Chemical analysis of the small builds was conducted across the parameter sweep to systematically evaluate the role of the volumetric energy density, E_D. Figure 1.4 shows the compositional changes in Zn and Mg as a function of E_D and laser power. The composition for every sample is shown in Table S1.1 in the supplementary information. As energy density increases, the concentrations of both Zn and Mg decrease, as shown in Figures 1.4a and 1.4b, respectively. The Zn:Mg ratio also decreases as much as 33% from the initial starting ratio in the feedstock powder (Figure 1.4c), since Zn evaporates faster than Mg. Importantly, notice that these trends are not directly affected by the laser power alone, confirming that volumetric energy density is a viable metric for predicting evaporation of constituent elements.

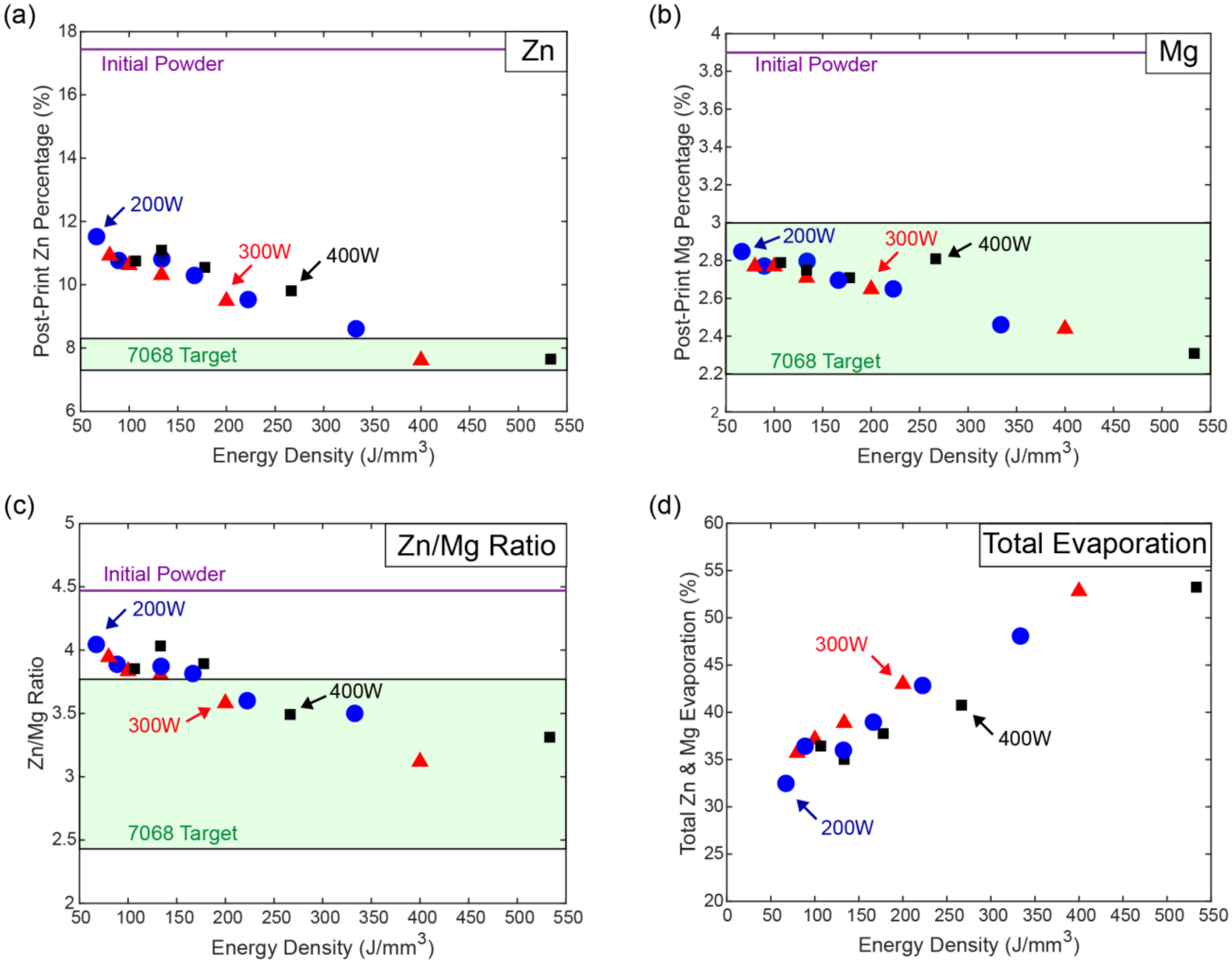

Figure 1.4. Compositional analysis of the resulting builds as a function of energy density: (a) Zn loss, (b) Mg loss, (c) Zn:Mg ratio, and (d) total weighted loss of Zn and Mg.

It has been frequently observed that LPBF-printed 7xxx Al alloys experience significant compositional change relative to the powder feedstock chemistry, with the literature reporting wide ranges of selective evaporation, depending on the process parameters and measurement method used[115,116]. The effect of printing parameters on the temperature of the melt pool, and ultimately on the selective evaporation of low-boiling point elements, can be estimated analytically through calculations of vapor pressures and vaporization fluxes via the Langmuir equation[118]. The melt pool geometry can be estimated using the Rosenthal equation[133,134], under the simplifying assumptions that the melt pool shape is semi-elliptical, the heat flow is two-dimensional, the heat transfer through the melt pool is purely conductive (with vaporization from the top surface), the laser beam is a point source, and all properties of each phase are temperature independent. Details of the calculations are provided in Appendix 1. The experimental measurements of Zn and Mg evaporation are compared with the analytical predictions in Figure 1.5. The predicted trend of a large initial increase in evaporation with a tailoring off towards higher energy densities matches the experimental measurements from this work. It should be noted that our experiments and analytical predictions best agree in the energy density range of 150-200 J/mm^3, which is the region in which we observe maximum density and avoid both lack-of-fusion and keyholing porosity (see Sec. 3.2 and Figure 1.6).

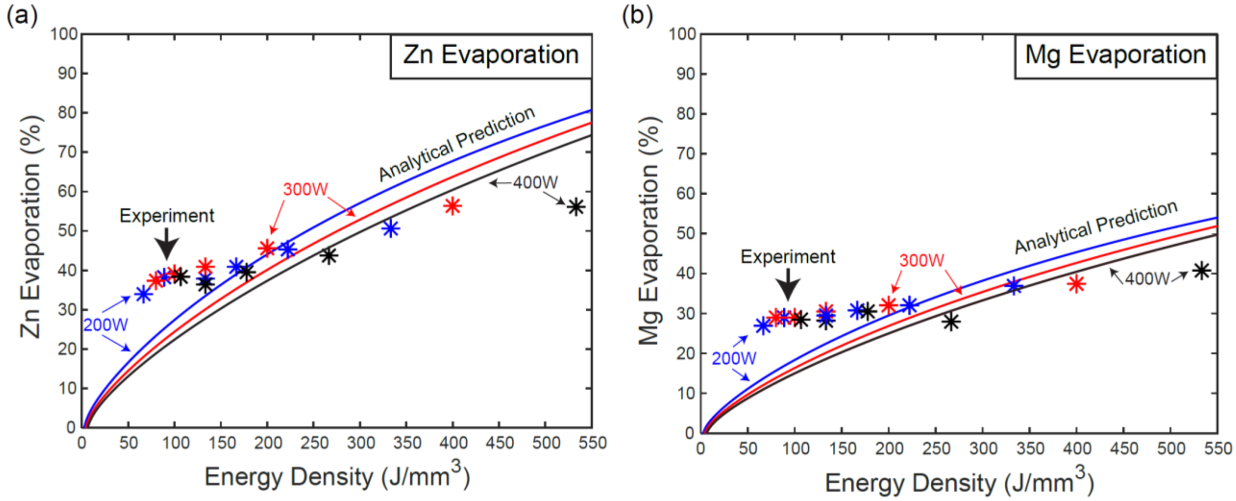

Figure 1.5. Analytical predictions and experimental measurements of (a) Zinc and (b) Magnesium evaporation.

In summary, significant compositional changes occur during LPBF processing of Al-7068, with 30-55% of volatile elements being removed, depending on the energy density (Figure 1.4d). While Mg concentration and Zn:Mg ratios fall within the prescribed ranges for Al-7068 at nearly any energy density, energy densities higher than 300 J/mm^3 are needed to bring the Zn amount in the prescribed range. This suggests that the Zn concentration in the initial powder could be slightly decreased, as further discussed in the next sections. Even with this caveat, we demonstrated that enriching the initial powder of volatile elements is a viable strategy for achieving compositional accuracy in LPBF-processed 7xxx series aluminum alloys.

1.3.2. Porosity Analysis

Metallic AM components are known to exhibit porosity, which results in limited ductility and reduced fatigue life[135]. Hence the relative density (defined as 100% - porosity%) is a key metric for process optimization. The ICP-MS composition measurements shown in Figure 1.4 indicate that samples processed at different energy densities have different compositions and therefore different theoretical densities, complicating determination of the relative density. To address this challenge, the compositional information determined by ICP-MS was used as the input for CALPHAD equilibrium calculations to determine the theoretical density of each sample. The experimentally measured density of each sample (Figure 1.6a) was then divided by its calculated theoretical density to determine the true relative density of each sample (Figure 1.6b).

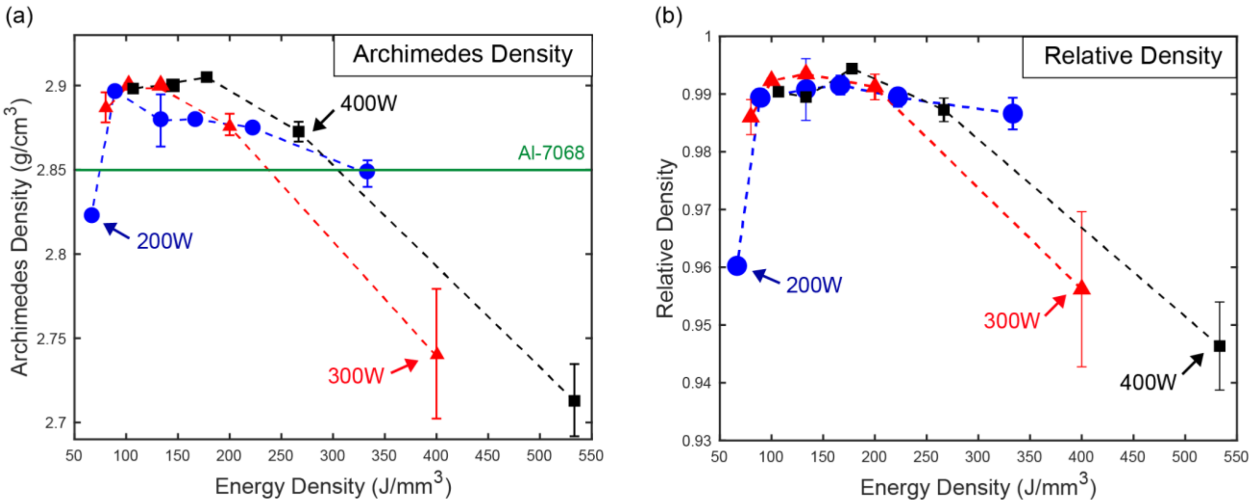

Figure 1.6. (a) Archimedes density and (b) relative density as a function of energy density.

For all sample compositions evaluated, CALPHAD predictions showed that the desired FCC-Al and $MgZn_2$ precipitate phases are stable across solid state temperatures, with no additional deleterious phases. Thus, process parameters for the larger prints were optimized simply to maximize relative density (i.e., minimize porosity), based on the data collected on the smaller prints (Figure 1.6b). The optimal energy density along the *200W* curve is obtained for E_D = 166.6 J/mm^3, resulting from a scan speed of 400mm/s; the optimal energy density along the *400W* curve is obtained for E_D = 177.7 J/mm^3, resulting from a scan speed of 750mm/s. These optimal parameters are henceforth adopted for large scale prints, to be used for microstructural analysis, CT analysis, and mechanical testing. Both optima are practically identical in chemistry (10.5% Zn and 2.7% Mg for the *400W* condition, and 10.3% Zn and 2.7% Mg for the *200W* condition). The full composition for every sample is shown in Table S1.1. in the supplementary information.

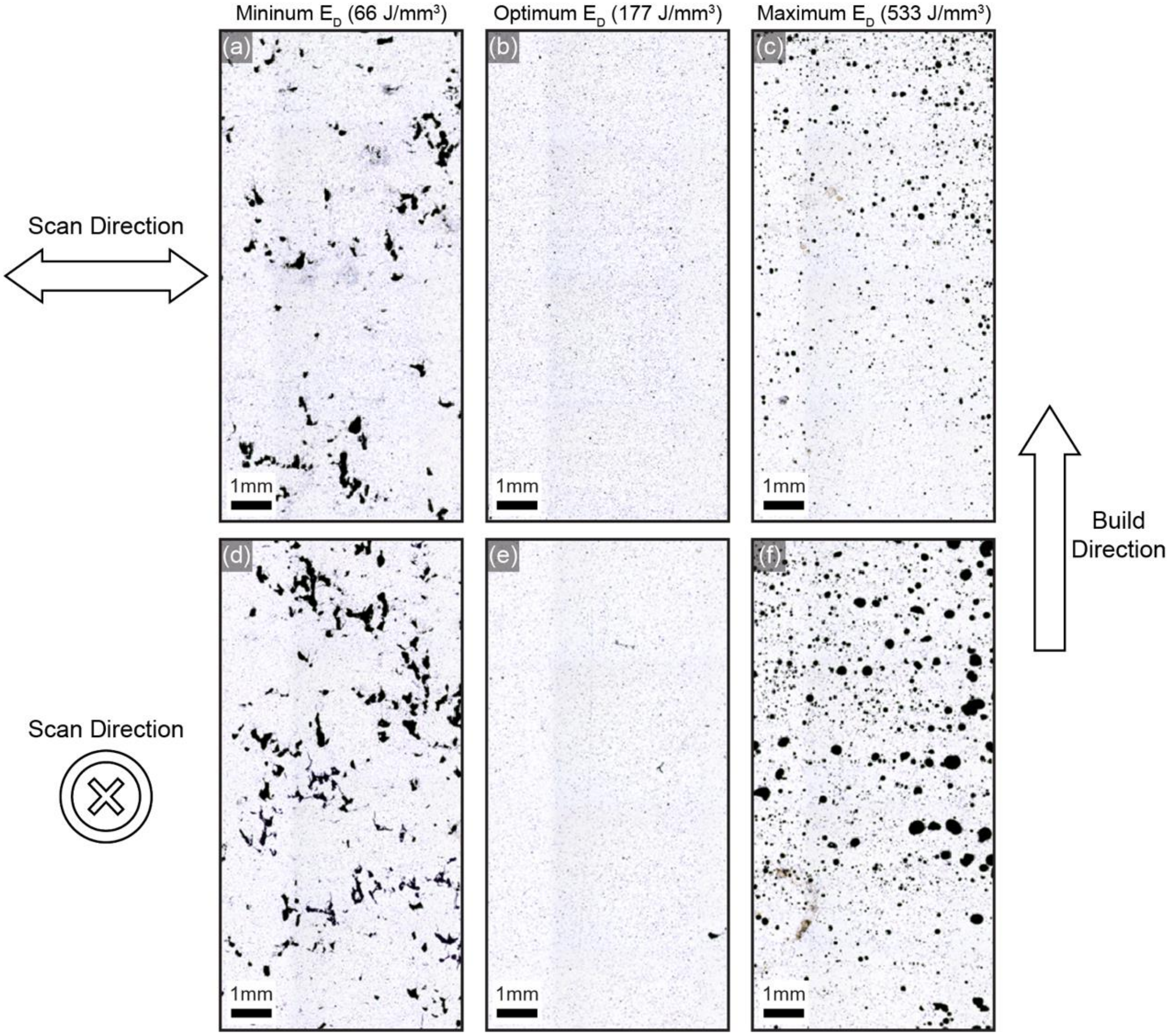

Figure 1.7. Representative optical micrographs of porosity morphology at (a), (d) the minimum energy density; (b), (e) optimal energy density; (c), (f) maximum energy density. The scan directions are noted.

The amount of porosity observed in each sample (Figure 1.7) confirms the trends in density discussed above and quantified in Figure 1.6. Figures 1.7a and 1.7d exemplify the lowest E_D value, where lack of fusion porosity between consecutive build layers and between adjacent scan lines are present. Figures 1.7b and 7e show prints produced with optimal E_D, resulting in 99.6% relative density, verified by CT imaging. Finally, Figures 1.7c and 1.7f show parts produced with the maximum E_D, leading to uncontrolled turbulence in the melt pool causing keyholing and large circular pores. The increased evaporation rate present in the alloy also led to gas porosity across the entire processing range, but most notably at maximum E_D. The trend of lack of fusion at low E_D values and keyholing at high E_D values is consistent with literature on LPBF processing[27,29].

The optimal process parameters for *200W* and *400W* conditions were used to print the larger sized tensile builds. The central portion of these larger builds were sectioned using EDM for CT imaging (shown in Figure 1.3a). CT data was used to quantify the pores' size and distribution. CT imaging shows similar relative densities when scaling up from the small 5x5x10mm builds to the larger 12x100x30mm tensile builds. Figures 1.8a and 1.8e are digitally reconstructed 3D volume renderings of the *400W* parameter set prints of the small build and large build, respectively. Figures 1.8b and 1.8f show the pore distribution along the build height, in the small and large builds, respectively. No trend in porosity distribution along the build height is observed. Figures 1.8c and 1.8g show the distribution across the scanning and recoating direction (referred to as the X-Direction), in the small and large builds, respectively. Both builds have a bimodal pore distribution along the X-Direction. Figures 1.8d and 1.8h show porosity radius histograms, in the small and large builds, respectively. The median pore radius of the large build is twice that of the smaller build, 101µm vs 43µm, respectively.

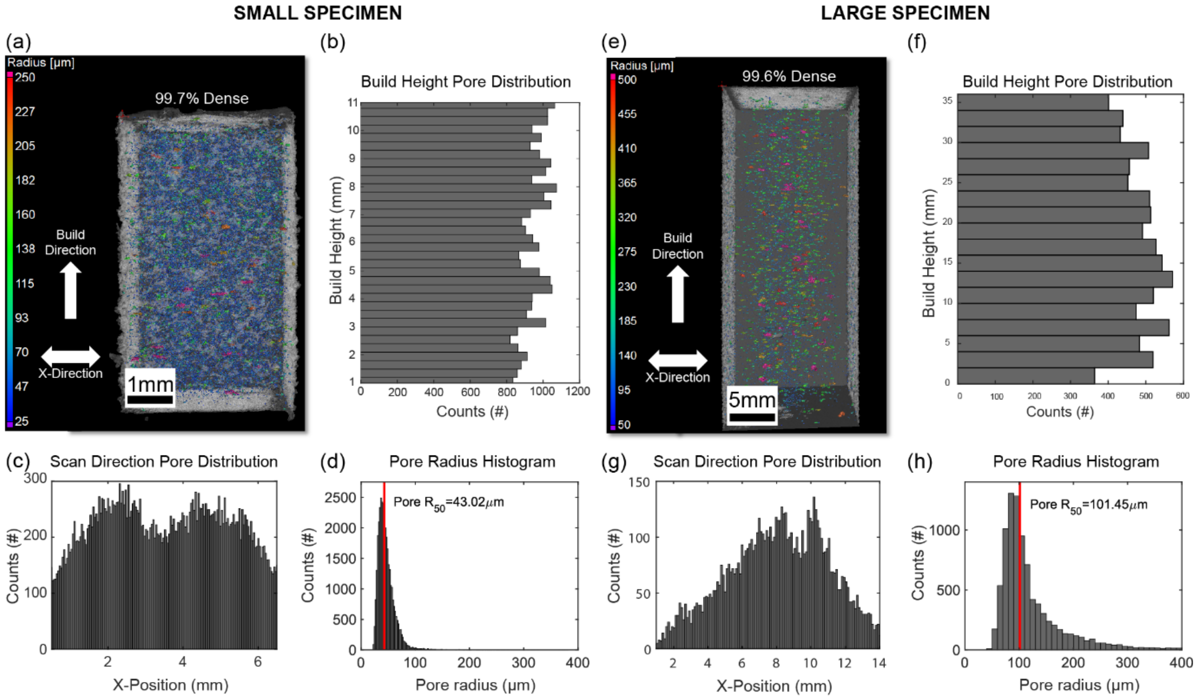

Figure 1.8. CT porosity measurements for *400W* specimens: 3D reconstructions of the (a) small and (e) large builds. Porosity distributions across the build height of the (b) small and (f) large builds. Porosity distributions along the recoat/scan direction of the (c) small and (g) large builds. Pore radius histogram across the (d) small and (h) large builds.

One possible explanation for the increased porosity size in the large build is an increase in powder spatter, as the larger build layers have nearly a 50X increase in cross-sectional area compared to the small build layers. Powder spatter disrupts the recoating process and creates pores as large as several powder particles, spanning multiple build layers. The powder spatter on the surface of each layer interferes with the bi-directional recoating process and gets swept towards the middle of the build, from each side (see Figure S1.2 and Video S1). This could also explain the bimodal pore distribution in the X-direction, observed in Figures 1.8c and 1.8g. This bimodal porosity distribution across the recoating direction is not observed in CT imaging of previously investigated LPBF alloys[136,137], strongly suggesting the connection for the increase in spatter from increased evaporation.

The measured porosity from CT imaging is within 0.3% of Archimedes density measurements for both the large and small builds. Even at the optimal energy input yielding a 99.7% dense sample, porosity is still present due to spattered powder (Figure S1.2 and Video S1). High speed imaging of the printing process has previously shown the vapor flux plume created during evaporation of constituent elements to be the main driver of ejected powder spatter[138]. Indeed, a large increase in spatter for the presently printed alloy processed via LPBF can be expected, as the print evaporated 8% of its total mass during printing. The effect of spatter-induced defects on mechanical properties, and their evolution throughout processing, is discussed in section 1.3.4.

1.3.3. Microstructural Evolution and Phase Analysis

The XRD patterns of the optimal *400W* sample presented in Figure 1.9 allow clear identification of the phases at each processing step. Figure 1.9b shows a slight diffraction peak shift towards higher angles of the $MgZn_2$ phase after printing compared to the powder feedstock, attributed to the loss of Mg and Zn during processing: as more Al substitutional atoms occupy lattice sites in the intermetallic $MgZn_2$ phase (predicted by CALPHAD calculations), the smaller Al atoms decrease the lattice plane spacing, thus increasing the diffraction angle. The TiC peak angles remain stable throughout processing, as shown in Figure 1.9c.

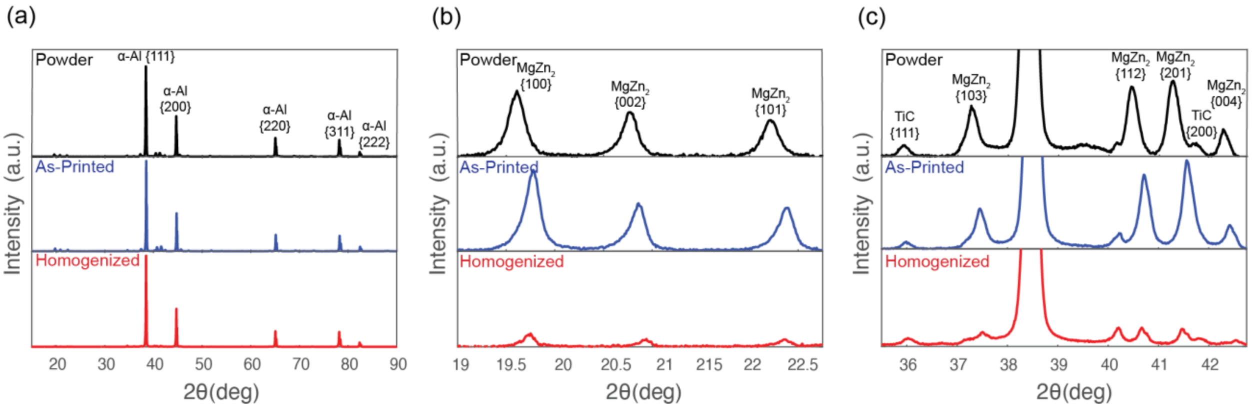

Figure 1.9. (a) Full range of XRD peaks observed in the feedstock powder, as-printed and homogenized *400W* sample. (b) Zoomed view of the 19-23° range, showing nearly complete homogenization. (c) Zoomed view of the 36-42° range, showing near full homogenization and the TiC stability.

Microstructural analysis was conducted on the initial feedstock powder and on samples printed with different processing conditions to understand the effect of processing on microstructure. Figure 1.10 shows representative microstructures for the powder feedstock (Figure 1.10a), as-printed (Figure 1.10b) and homogenized (Figure 1.10c) samples, printed with *400W* optimal parameters. All SEM-BSE micrographs clearly show three different phases, with the grey-scale intensity correlating with atomic mass. The phases from brightest to darkest are η-$MgZn_2$, TiC, and α-Al, with CALPHAD-predicted densities of 5.11g/cm^3, 4.93g/cm^3, and 2.71g/cm^3, respectively. EBSD analysis (Figure S1.5) confirmed that the equiaxed α-Al grains observed in Figure 1.10 are individual grains separated by distinct $MgZn_2$ intermetallic regions, without the presence of a larger columnar grain texture. The α-Al grain sizes are similar in both the feedstock powder and in the as-printed conditions, at 1.57 ± 0.55μm and 1.61 ± 0.79μm, respectively. This microstructure is consistent with the similar cooling rates achieved in gas atomization and LPBF[20]. A full homogenization window was not observed, with 1.6% volume $MgZn_2$ intermetallic remaining after homogenization (Figure 1.10c), which agrees with CALPHAD predictions. The comparison between the experimentally measured post-homogenization $MgZn_2$ volume fraction and the CALPHAD predicted remaining intermetallic fraction immediately below the solidus temperature is quantified and shown in Table 1.3. In addition to appearing at α-Al grain boundaries, spherical $MgZn_2$ intermetallic particles are present within the α-Al grains in the as-printed condition. These additional particles are attributed to the build continuing to equilibrate on the 200°C heated substrate for several hours while the entire print is completed. During the printing process, the solidified material is exposed to sufficiently high temperatures to enable diffusion of solute elements saturated in the α-Al grains due to the high solidification rates achieved. This diffusion leads to the uniform precipitation of spherical $MgZn_2$ intermetallic particles in the matrix. Figures 1.10a-c confirm that the TiC particles remain stable throughout the LPBF process. TiC in the as-printed condition is mostly observed along the grain boundaries, bonded to the intermetallic phase due to low lattice-plane mismatch, with some TiC also present within the α-Al grains (Figure 1.10b). TiC agglomerates are 530 ± 270 nm, 590 ± 180 nm, 630 ± 400 nm in the powder, as-printed, and homogenized samples respectively; however, TEM observations (Figure 1.11) show that the TiC nanoparticles form agglomerates made up of smaller particles, with an average diameter of 180±83 nm.

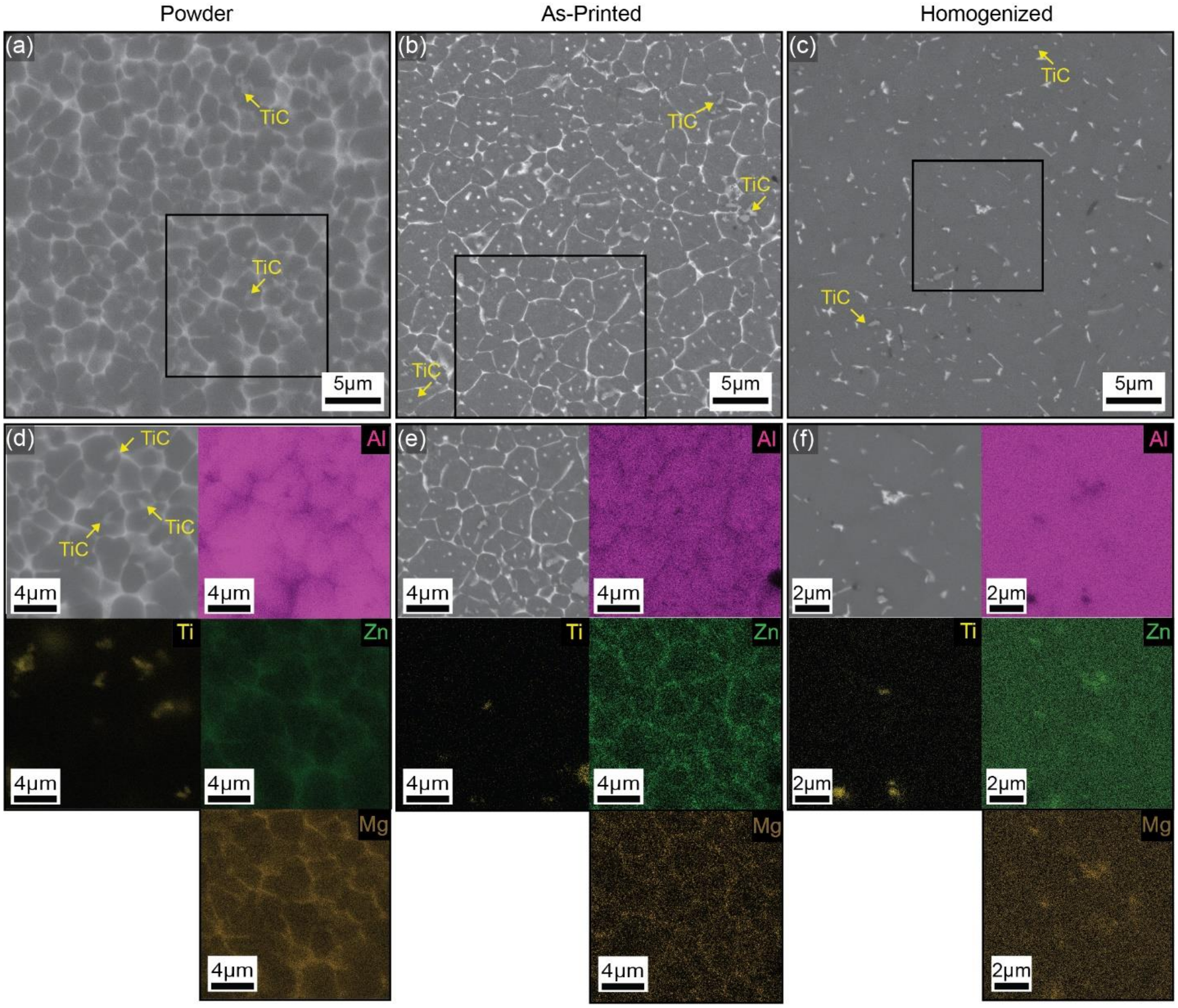

Figure 1.10. Representative SEM-BSE micrographs of (a) the feedstock powder, (b) the as-printed and (c) homogenized *400W* specimen. Representative EDS showing phase constituents in (d) powder, (e) as-printed and (f) homogenized samples. The build direction is upwards.

Table 1.3. Volume percent of the intermetallic phase: experimental measurements versus CALPHAD predictions.

	SEM As Printed	**CALPHAD 200°C Equilibrium**	**SEM Homogenized**	**CALPHAD 465°C Equilibrium**
Volume $MgZn_2$ (%)	9.3	9.3	1.6	1.8

The as-printed microstructure shown in Figure 1.10b clearly illustrates an equiaxed grain structure, confirming that columnar grain growth (a precursor to hot cracking) is avoided by the addition of TiC nanoparticles in the alloy. TiC nanoparticles act as heterogeneous nucleation sites within the melt pool, as the TiC particles are located within the α-Al grain. A high-resolution TEM (HRTEM) image of at the TiC/Al interface is given in Appendix 2 (Figure A2.1). Previous work has also verified coherent bonding between the planes of the intermetallic phase and TiC through HR-STEM in a nano-treated Al-7075 weld filler[112]. Additionally, Li *et al.* have observed an increased nucleation rate of cast Al-7075 with TiC compared to Al-7075 without TiC[35]. Restriction of the solidification front is also observed as TiC is located at the grain boundaries along with the $MgZn_2$ phase. This is due to TiC's high melting point and its stability in the melt pool throughout LPBF processing.

Selected samples for mechanical testing were additionally treated with HIP prior to homogenization and aging treatments. TEM micrographs of the *400W* optimal parameter samples in different heat-treated conditions are shown in Figure 1.11. Excessively large, elongated precipitates of η-$MgZn_2$ are clearly shown along the grain boundaries in the as-printed condition in Figures 1.11a and d. The HIP treatment was subsequently performed at 400^{o}C, which is lower than the maximum solubility homogenization temperature (465^{o}C). As the alloy is super-saturated, much of the Zn and Mg coalesces into the larger $MgZn_2$ precipitates during HIP treatment, leading to coarse regions of $MgZn_2$ at the grain boundaries. The post-HIP homogenization solutionizes most of the Mg and Zn from the overaged intergranular spherical $MgZn_2$ precipitates, back into the matrix, as shown in Figures 1.11b and e. The final strengthening heat treatment (24-hour ageing at 130^{o}C) reforms the nanoscale $MgZn_2$ precipitates, as shown in Figures 1.11c and f. The mean radius and spacing of the $MgZn_2$ precipitates and TiC nanoparticles are reported in Table 1.4. The strengthening effects of both the $MgZn_2$ precipitates and TiC nanoparticles in the different heat-treated conditions is discussed in section 1.3.4.

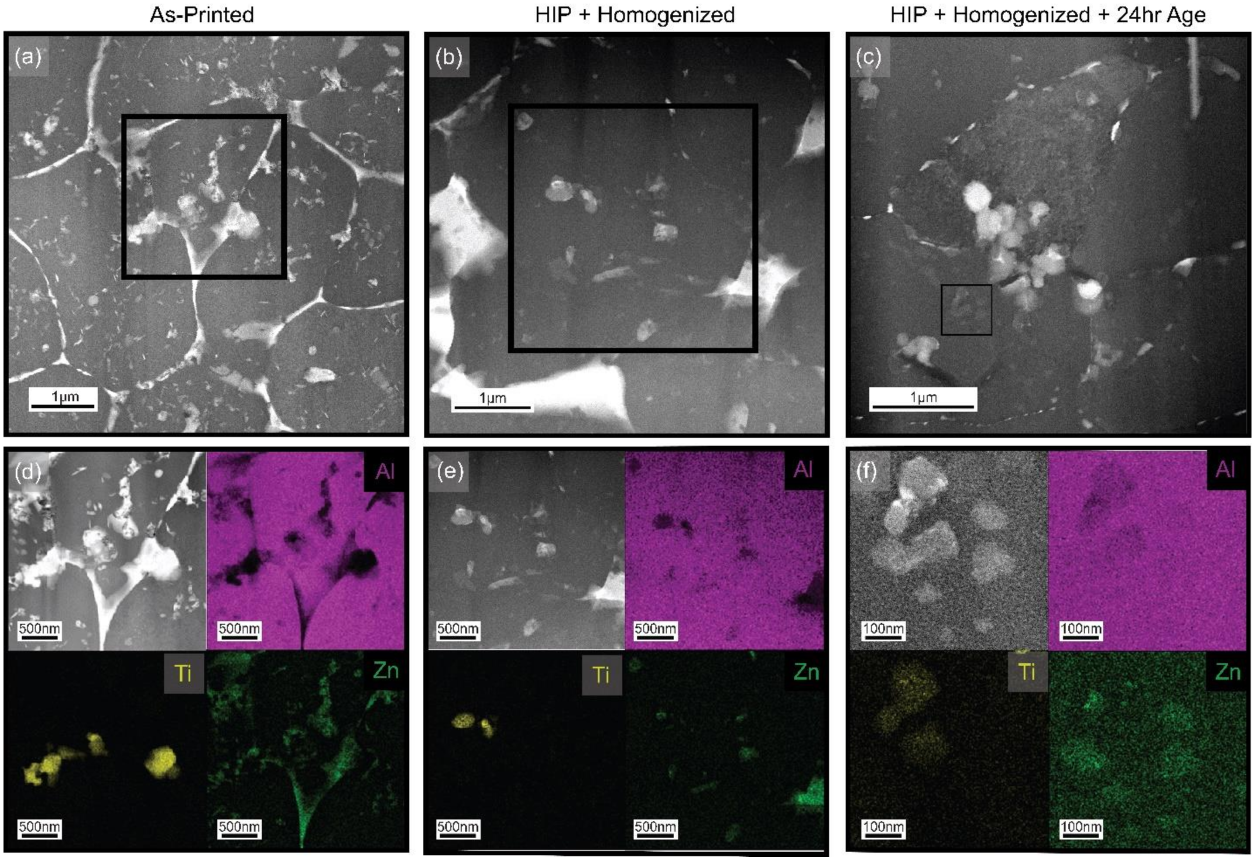

Figure 1.11. (a)-(c) STEM micrographs showing the phase distributions and (d)-(f) STEM-EDS measurements showing the TiC and $MgZn_2$ phases ,in the as-printed, HIP + homogenized, and HIP + homogenized + 24hr aged samples, respectively.

Table 1.4. TEM measurements of average precipitate diameter and spacing.

Sample	Precipitate Type	Average Diameter $2\bar{r}$ (nm)	Mean spacing λ_p (mm)
Homogenized + HIP	TiC	180	6
	$MgZn_2$	125	0.311
Homogenized + HIP + 24hr aged	TiC	180	6
	$MgZn_2$	48	0.079

1.3.4. Mechanical Behavior

The mechanical properties of LPBF-processed samples were measured via tensile testing, to reveal the effects of processing parameters, heat treatments and HIP on strength and ductility. Figure 1.12 shows representative stress-strain curves for all processing conditions tested. The results are provided in Tables 1.5 and 1.6, for the *200W* and *400W* samples, respectively. For

Tables 1.5 and 1.6, For both print conditions, homogenized samples show yield strengths $\sigma_{\mathrm{y}}{\sim}370$ MPa and strains to failure $\varepsilon_{\mathrm{f}}{\sim}4\%$. HIP has a relatively small effect on the yield strength but increases strain to failure; i.e., $\varepsilon_{\mathrm{f}}{\sim}6\%$ for the *400W* print condition. While this increase is consistent with porosity closure (Figure S1.4), HIP is not sufficient to provide the 11% elongation typical of wrought Al-7068[139,140].

Aluminum 7xxx series alloys are precipitation hardened, with optimally sized and distributed $MgZn_2$ precipitates increasing both yield strength (σ_{y}) and ultimate tensile strength (σ_{ult}), albeit at the cost of reduced ductility. In this work, all aging treatments were performed at 130°C, with a peak aging time of 24 hrs determined by hardness micro-indentation (Figure S1.1). The length of the peak aging treatment is in good agreement with reported data for wrought 7xxx alloys[139,141]. The effects of peak 24 hrs aging and HIP on strength and ductility are reported in Figure 1.12. As expected, for both *200W* and *400W* printing conditions, peak aging increases the strength significantly (up to a maximum $\sigma_{\mathrm{y}}{\sim}650$ MPa when combined with HIP treatment), but substantially embrittles the alloy.

There are no clear differences in properties when comparing the optimal settings printed with the *200W* and *400W* conditions. As both conditions had nearly identical energy densities (E_D = 166.6 J/mm^3 for the *200W* sample and E_D = 177.7 J/mm^3 for the *400W* sample), E_D emerges as a solid metric to predict part density and mechanical properties achievable during LPBF processing of 7xxx Al alloys.

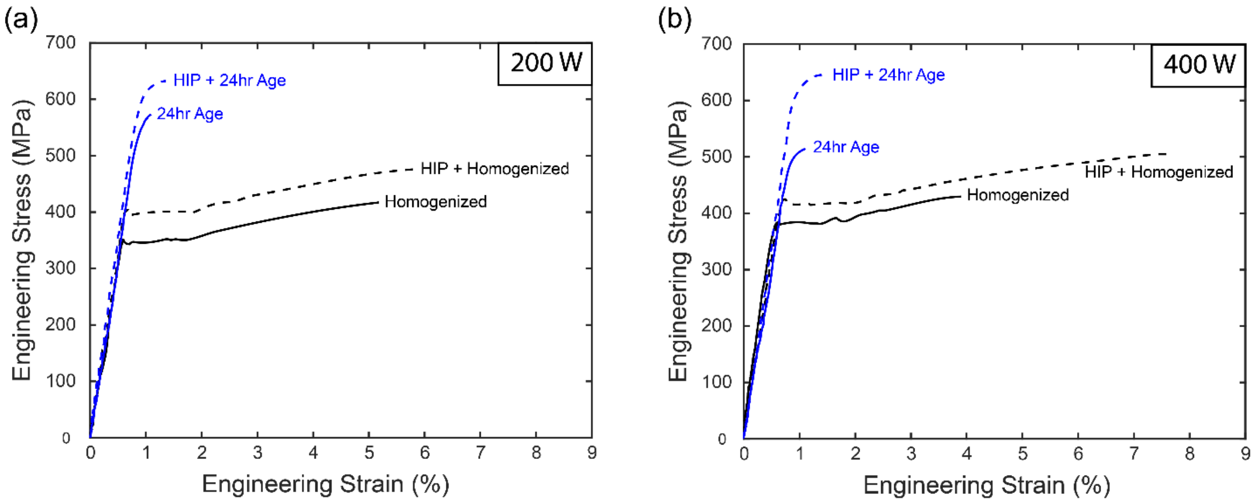

Figure 1.12. Representative tensile curves for optimal (a) *200W* (b) *400W* samples in the homogenized and 24hr aged conditions, with and without HIP.

Table 1.5. Tensile properties of samples printed with the *200W* conditions (* only one test exceeded yielding)

200W	**σ_y (MPa)**	**σ_{ult} (MPa)**	**ε_f (%)**
Homogenized	367±61.5	443±45	3.9±1.8
Homogenized + HIP	343±71	419±97	4.3±1.7
24hr Aged*	573±0	579±0	1.2±0
24hr Aged + HIP	569±55	579±77	1.5±0.1

Table 1.6. Tensile properties of samples printed with the *400W* conditions (* only one test exceeded yielding)

400W	**σ_y (MPa)**	**σ_{ult} (MPa)**	**ε_f (%)**
Homogenized	371±38	421±41	3.9±0.2
Homogenized + HIP	394±22	465±56	6±2.3
24hr Aged*	512±0	551±0	1.0±0
24hr Aged + HIP	557±78	568±112	1.5±0.1

The limited effect of HIP treatment on mechanical properties was unexpected, as porosity is generally responsible for the low ductility of LPBF-processed materials. Figure S1.4 confirmed that HIP treatment resulted in near-total elimination of internal porosity in all samples. The contributing strengthening mechanisms in different conditions is discussed below and in detail in Appendix 2.

Figure 1.13 is representative of the observed defect evolution throughout LPBF processing. EDS of oxide defects are shown in Figures 1.13d-f. Figures 1.13a and 1.13d show that within the as-printed pores, there is an increase in Zn, Mg, and O content throughout the pore. Figures 1.13b and 13e show that HIP successfully reduces the size of the pores as expected; however, oxide inclusions persist throughout the processing steps (Figure S1.4 additionally shows HIP fully reduced porosity). Figures 1.13c and 1.13f show that the areas enriched with oxide inclusions are the locations where fracture initiates and propagates. Figure S1.3 additionally compares the brittle fracture surface shown in Figure 1.13c with that of a more ductile sample printed and aged with the same conditions. It should be noted that the difference in scale bar size between Figures 1.13a and Figure 1.13b is due to HIP-induced pore closure.

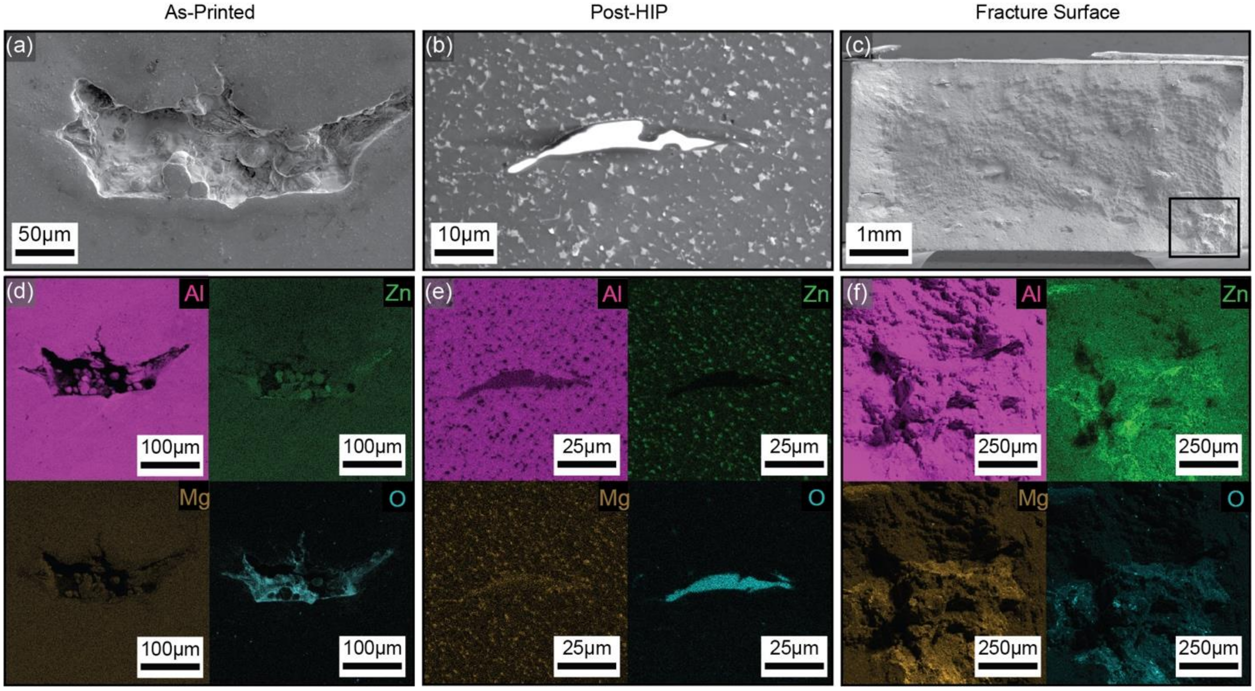

Figure 1.13. Representative SEM and EDS of defects in the *400W* sample: (a,d) a pore in the as-printed condition, with oxide and Zn, Mg accumulation; (b,e) an oxide inclusion in the post-HIP condition; (c,f) the fracture surface of a post-HIP sample showing beach marks propagating from a region with overall increased amount of oxygen, along with oxide inclusions.

There is a wide variance in ductility in each condition, quantified in Tables 1.5 and 1.6, attributed to the presence of defects introduced during spattering. Since this variance similarly occurs in the post-HIP condition, the defects causing ductility variance and premature failure are not the pores themselves, but rather oxides that may be deposited during spatter. Both our fracture surfaces and large pores are observed to have similar discolorations. Confocal micrographs of the fracture surface in Figure 1.13c are shown in Figure S1.3, highlighting the discoloration and defect accumulation in the most brittle specimens. While most of the spatter and vapor are flown into an outlet filter via a laminar gas flow inlet pressure, much of the spatter inevitably lands on the print, enriching the pores with Zn and Mg oxides. Images of these spattered particles after the recoating process are shown in Figure S1.2.

The exceptionally high strengths achieved in this modified alloy warrant discussion into the specific roles of multiple strengthening mechanisms, including grain boundary or Hall-Petch strengthening ($\Delta\sigma_{\mathrm{gb}}$), solid-solution strengthening ($\Delta\sigma_{\mathrm{ss}}$), dislocation strengthening ($\Delta\sigma_{\mathrm{dis}}$), and/or precipitate/dispersoid strengthening ($\Delta\sigma_{\mathrm{Orowan}}$). The contributions of each strengthening mechanism to the yield strength of the alloy, before and after the aging process, can be analytically estimated (see Appendix 2 for details) and are illustrated in Figure 1.14, in comparison with experimentally measured values.

Remarkably, we find that the calculated yield strengths are within 15% of the experimentally determined yield strength values for the HIP'ed and homogenized alloy, and within 2% for the 24-hour aged alloy. Dislocation strengthening may be anticipated to make a large contribution, as fast solidification rates in LPBF result in high dislocation density values. Additionally, both grain boundary and solid solution strengthening are expected, due to the significant grain refinement induced by TiC and the large additions of Zn and Mg, which are well above the ranges for conventional 7xxx Al alloys. The calculated effect of Orowan strengthening in the HIP + Homogenized condition is small, as the majority of Mg and Zn is solutionized and has not been aged into nanoscale η-$MgZn_2$ precipitates. Accurate precipitate radii and spacing for the larger elongated particles along the grain boundaries are difficult to quantify, thus leading to variances between the theoretical calculations and experimental measurements. Precipitation strengthening due to TiC particles is only responsible for $\Delta\sigma_{orowan}$ ~4MPa, which can be linked to the large spacing of 6μm between TiC agglomerates, with the remaining Orowan strengthening due to the larger $MgZn_2$ phases at grain boundaries and smaller $MgZn_2$ precipitates that did not fully solutionize during the homogenization treatment. However, the TiC nanoparticles do provide a significant grain boundary strengthening effect overall, by restricting grain growth during homogenization at 465^{o}C, leading to relatively high strengths even without aging. When aging at 130^{o}C for 24 hours after HIP + Homogenization, much smaller η-$MgZn_2$ phase precipitates form, with a much closer 79nm inter-precipitate spacing, leading to substantial Orowan strengthening in comparison to the homogenized sample. Overall, the ability to maintain high precipitation strengthening and solid solution strengthening associated with 7xxx series Al alloys by compensating for evaporation of Mg and Zn, along with TiC nanoparticles refining grain size and thus increasing grain boundary strengthening, result in a printable alloy with remarkably high strength.

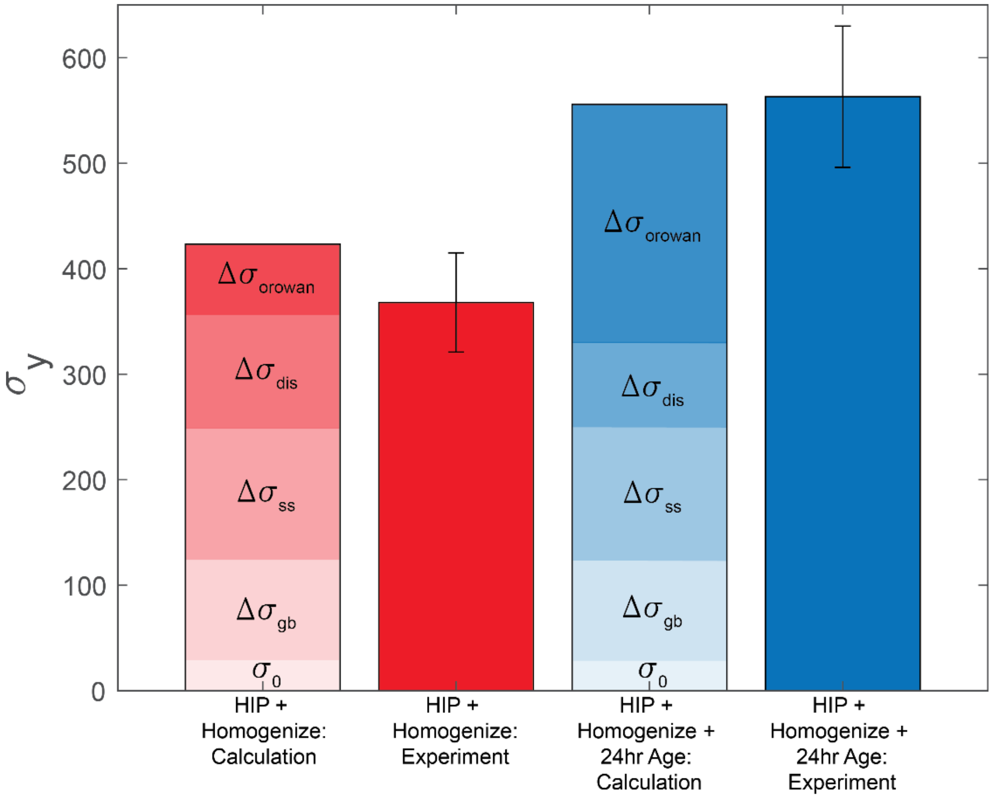

Figure 1.14. Comparison of the analytically estimated strengthening mechanisms with experimentally determined yield strength values, for the *400W* sample before and after aging.

1.4. Chapter 1 Summary and Conclusions

A modified Al-7068 alloy enriched with higher Zn and Mg content and TiC nanoparticles was designed and printed to eliminate hot cracking, improve mechanical behavior, and counter-act evaporation of volatile elements. The key conclusions can be summarized as follows:

(1) The TiC particles in the feedstock powder promoted equiaxed grains in the as-printed condition, avoiding hot cracking. TiC particles are present both within the grain (indicating heterogeneous nucleation sites) and at grain boundaries (indicating the grain restriction during solidification). This results in small grains and high grain boundary strengthening effect after conventional homogenization and aging treatments.

(2) A post-print target composition was achieved by counteracting the evaporation of constituent elements. This provided a near-optimal distribution of $MgZn_2$ precipitates upon homogenization and aging, resulting in a very significant Orowan strengthening effect.

(3) Simple analytical models of selective evaporation agree well with experimental measurements of compositions in samples printed at intermediate energy densities, when porosity is minimal and sample quality is maximal. CALPHAD calculations based on post-print compositions captures experimentally observed phase evolution and volume fractions. Collectively, these models can be easily applied to other alloy compositions, providing a valuable tool for the design of powders for LPBF of aluminum alloys strengthened by precipitates incorporating highly volatile elements.

(4) Lack-of-fusion and keyhole porosity mechanisms in the novel alloy used in this study are similar to those in previously reported LPBF-processed Al alloys. However, we observed an unusual bimodal porosity distribution along the recoating direction. This suggests that increased Mg and Zn evaporation causes ejected powder spatter onto the surface, which persists through HIP. Possible strategies to eliminate spatter-induced defects include increasing the gas inlet flow rate to remove spatter within the vapor plume Furthermore, reducing the concentration of Zn in the initial powder feedstock would enable printing at lower energy density, hence reducing elemental evaporation, spatter, and sample porosity.

(5) Optimally processed samples reach strengths comparable to wrought alloys, and much higher than those of previously LPBF-processed Al alloys. The presence of oxide inclusions, which are present even in HIP-treated specimens, results in low ductility. As we surmise that the larger oxides are mostly due to LPBF processing-induced spatter and elemental evaporation, the aforementioned strategies to reduce spatter would result in increased ductility. The presence of residual $MgZn_2$ precipitates at the grain boundaries after the aging process may also contribute to low ductility. Given the effectiveness of TiC in limiting grain growth, increasing the homogenization time may further remove $MgZn_2$ from the grain boundaries and help the alloy approach typical wrought standards.

2. Chapter 2. Microstructural Control of a Multi-Phase PH Steel

2.1. Introduction and Background

The intrinsic point-by-point nature of AM, combined with the enormous and location-dependent temperature gradients that affect laser and electron beam melting processes, present significant challenges in controlling residual stresses and achieving uniform microstructures across geometrically complex parts. Historically, much of the research in LPBF, EBM and DED has focused on tackling these challenges, while depositing materials with properties approaching (and occasionally exceeding) those of commercially available wrought or cast alloys[40,55]. While this approach has certainly facilitated adoption and certification of AM parts for several industries, a huge opportunity remains largely unexplored: the development of strategies to print heterogeneous 'designer microstructures', where composition and/or microstructure are locally controlled at the microscopic scale and tailored to optimize component performance. The ability to fabricate large-scale components with local microstructural control has the potential to revolutionize manufacturing.

AM techniques based on material deposition (including DED, FFF, MBJ) enable local control of composition via the use of multiple feedstocks, promising the most dramatic gradients in local material properties[142–145]. Beese *et al.* reviewed recent advances in additive manufacturing of metal functionally graded materials, highlighting the potential for multiple AM techniques to produce microstructures impossible to manufacture just a few years before[146]. Additionally, it has been well established that functionally graded lattice geometries can be printed to manufacture 'metamaterials' with bulk properties exceeding that of conventional monolithic materials[147,148]. The combination of gradations in material structure and gradations in part geometry, both enabled and unique to AM processes, will allow for the design of truly multi-scale optimized parts. While significant challenges exist when grading disparate materials particularly relating to the formation of undesirable brittle phases along compositional pathways, significant progress was made in DED of hybrid and functionally graded materials, with much research focusing on titanium/molybdenum[149,150], ferritic/austenitic steels[151], steel/Inconel,[152,153] and novel functionally graded structures with multiple intermediate compositions[154,155]. The formation of undesirable brittle phases is a challenge which is exacerbated when multiple principal element alloys are used, for which the complex multidimensional thermodynamic space is not fully explored.

With the exception of some recently introduced multi-material powder bed systems[77–79], most powder bed processes have uniform feedstock and do not allow compositional grading. Thus, the only possible route in LPBF is control of microstructural evolution is by local tailoring of the processing parameters. Recent progress in this field has shown significant ability to locally control the grain size, shape and texture, by manipulating the printing strategy to tune the direction of the temperature gradients upon cooling[80–85]. Mukherjee *et al*. have thoroughly reviewed and outlined the different methods for controlling the grain structure, phases, and defects in metal AM parts[86]. Most notably, Sofinowski *et al*. have introduced highly controllable layer-wise engineering of grain orientation (LEGO) microstructures, where the crystallographic grain orientation in LPBF 316L steel[87] and Ti-Nb[88] can be locally manipulated with great accuracy, by using the laser scan speed and printing strategy to manipulate thermal gradients. This capability has recently been further refined by Gao *et al*. through careful selection of the hatch spacing and remelting the same location from multiple laser scans. This allows for controlling the grain orientation texture of LPBF 316L at a resolution of 125μm[89]. Similarly, Plotkowski *et al*. have shown the ability to control grain texture and morphology in EBM Inconel 718 by locally tuning the amount of time the material is above the melting point, generating equiaxed and columnar microstructures on a point-by-point basis[90]. These approaches indicate the feasibility of manipulating the processing parameters to affect the resultant microstructures. However, the work to date does not result in significant spatial gradation in mechanical properties nor the ability to generate local microstructures with competing properties (e.g., strong/brittle VS soft/ductile)[80,88,91].

In this chapter, we propose an alternative approach for local microstructural control in LBPF, based on tailoring of volume fractions in multi-phase alloys. We demonstrate the potential of this approach on 17-4 precipitation hardening (17-4PH) stainless steel (Type 630, or UNS S17400). In its wrought form, 17-4PH is in the solutionized and quenched state (Condition A) in a fully martensitic microstructure and is subsequently precipitation-hardened to maximize strength and/or corrosion behavior[54,75,76,156].

A concentric borders scan strategy and a rotating stripe scan strategy were used respectively. Both studies printed with the same 3D Systems provided powder on a 3D systems ProX 300 LPBF printer, with energy densities of 53 and 56 J/mm^3, further highlighting the variability present in the as-printed microstructures between similar feedstocks printed under similar conditions. While the as-printed steel can always be solutionized and quenched back into a fully martensitic homogeneous microstructure, the high-property contrast between these phases in the as-printed condition may be exploited for local microstructural control. Here we show that we can locally control the volume fraction of martensite and ferrite by spatially varying the energy density during LPBF printing. We characterize the limit of the microstructures we can achieve while preserving nearly 100% density and demonstrate the ability to locally and systematically vary strength by ~20% and ductility by ~150% at a spatial resolution ~150μm. This enables the fabrication of metal-matrix-composites (MMC) with a hard/brittle BCT martensite phase and a soft/ductile BCC ferrite phase. While 17-4PH is used as a model material in this study, this approach applies to virtually all multi-phase materials, including titanium alloys, nitinol shape memory alloys, and especially in multiple principal element alloy systems in which phase stability and microstructural evolution are highly dependent on processing conditions[157–168]. This approach opens a vista of opportunities to manufacture metallic systems with locally tailored ‘designer microstructures’.

2.2. Methods

Nitrogen atomized 17-4PH powder from Carpenter Additive is used as feedstock for this study. The particle size distribution is between 20µm and 40µm. All samples are printed using a SLM Solutions 125HL printer, with the build chamber in a 99.99% Nitrogen atmosphere and the build substrate pre-heated to 200°C. A laser power of 200W, a layer thickness of 30µm, a hatch spacing of 100µm, and a scan strategy of “borders inside-out” are kept constant throughout the printing. Borders inside-out is a scan strategy in which concentric outlines (borders) of the parts are printed, from the smallest inside the core of the part towards the outer border of the part. The scan speed is varied from 166mm·s^{-1} to 1333mm·s^{-1}, to vary the volumetric energy density from 50 J/mm^3 to 400 J/mm^3. Energy density is calculated by $E = \frac{P}{v \cdot h \cdot t}$ where P is the laser power, v is the laser scan speed, h is the hatch spacing, and t is the layer thickness.

Wedge specimens are printed at 4 different energy densities (50, 100, 250 and 400 J/mm^3), and with two different printing directions (in the plane of the triangle and perpendicular to it). Thin-wall specimens (with single track and double track width) are printed vertically, with two different energy densities (100 and 400 J/mm^3). Dog-bone-shaped specimens are printed in the vertical direction, with three different printing conditions: E=100 J/mm^3 throughout, E=400

J/mm^3 throughout, and a hybrid ‘brick-and-mortar’ pattern, with harder (E=400 J/mm^3) prismatic bricks embedded in a softer (E=100 J/mm^3) matrix. Gradient blocks are printed with alternating layers at low energy density (E=100 J/mm^3) with layers at high energy density (E=400 J/mm^3), resulting in microstructural gradients parallel to the printing direction. Finally, hybrid specimens (the UCI logo and the soft core/hard shell cylinder) are printed with microstructural gradients parallel to the build platform: multiple energy densities in a single layer are achieved by interpenetrating two geometrical files, each printed with uniform energy density, in a single build.

Samples are removed from the build substrate via wire electro-discharge-machining (EDM). Post-processing heat treatments of the samples consist only of aging, without any solutionizing step. Samples are aged at 482°C for 60 minutes in a Nabertherm B400 furnace in ambient atmosphere with a heating rate of 10°C·min^{-1}, and then air quenched.

Microstructural analysis for lower magnifications is performed using an Olympus DSX10-UZH Digital Optical Microscope. Higher magnification microscopy is conducted using a TESCAN GAIA-3 Scanning Electron Microscope (SEM). Electron-Backscatter-Diffraction (EBSD) phase-distribution maps are acquired with Oxford NordlysMax3 detector, and the Kikuchi patterns are processed via Aztec software. Particle size distribution of the feedstock is imaged in secondary electron (SE) mode. Phase fractions are calculated using ImageJ Software. Samples are mounted in epoxy and polished using standard metallurgical procedures down to 0.05µm. To differentiate between the phases, samples are etched using Waterless Kalling’s, aka Kalling’s No.2 Reagent. Samples are submerged in etchant for 40s before immediately being rinsed, sonicated for 1 minute, and air dried.

Higher resolution microstructural characterization of the lattice structure and precipitates is conducted in a JEOL JEM-2800 scanning/transmission electron microscope (S/TEM) with a

Gatan Oneview camera, operating at a beam voltage of 200 kV. JEM-2800 is equipped with dual 100 mm^2 silicon drift detectors (SDD) for energy-dispersive X-ray spectrometry (EDS). TEM lamellae are extracted using a focused ion beam (FIB) in a Quanta 3D FEG dual beam SEM/FIB (Thermo Fisher Scientific Inc.).

Tensile tests are conducted on an Instron 5985 frame with a 250kN load cell. An AVE2663-901 video extensometer with a Fujinon HF16HA-1S lens is used to track the strain of the gauge section. Tests were conducted according to ASTM E8 standards at quasistatic strain rate of 0.001s^{-1}. Strain mapping via Digital Image correlation (DIC) is conducted using a Correlated Solutions system, and the captured speckle patterns are processed via Vic3D software. Vickers hardness measurements are taken with a 500g load held for 10s for each indent. Hardness maps are created with indents spaced 150μm apart, across the entire sample. A Wilson VH3300 automated indenter is used for mappings.

2.3. Results and Discussion

2.3.1. Phase Stability and Microstructural Control

It is well known that the quality of metal parts printed by LPBF is dramatically influenced by multiple processing parameters, most notably the laser power (P), the laser scan speed (v), the hatch spacing (h), the thickness of each powder layer (t) and the scan strategy (laser path). An intuitive combination of these parameters is the volumetric energy density (E), calculated as $E = \frac{P}{v \cdot h \cdot t}$, expressing the amount of energy deposited in a given volume of powder. For a given material, the ratio of E to the minimum amount of energy necessary to melt the powder strongly correlates with sample density[134,169]: low values of E cause excessive lack-of-fusion porosity, whereas excessively high E induces significant turbulence in the melt pool, resulting in keyhole porosity.

Both scenarios negatively affect mechanical properties, in particular ductility. Intermediate values of E generally yield maximum density and hence optimal mechanical behavior. To determine the processing window for 17-4PH steel, we print a number of wedge-shaped specimens along two different printing directions, over a range of energy densities between 50 and 400 J/mm^3 (see Figure S2.1 for geometric details). The 'borders inside-out' scan strategy is used in all our prints, whereby an outline of the shape is printed from the inside of the sample, followed by progressively larger adjacent outline scans until the final border is scanned. The results are shown in Figure 2.1, with porosity data reported in Table 2.1. Figure 2.1(a-d) and Figure 2.1(e-h) show optical images of the samples printed horizontally and vertically, respectively. Significant lack of fusion porosity is clearly visible in the samples processed at the lowest energy density (E=50 J/mm^3), regardless of the printing orientation. The vertically printed sample (Figure 2.1e) shows more porosity near the base, consistent with the higher heat flow induced by the vicinity of a large heat sink. All other samples are almost fully dense (porosity $\lesssim$ 0.1%), except for the vertically printed specimen at the highest energy density (E=400 J/mm^3), in which pores are visible near the tip. Indeed, this region is the furthest away from the heat sink, consistent with keyhole porosity. The conclusion is that 17-4PH steel presents a wide processing window, where near fully dense specimens can consistently be printed with energy densities in the range of 100-400 J/mm^3. This is in striking contrast with many conventional LPBF alloys, which enter the keyholing porosity regime at much lower energy densities[54,170].

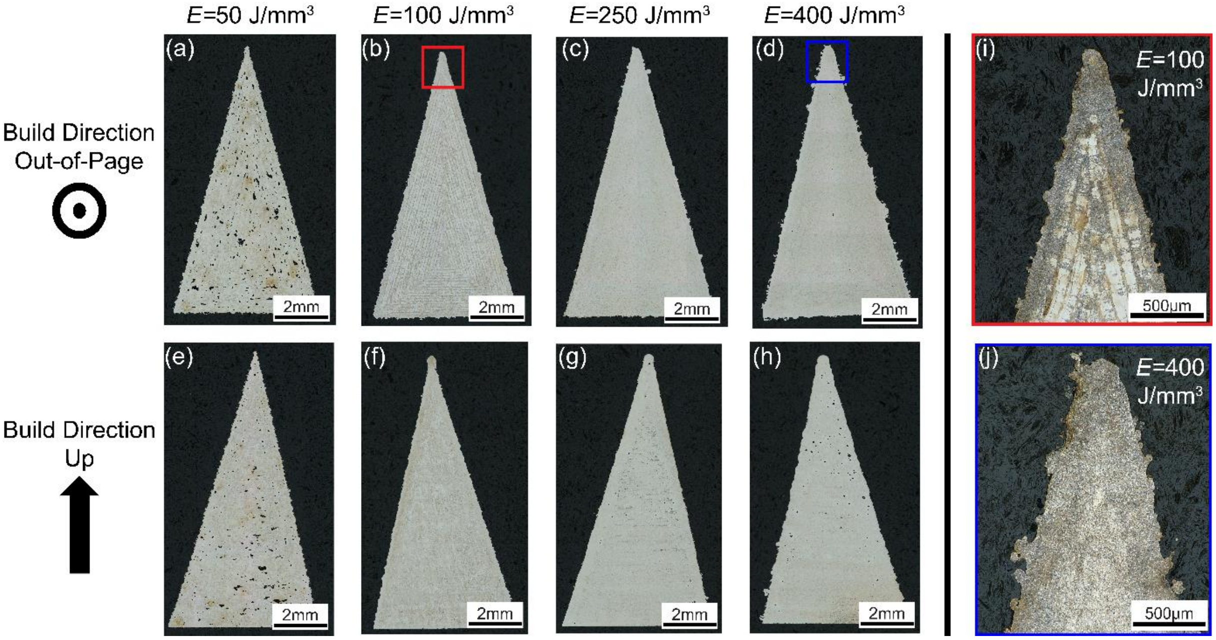

Figure 2.1. (a)-(d) Optical micrographs of wedge builds printed with an out-of-page build direction, increasing the energy density from 50 to 400 J/mm^3. (e)-(h) Optical micrographs of wedge builds printed with an upwards build direction, increasing the energy density from 50 to 400 J/mm^3. Higher magnification of wedge builds printed with an out-of-page build direction, showing dual phase versus martensitic microstructures corresponding to (i) E=100 J/mm^3 and (j) E=400 J/mm^3 respectively. (See Figure S2.1 for geometric details).

Table 2.1. Porosity of wedge samples as a function of energy density.

Porosity (%)	**E=50 J/mm^3**	**E=100 J/mm^3**	**E=250 J/mm^3**	**E=400 J/mm^3**
Build Direction Out-of-Page	2.6%	0.003%	0.003%	0.013%
Build Direction Up	1.5%	0.002%	0.088%	0.45%

The optical micrographs in Figure 2.1 have been etched to reveal microstructural details. A clear difference emerges between the samples produced at low (50-100 J/mm^3) and high (250-400 J/mm^3) energy densities, with the former showing a two-phase microstructure with finely spaced martensitic laths interspersed with larger grains between scan lines (Figure 2.1i), and the latter exhibiting a very uniform martensitic microstructure throughout the specimen (Figure 2.1j). All samples clearly show a uniform martensitic outer border, regardless of the printing conditions. As the outer border is printed last, this suggests that the initial solidification of any single laser scan has a sufficiently high cooling rate to induce a martensitic transformation. This is consistent with well-established estimates of cooling rates in a single LPBF laser scan of 10^4-10^7 °C·s^{-1}, which are much higher than the critical cooling rate needed to induce martensitic transformations in steels upon cooling from austenite, 10-100 °C·s^{-1}[20,21,159,171]. The larger grains present can be linked to retained ferrite[40]; in the present work, this is proposed to have formed through re-transformation upon reheating from an adjacent scan line. Since dual phase microstructures are only observed in our lower energy density prints, and fully martensitic microstructures are observed in our higher energy density prints, the reheating effect necessary to retransform martensite during adjacent scans is dependent on the processing parameters. The important conclusion is that two processing conditions exist (corresponding to E=100 J/mm^3 and E=400 J/mm^3) that result in fully dense specimens with remarkably different microstructures, clearly indicating the possibility of microstructural control. These two processing conditions were selected for further analysis.

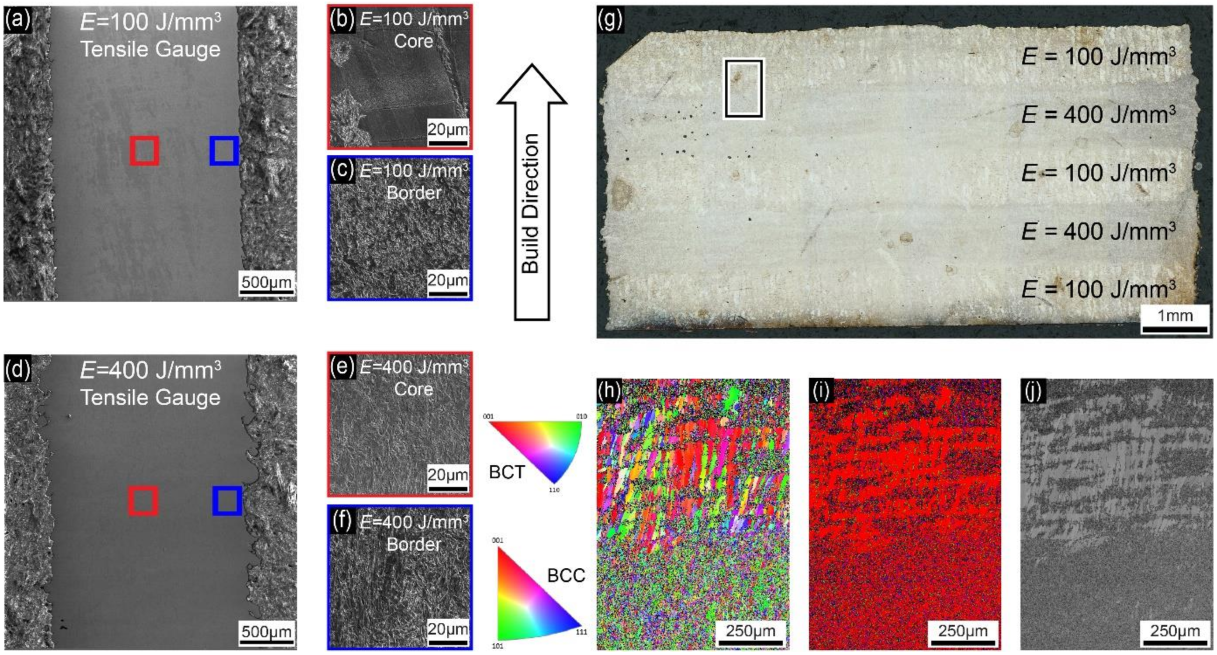

Figure 2.2. (a,d) SEM images of dual phase versus fully martensitic microstructures from gauge sections of dog bone specimens processed with E=100 J/mm^3 and E=400 J/mm^3, respectively. Microstructures of the inner core versus the outer border of the samples are shown in (b-c) for E=100 J/mm^3 and (e-f) for E=400 J/mm^3. (g) Optical image of an etched hybrid sample printed by alternating 1mm layers at E=100 J/mm^3 and 400 J/mm^3, with IPF-X maps, phase maps, and band contrast maps shown in (h-j) for the inset in (g), respectively. The build direction is upwards throughout the figure. (See Figure S2.1 for geometric details).

To further investigate the difference in microstructure between samples printed at different energy densities, 1mm-thick dog bone specimens are printed with E=100 J/mm^3 and E=400 J/mm^3, respectively. A larger specimen is fabricated with alternating 1mm-thick layers printed with E=100 J/mm^3 and 400 J/mm^3 conditions, allowing visualization of the interface between different processing conditions. (See Figure S2.1 for geometric details). Scanning Electron Microscopy (SEM) images of the dog bone gauge sections are depicted in Figure 2.2a and 2.2d. While the sample printed at lower energy density displays a martensitic border (Figure 2.2c) encompassing a two-phase core consisting of fine martensite intermixed with larger grains (Figure 2.2b), the sample printed at higher energy density shows a uniform martensitic microstructure (Figure 2.2e-f). This finding is consistent with the 'border-inside-out' printing strategy, as discussed above. The interfacial region between volumes printed with different energy densities is analyzed by Electron Back Scatter Diffraction (EBSD), with Figure 2.2h-j showing Inverse Pole Figure (IPF-X), phase map, and EBSD band contrast, respectively. The phase map (Figure 2.2i) confirms that the region processed with E=100 J/mm^3 (top half) has a dual phase microstructure, composed mainly of columnar ferrite grains (shown in red) and regions of martensite laths (shown in blue); by contrast, the region processed with E=400 J/mm^3 (bottom half) shows a fully martensitic microstructure. We note that the several red pixels indexed as ferrite in this region are due to the challenge in distinguishing between body centered cubic (BCC) ferrite and the low aspect ratio centered tetragonal (BCT) martensite, resulting in an EBSD detection limit of ~1μm, which is comparable with the laths dimension[53,54,172]. From the large area EBSD phase map (Figure 2.2i), ferrite fractions are measured as 79% and 28% in the regions processed with E=100 J/mm^3 and E=400 J/mm^3 respectively. While the phase fractions from the phase map in Figure

2.2i are not precise values, they nonetheless offer good estimates, and exclude the presence of austenite. Most importantly, Figure 2.2h-j clearly shows that regions printed with different energy densities consistently exhibit different (and repeatable) microstructures.

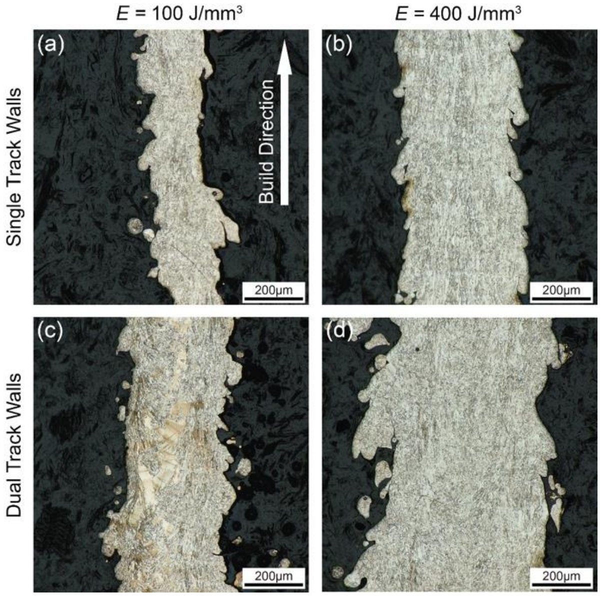

Figure 2.3. Single-track walls printed with (a) E=100 J/mm^3 and (b) E=400 J/mm^3. Dual-track walls printed with (c) E=100 J/mm^3 and (d) E=400 J/mm^3. Notice that ferritic grains are only present in the inter-hatch spacing in dual-track walls printed with the lower energy density.

To fully validate the hypothesis that powder always initially solidifies in a fully martensitic microstructure (regardless of the energy density), with dual-phase ferritic/martensitic regions developing into inter-hatch regions upon subsequent heating/cooling cycles in samples printed at lower energy density, we print simple vertical walls, either one or two laser tracks wide, with the two different energy densities, 100 and 400. The programmed hatching distance for the two-track walls is 100μm. Optical images of the etched specimens are shown in Figure 2.3. Notice that the width of single-track walls increases significantly with energy density, almost doubling from 158.8 ± 20.0μm at 100 J/mm^3 to 327.1 ± 22.4μm at 400 J/mm^3, implying that the remelted region between adjacent melt pools is significantly larger in the 400 J/mm^3 two-track sample than in the 100 J/mm^3 two-track sample. It should be noted that both single and dual-track walls printed at high energy density display a uniform martensitic microstructure, consistent with the results on all parts displayed in Figures 2.1 and 2.2. Single-track walls printed at low energy density also display a uniform martensitic microstructure, indistinguishable from that of the walls printed at higher energy density. Conversely, dual-track walls printed at low energy density show a clear martensitic border encapsulating a dual-phase microstructure in the core, with large ferritic grains extending through multiple print layers. Both the ferritic and martensitic phases are identical to those seen in the large-scale specimens (Figure S2.3). This clearly confirms that powder always initially solidifies in martensitic microstructure at all energy densities (consistent with the very fast cooling rates experienced in LPBF), and that the ferritic microstructure is formed in the hatch between adjacent scan tracks upon reheating – and only at low energy densities.

It is well known that vaporization of lower boiling point elements in LPBF melt pools is a function of energy density, potentially resulting in variations in alloy composition at different E values. We measure these differences via OES and perform Scheil solidification calculations with ThermoCalc (Figure S2.5). With the caveat that martensitic transformations are not accounted for in the model, we demonstrate that these compositional differences are not responsible for the observed differences in microstructure between samples printed with different energy densities reported herein. Fully elucidating the precise pathways that induce the martensite to ferrite solid phase transformation in the hatch upon the heating/cooling cycle requires a more complex combination of numerical modeling and experimental work, which is beyond the scope of this article. Our working hypothesis is that the temperature distribution and history is such that some volumes of material near the hatch get reheated to a temperature where the δ-ferrite phase is stable, inducing fast athermal transformation to the δ phase. Once nucleated, these grains no longer transform to martensite upon fast cooling, 'locking in' the ferritic microstructure. Extensive simulations of thermal history coupled with thermodynamic modeling and selected experiments are currently underway to verify this hypothesis.

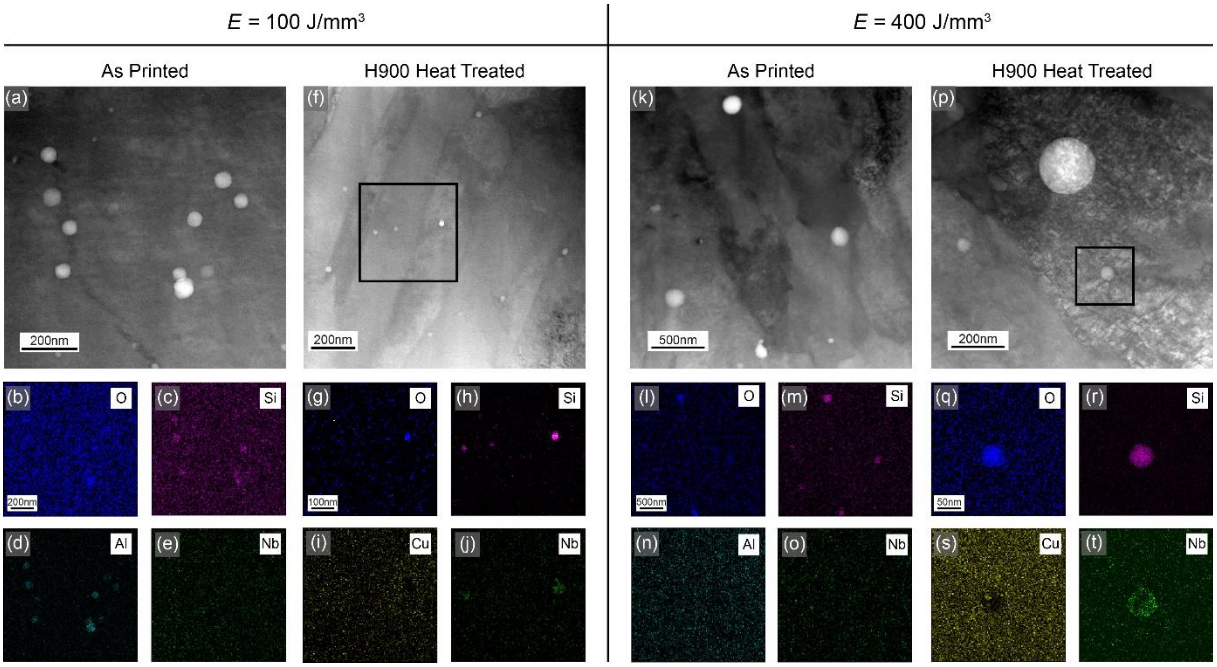

Figure 2.4. STEM and STEM-EDS images of a sample processed with E=100 J/mm^3 in the as-printed (a-e) and heat treated conditions (f-j), and a sample processed with E=400 J/mm^3 in the as-printed (k-o) and heat treated conditions (q-t). Nb-rich precipitates are visible in the heat treated samples.

In conventionally processed 17-4PH steel, the martensitic microstructure is introduced via solutionizing and quenching, and further enriched with Nb- and Cu-rich precipitates upon 1hr aging at 482°C (900°F), a thermal process denoted as H900[54,76,156]. In LPBF-printed and H900-treated 17-4PH, the nature and distribution of precipitates appears to depend on the printing conditions, in ways that have not been fully elucidated[60,173,174]. As solutionizing would effectively erase any gradient in microstructure intentionally introduced in our samples, in this study we eliminate this process and directly age the as-printed specimens. To verify the efficacy of this approach in generating precipitation-strengthened microstructures and identify potential differences as a function of the applied energy density, Scanning Transmission Electron Microscopy (STEM) and Energy Dispersive Spectroscopy (STEM-EDS) are performed on samples printed at E=100 and E=400 J/mm^3, both in as-printed and heat treated conditions (Figure 2.4). The TEM lamellae samples processed at E=100 J/mm^3 are taken from a large grained ferritic region, and those processed at E=400 J/mm^3 are taken from the martensitic region. Several important results emerge:

(i) Samples printed at lower energy density (Figure 2.4a and 2.4f) exhibit a much lower dislocation density than samples printed at higher energy density (Figure 2.4k and 2.4p), both before and after the aging process. This observation, combined with visual observation of the lath structure in the sample printed at a high energy density, confirms that samples printed at high energy density (400) have a martensitic microstructure, whereas the large grains observed in samples printed at lower energy density (100) are non-martensitic. TEM diffraction patterns from all samples (Figure S2.4) confirm the large grains to have a BCC ferrite structure (as opposed to FCC austenite).

(ii) STEM micrographs of both samples in the as-printed condition show large spherical particles (~50-150 nm in diameter) dispersed throughout the samples (Figure 2.4a and 2.4k). STEM-EDS identified these particles as alumino-silicates in the low energy density specimen (Figure 2.4b-e) and silicates in the high energy density specimen (Figure 2.4l-o). Similar silicate particles have been observed in LPBF-processed 17-4PH samples before, and reported as inclusions, as opposed to strengthening precipitates[62,68]. Upon aging, these particles appear to nucleate Nb-rich precipitates in samples printed at both energy densities (Figure 2.4j and 2.4t). Interestingly, no Cu-rich precipitates are visible in either sample.

(iii) Both the ferritic and martensitic microstructures remain unaltered after the aging process (except for formation of precipitates), confirming that this treatment maintains microstructural gradients intentionally introduced during printing.

In conclusion, the STEM investigation reveals that the aging process is successful in precipitating Nb-rich particles in microstructures printed with any energy density, without altering the martensite and ferrite distribution.

2.3.2. Mechanical Behavior

The ability to consistently program heterogeneous microstructures in samples of different shapes, dimensions and printing orientations is demonstrated in Figure 2.5. (See Figure S2.1 for geometric details). The low-energy density ferritic/martensitic microstructure and the high-energy density fully martensitic microstructures are clearly visible in the etched specimens via optical microscopy (Figure 2.5a-c). Note that the sample displayed in Figure 2.5a exhibits a microstructural gradient parallel to the printing direction, while the two are perpendicular in the samples shown in Figure 2.5b-c. Figure 2.5d-f displays hardness maps obtained by Vickers micro-indentation on the same samples. Moreover, the fully martensitic microstructure is consistently harder than the two-phase microstructure, with a difference that is more pronounced along the printing direction: while the fully martensitic region consistently displays a hardness of ~500HV, the dual-phase microstructure ranges in hardness from ~400HV along the print path (Figure 2.5d) to ~450HV in the perpendicular direction (Figure 2.5e-f). The dependence of the hardness on the printing orientation for the dual-phase microstructure is consistent with the highly elongated shape of the ferritic grains along the printing direction (Figure 2.2h).

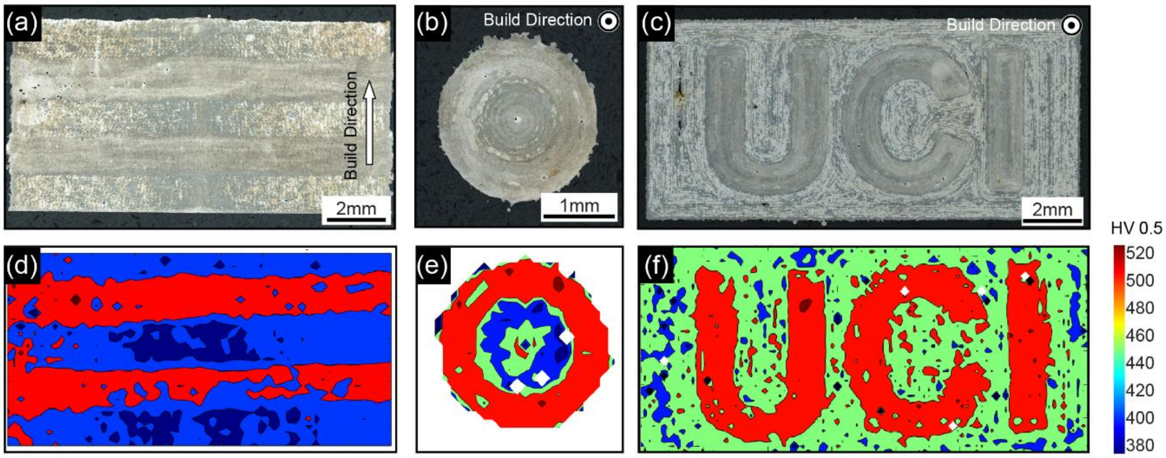

Figure 2.5. Optical images (a-c) and Vickers HV0.5 hardness maps (d-f) of etched hybrid samples: (a,d) a block printed by alternating 1mm-thick layers processed with E=100 J/mm^3 and 400 J/mm^3; (b,e) a cylinder printed with an E=100 J/mm^3 core and a 400 J/mm^3 outer shell; and (c,f) a block printed at 100 J/mm^3 encompassing the UCI logo printed at E=400 J/mm^3. (See Figure S2.1 for geometric details).

To investigate the scale of microstructural control, a gradient block sample is printed by alternating high energy density (E=400 J/mm^3) and low energy density (E=100 J/mm^3) regions of decreasing thickness, from 450μm down to 30μm (the thickness of a single print layer), along the print direction. An optical image of the etched sample is shown in Figure 2.6a-b. As detecting the boundaries between different regions becomes challenging as the regions get progressively thinner, a hardness map is produced in Figure 2.6c, with a scan across the gradient shown in Figure 2.6d. Note that differences in hardness are appreciable down to a thickness region of ~150μm (equivalent to ~5 print layers). As this value is partly determined by the resolution of our micro-indentation maps, it can be taken as a very conservative estimate of the scale of our microstructural control along the print direction. As the hatch spacing perpendicular to the print direction is 100μm, and microstructural differences are evident at this scale (Figure 2.1i), we expect the resolution perpendicular to the build direction to be of the order of 50-100μm.

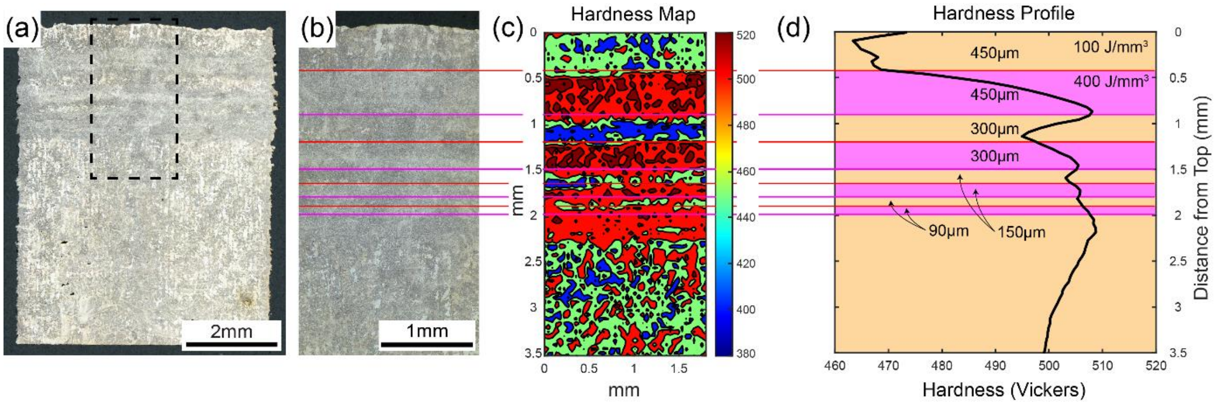

Figure 2.6. (a) Optical image of an etched hybrid sample, printed by alternating layers processed at E=100 J/mm^3 and 400 J/mm^3, with gradually lower thickness. The microstructural gradient is aligned with the printing direction. (b) Magnification displaying the microstructural differences between the layers. (c-d) Hardness map and hardness profile (averaged across the width) of region in (b), demonstrating a resolution for microstructural control of the order of 150μm. (See Figure 2.S1 for geometric details).

While non-instrumented indentation provides a high-throughput mechanism to ascertain the impact of microstructural features on mechanical properties as well as allowing rapid 2D mapping of large heterogeneous regions (Figures 2.5-6), it cannot capture all the information embedded in a full stress-strain curve extracted from a tensile test. To fully appreciate the impact of our microstructural control on the mechanical response of LPBF-printed 17-4PH components (and in particular on yield strength, ultimate strength, hardening behavior and strain to failure), we perform tensile tests on dog bone-shaped specimens printed with three different conditions: (i) samples printed with uniformly low energy density of 100 J/mm^3; (ii) samples printed with uniformly high energy density of 400 J/mm^3, and (iii) hybrid samples with a 'brick-and-mortar'-inspired architecture, embedding prismatic domains (bricks) printed with high energy density in a matrix (mortar) printed with low energy density (Figure S2.1 and S2.2). Ten nominally identical samples were tested for each processing condition. Stress-strain curves are displayed in Figure 2.7a, with average mechanical properties reported in Table 2.2. Several important results clearly emerge. The samples printed with low energy density exhibit substantial ductility (strain to failure ~18%), and yield and tensile strength of 1,151 MPa and 1,378 MPa, respectively. By contrast, the samples printed with high energy density are remarkably more brittle (strain to failure ~7%) but significantly stronger, with yield and tensile strength of 1,394 MPa and 1,561 MPa, respectively. Remarkably, these results are consistent across all samples tested, with most properties exhibiting variations of less than 2% (Table 2.2). The only exception is the strain to failure in the sample printed at higher energy density, which shows variations in excess of 30%; this is consistent with a brittle mechanical response and is likely exacerbated by the presence of keyhole porosity (Figure 2.1h). The hybrid sample printed with a ‘brick-and-mortar’ pattern displays intermediate characteristics, with strain to failure ~13% and yield and tensile strength of 1,213 MPa and 1,444 MPa, respectively. A full-field strain map obtained during the uniaxial test of a hybrid specimen by Digital Image Correlation (DIC) is shown in Figure 2.7b, clearly showing that plastic strain can be effectively localized in the softer domains.

Collectively, two key results emerge:

(a) By simple tuning of the energy density upon printing, we can generate two different microstructures, both yielding desirable but different mechanical properties. Both phases are easily printable with high quality and exhibit differences in yield strength and ductility of the order of 20% and 150%, respectively, which are much larger than variations achievable with any other previously demonstrated microstructural control strategy in LPBF.

(b) Functionally graded hybrid samples can be readily fabricated by interpenetrating domains printed with different conditions at a resolution of the order of 100μm. These hybrid printing strategies can be used to fully tune the mechanical response within the bounds presented by the two end microstructures, as well as a mechanism to localize plastic deformation in specific regions of the sample.

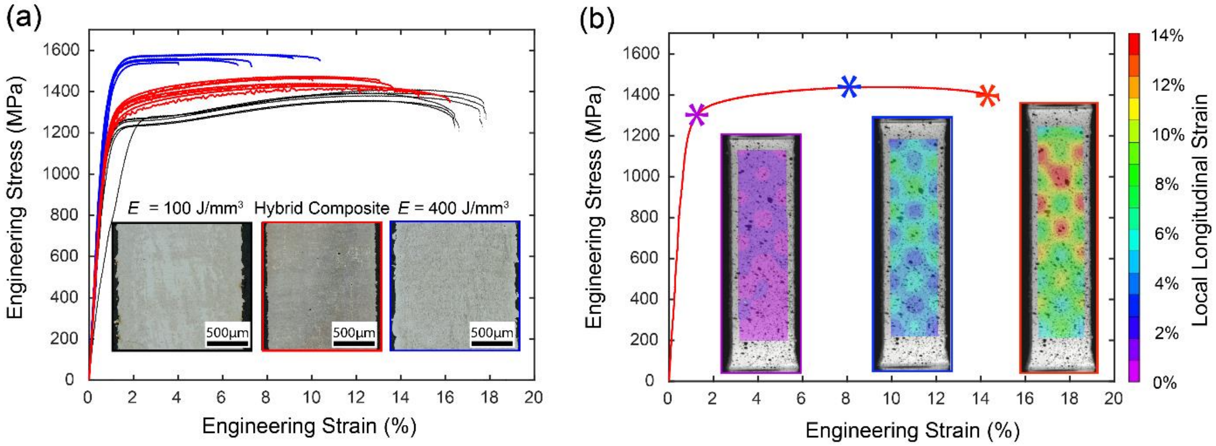

Figure 2.7. (a) Engineering stress-strain curves from tension tests on dog bone specimens printed with differing processing strategies: (i) uniformly low energy density of 100 J/mm^3 (black); (ii) uniformly high energy density of 400 J/mm^3 (blue), and (iii) a 'brick-and-mortar'-inspired architecture, embedding prismatic domains (bricks) printed at 400 J/mm^3 in a matrix (mortar) printed at 100 J/mm^3 (red). (b) Stress-strain curve with DIC strain maps for a 'brick-and-mortar'-inspired sample, clearly showing localized plastic deformation in the softer regions printed at E=100 J/mm^3. (See Figure S2.1 for geometric details).

Table 2.2. Mechanical properties of dog bone specimens printed at E=100 J/mm^3, hybrid 'brick-and-mortar' strategy, and E=400 J/mm^3. (See Figure S2.1 for geometric details).

	E=100 J/mm^3	**Hybrid Sample**	**E=400 J/mm^3**
Yield Strength (MPa)	1151 ± 17	1213 ± 41	1394 ± 25
Ultimate Tensile Strength (MPa)	1378 ± 22	1444 ± 24	1561 ± 16
Elongation to Failure (%)	18.3 ± 0.3	12.7 ± 3.5	7.2 ± 2.7

2.4. Chapter 2 Summary and Conclusions

In summary, we demonstrated local microstructural control in a precipitation hardened stainless steel printed via LPBF. When printed at high energy density (400 J/mm^3), the material develops a fully martensitic microstructure; by contrast, when printed at lower energy density (100 J/mm^3), a dual phase microstructure ensues, with martensitic laths interspersed with large ferritic grains, which largely populate the inter-hatch regions of the samples. The two microstructures exhibit significantly different mechanical properties, with ~20% differences in strength and ~150% differences in ductility. We demonstrate local microstructural control with a resolution of ~100 microns, in samples of different shapes and sizes. While the kinetic pathways that lead to different microstructural evolutions under different processing conditions are still under investigation, we experimentally confirm that ferritic grains consistently form exclusively in the inter-hatch region during subsequent thermal cycles, when the material is reheated within the temperature range of δ-ferrite stability. Computational studies are currently underway to develop a mechanistic understanding of these complex phase evolutions.

We expect that the findings presented in this study can be extended to other multi-phase alloy systems (e.g., Titanium alloys), significantly expanding the design space for LPBF-processed gradient structures.

3. Chapter 3. Controlling Phase Evolution of 17-4PH steel in Laser Powder Bed Fusion

3.1 Introduction

Laser powder bed fusion (LPBF) continues to be the most utilized metal additive manufacturing (AM) process, thanks to its many advantages over other metal AM techniques, specifically fine part resolution, high print density, improved mechanical properties, and operational simplicity [10]. While much of the effort in the early days of AM, and particularly LPBF, focused on fabricating homogeneous structures with a minimal amount of porosity and internal stresses, the inherent ability to locally tailor the structure and properties of a component is a powerful and unique feature of additive manufacturing (AM), which is inaccessible by any other manufacturing process [86,146–148]. This is enabled by the highly localized solidification process occurring at the dimensional scale of the melt pool (~100-500μm)[73,175–177]. With the ability to tailor multi-phase microstructures and their properties at specific locations, new pathways become available to optimize component performance [178–182]. For this opportunity to be fully utilized, a mechanistic understanding of the thermodynamics and kinetics of the local solidification processes contributing to phase evolution is needed.

Among the many alloys printed with LPBF, steels are the most utilized alloy family, offering an extensive range of alloy classes with different properties [55,168]. Within the high-value-added class of precipitation-hardening steels, 17-4PH emerges as one of the most employed due to its exceptional mechanical properties, corrosion resistance, and sustained performance at intermediate temperatures [54,75]. Wrought 17-4PH is a well-studied alloy, in which the material is often acquired or treated into the homogenized and quenched state (known as Condition A), resulting in a nearly fully martensitic microstructure, which is then precipitation hardened at different temperatures and times for different levels of strength, ductility, and corrosion resistance [56,183–185]. By contrast, the literature on LPBF processing of 17-4PH has reported a myriad of different microstructures and resulting properties, suggesting that this material is extremely sensitive to processing parameters, and hence would be an excellent candidate for local microstructural control [53,61–63,65,72,73,172,186,187]. Indeed, in our previous investigation, we observed that 17-4PH specimens printed under different processing parameters consistently produce different microstructures, ranging from 100% martensite to a dual-phase ferrite/martensite microstructure, and we used this effect to tailor properties and fabricate hybrid microstructures [188] locally. Figure 3.1 illustrates the degree of control. Simple parts printed with uniform processing parameters, chosen to yield relatively low volumetric energy density (VED = 100 J/mm^3), develop a two-phase ferrite/martensite microstructure (Figure 3.1a-b), whereas the same parts printed at uniform but higher volumetric energy density (VED = 400 J/mm^3) are fully martensitic (Figures 3.1c-d). Here VED is defined as the laser power divided by the product of hatching distance (i.e., distance between adjacent scan lines), layer thickness and laser scan speed. Hybrid microstructures can be easily and consistently produced by alternating the processing parameters during the build, e.g., by varying the laser scan speed while keeping the other parameters constant (Figures 3.1e-f). The mechanical properties are clearly affected by the microstructure, with the single-phase martensitic structure exhibiting high yield strength and low ductility, and the dual-phase ferrite/martensite structure displaying lower strength but much higher ductility (Figure 3.1g). Intriguingly, hybrid components can be designed that intentionally localize plastic deformation in specific regions (Figure 3.1h). Please, refer to [188] for details. This level of microstructural and mechanical property control was previously unreported in LPBF, and only possible through AM techniques that allow multiple material feedstocks (e.g., DED reviewed by Beese et. al. [146]).

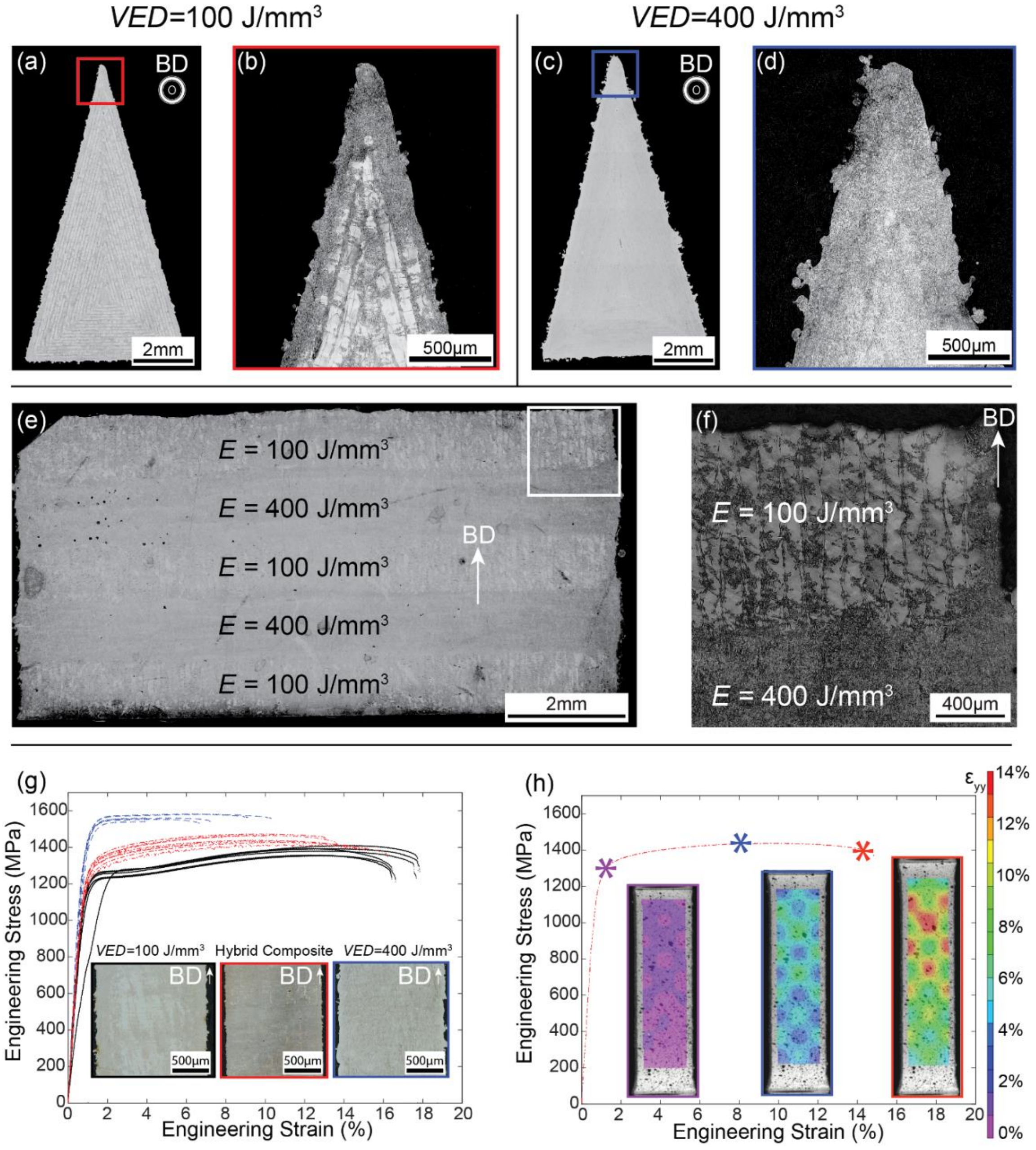

Figure 3.1. (a,b) Representative dual-phase microstructures of VED=100J/mm^3 specimens and (c,d) fully martensitic microstructure of VED=400J/mm^3 specimens. (e,f) The combination of multiple processing parameters into a single part composed of a hybrid microstructure. (g) The stress-strain curves of showing the bounds of mechanical behavior through microstructure. (h) Localized deformation controlled by purposefully input local microstructures. With permission from reference [188].

While this previous work clearly demonstrates consistent local control of the microstructure (particularly the ferrite/martensite phase composition) and associated properties, a mechanistic understanding of the pathways leading to the observed microstructures remains elusive. Here, we embark into an experimental and computational study to unveil these pathways. Two key results emerge from Figure 3.1[188]: (i) samples printed with high energy density (VED = 400 J/mm^3) develop a uniform, fully martensitic microstructure; by contrast, samples printed with lower volumetric energy density (VED = 100 J/mm^3) develop a more complex two-phase microstructure; (ii) in the case of low VED, the last scan lines are always martensitic (see borders in Fig. 3.1b), with large ferritic grains only appearing *in the hatch* between adjacent scan lines (Fig. 3.1b and 3.1f).

Microstructural evolution is a complex interplay of thermodynamic and kinetics effects, both of which may be responsible for the difference in microstructures observed in Fig. 3.1. Significant structural differences in the Fe-Cr-Ni system can be explained by understanding the thermodynamic stability of phases influenced by chemical composition, and the kinetic conditions promoting the formation of metastable phases (α' martensite). *Thermodynamic effects* are related to possible compositional changes induced by selective evaporation of low boiling point elements during laser melting. The Fe-Cr-Ni system is thermodynamically complex, and small variations in the chemical composition have significant effects on phase stabilities (and hence microstructural evolutions). Cr, Mo, and Nb are δ-ferrite-stabilizing elements, whereas Ni, Cu, C, and N are austenite-stabilizing elements. These effects have been captured in Schaeffler diagrams [189–191], which depict phase stability as a function of two compositional parameters, the Chromium equivalent, Cr_{eq}, and the Nickel equivalent, Ni_{eq}, which empirically capture the effects of alloying elements on phase stability [69,191–193]. While these diagrams were originally derived to explain microstructural evolution in welds, they can help explain phenomena observed on LPBF, with the important caveat on enormous kinetics differences between welding and LPBF. Incidentally, this thermodynamical competition between body centered cubic (BCC) ferrite and face centered cubic (FCC) austenite stability has been used as a framework for other alloy systems, including Fe-Mn-Si [162,194,195] and Nitinol [157,164,196] shape memory alloys, Ti-6Al-4V dual phase alpha-beta alloys [166,197], and Fe-9Cr reduced-activation-ferrite/martensite (RAFM) [198–201] steels. *Kinetic effects* are related to local thermal rates during laser melting and solidification, as well as subsequent thermal cycles associated with the melting and solidification of adjacent scan lines. Martensite forms upon rapid cooling of austenitic microstructures from the austenizing temperature. A critical cooling rate (CCR) can be defined as the minimum rate necessary to form a completely martensitic microstructure. The CCR is ~10^1-10^2 ^{o}C/s for most steels, depending on their composition [167,194,202,203]; these rates are easily achieved in water quenching, and far surpassed in AM, which is characterized by cooling rates of 10^4-10^7 ^{o}C/s [20,21]. While the cooling rate from melting is likely sufficiently high to transform all austenite to martensite upon solidification, the complex local thermal history associated with multiple heating/cooling cycles as the laser scans adjacent lines may induce unexpected phase transformation. This complex local thermal history is unique in comparison to conventional processes such as casting and quenching, in which only a singular cooling event is observed.

While VED is a convenient parameter expressing the local energy input into a volume of material during LPBF [134], the convolution of thermal input during powder melting (which is well captured by the linear energy density (LED), defined as laser powder divided by scan speed) and proximity of scan lines (i.e., hatching distance) makes it difficult to explicitly analyze the effects of thermodynamic and kinetic effects. To deconvolute these effects, we carefully examine the microstructural development of samples produced with different combinations of LED and VED. To eliminate, to the extent possible, the effects of sample geometry and the ensuing complexities in thermal history, while retaining the ability to investigate in-track and in-hatch regions of the builds, we produce simple thin-wall samples, vertically printed from the base plate, with thicknesses deriving from 2 (dual-wall) or 4 (quad-wall) adjacent scan lines (with the actual sample thickness affected by number of lines, LED and hatch distance). We analyze global (sample scale) and local (melt pool scale) chemical compositions, and relate them to phase stability, using both thermodynamic equilibrium and kinetic models, the latter informed by Finite Elements simulations of thermal histories [169,204,205]. Finally, we propose a diffusion model to explain the observed formation of large ferritic grains in the hatches between adjacent melt pools.

3.2 Methods

3.2.1 Samples Preparation

Experiments are conducted where the volumetric (VED) and linear (LED) energy densities are varied to yield different combinations of remelting and reheated regions. Volumetric and linear energy density are combinations of printing parameters that are used to express the total energy per unit of volume, and length, respectively. Here VED is defined as $\mathrm{VED} = \frac{P}{v \cdot h \cdot t}$, where P is the laser power, v is the laser scan speed, h is the hatch spacing between adjacent scans, and t is the layer thickness between consecutive build layers. LED is defined as $\mathrm{LED} = P/v$. With this definition, LED is independent of hatch spacing, and only characterizes melting along a single scan line [134]. While these quantities could be defined via non-dimensional parameters that include thermophysical properties and allow comparisons across different alloys[206], here we are considering a single material and preferred referring to the classic dimensional definitions.

17-4PH stainless steel N_2-atomized powder is obtained from Carpenter Additive and used throughout this study. All samples were printed with a SLM Solutions 125 printer, with a 99.99% N_2 atmosphere in the build chamber. Dual-wall samples were printed, in which each layer is produced by scanning the laser in a straight line, hatching over, and scanning the second line in the opposite direction. Quad-wall samples were produced similarly, but with each layer produced by 4 parallel scan lines. Dual and Quad wall samples are 5mm in length, 5mm in height, and have thickness varying depending on hatch spacing. Processing parameters were kept constant within each sample. For all samples, the laser power and layer thickness were kept constant at 200W and 30μm, respectively. Two scanning speeds of 167mm/s and 667mm/s were used, resulting in two different LEDs (LED = 1.2 J/mm and 0.3 J/mm respectively). The hatching distance (h) is varied from 80μm to 600μm for the higher LED samples, and from 20μm to 150μm for the lower LED samples, resulting in a range of VED of 67-500 J/mm^3 for both sets of LED. All other printing parameters were kept constant throughout the prints. The 'borders inside-out' scan strategy is chosen, in which concentric borders are printed from the inside to the outside. While this strategy had no effect for the dual-wall samples, the implication for quad wall samples is that the inside scans are reheated/remelted twice (once on each side/border). Sample characterization and analysis is conducted on the as-printed condition of the samples throughout the paper.

3.2.2 Microstructural Characterization

Samples are ground from 200 grit down to 600 grit and then polished via standard metallurgical techniques to 0.05μm using alumina. Samples are etched using Waterless Kalling's Reagent, aka Kalling's No.2, submerged face up and swirled for 60s. Microstructural analysis is predominantly performed using an Olympus DSX10-UZH Digital Optical Microscope. Higher magnification microscopy is conducted using a TESCAN GAIA-3 Scanning Electron Microscope

(SEM) with an Electron-Backscatter-Diffraction (EBSD) Oxford NordlysMax3 detector, to acquire phase maps to distinguish the martensite and ferrite phases. EBSD is used instead of XRD to identify phases, since multiple Kikuchi bands allow better differentiation compared to X-Ray Diffraction (XRD) shown in Figure S3.1 and S3.2 in which the detectable peaks are not distinguishable between BCC-ferrite and BCT-martensite. EBSD still has issue indexing the BCT martensite since 17-4PH is a low carbon steel, thus the tetragonality is minor and difficult to detect. Additionally, the martensitic grains are on the order of 500nm-1μm in size. With an EBSD spot size >200μm, indexing individual martensitic lathes is often unreliable and results in a perceived small ferrite grain. While some small untransformed residual ferrite is surely possible, the martensitic regions of our VED = 400 J/mm^3 samples are unlikely to be the ~25% indexed as ferrite, as that due to the difficulty in distinguishing between the two crystal structures.

3.2.3 Chemistry and Phase Measurements

Bulk chemistry is measured using a SPECTRO SPECTROLAB-S Spark Optical-Emission-Spectrometer (OES), in which the material is vaporized, and the radiation emitted is passed through to the OES and compared to a database of Fe-Ni-Cr calibration curves (*Fe-30* Spectro database). Spark-OES is a bulk measurement, vaporizing >100μm of material from the surface. As Spark-OES is highly sensitive to sample preparation, samples are tested in the as-printed condition immediately after printing. Spark-OES is also used to measure light elements such as C and N, which play a significant role in promoting the stability of FCC and BCC phases. To measure bulk sample chemistry via Spark-OES (see Materials and Methods), we fabricate prismatic samples (30mm x 30mm x 2mm) using the same combinations of LED and VED that is employed for the dual-wall samples (Figure 3.2). These samples were larger than dual-wall samples in order to meet the requirements for Spark-OES chemistry testing. X-Ray Fluorescence

(XRF) is also conducted using a Horiba XGT-9000 to precisely measure the local chemistry and capture elemental segregation. XRF points are measured using 50kV accelerating voltage, 1000μA current, and a scan time of 120s. XRF enables sample mapping at a spatial resolution of ~30μm, however light elements cannot be measured.

Differential Scanning Calorimetry (DSC) is conducted using a Netzch STA 449 F3 Jupiter. DSC is used to measure latent heats and capture phase transformations. DSC samples are heated from room temperature to 1500°C at a rate of 10 °C/min, held for 15 minutes, and then cooled back down at slow cooling rates of 5, 20, and 50 °C/min.

3.2.4 Thermodynamics, Kinetics and Thermo-Mechanical Simulations

ThermoCalc 2023b software is used to conduct thermodynamic equilibrium calculations using the TCFE8 equilibrium database. Only BCC-ferrite and FCC-austenite are equilibrium phases, thus meta-stable martensite is not considered in these diagrams. However, the full transformation of austenite into martensite due to extreme LPBF cooling rates is discussed in Appendix 1. Diffusion and Scheil solidification calculations are conducted using both the TCFE8 equilibrium and MOBFE8 mobility databases. Scheil solidification calculations account for back diffusion into the primary phase, as opposed to no diffusion in the solid when using conventional Scheil solidification calculations. Additionally, the δ-ferrite to γ-austenite transformation is accounted for. For the details of the Abaqus Finite Element Method thermal history simulations, see Appendix 1.

3.3. Results & Discussion

3.3.1 Microstructural Observations Across the Processing Regime

Optical images of dual-wall samples printed over a range of VED and LED, and etched to reveal microstructural features, are presented in Figure 3.2. All images are parallel to the build platform. While Figure 3.2 uses optical microscopy and etching to distinguish between ferrite (bright) and martensite (dark), these phases were also confirmed by electron-backscatter-diffraction (EBSD) (Figure S3.1).

In agreement with previous results obtained on larger specimens (Figure 3.1)[188], only the samples printed with $\mathrm{VED} \leq 100\,\mathrm{J/mm^2}$ produced a dual phase microstructure, with large columnar ferrite grains shown in Figure 3.2h, and smaller ferrite grains also observed in Figure 3.2g. Interestingly, though, this dual phase microstructure is only present at low linear energy density (LED = 0.3 J/mm). By contrast, all samples printed with $\mathrm{VED} > 100\,\mathrm{J/mm^2}$ or LED = 1.2 J/mm consistently show a uniform martensitic microstructure. Unsurprisingly, samples with LED = 1.2 J/mm and $\mathrm{VED} < 200\,\mathrm{J/mm^2}$, and samples with LED = 0.3 J/mm and $\mathrm{VED} < 100\,\mathrm{J/mm^2}$ also display a considerable amount of lack-of-fusion porosity. The implication of these findings is that VED alone is not a sufficient parameter to predict microstructural evolution, and non-trivial interplays of melt pool energy input and hatching spacing (represented by different combinations of VED and LED) are responsible for the distribution of phases in the as-printed microstructures.

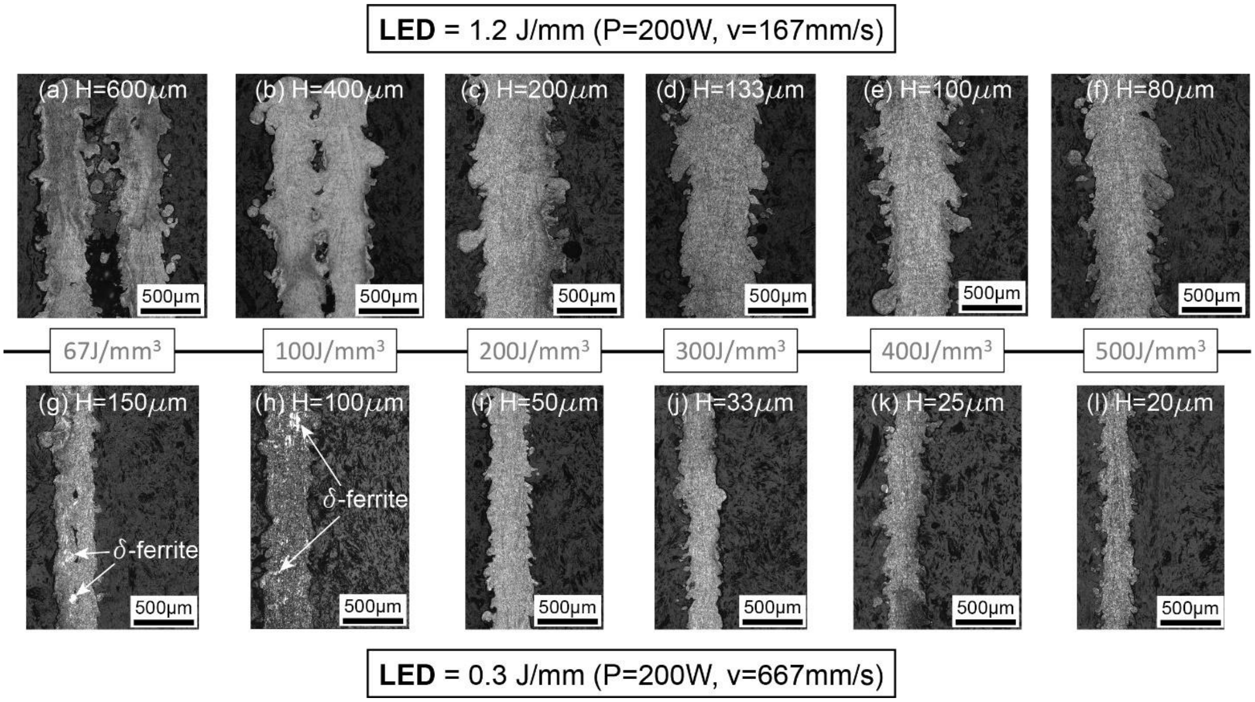

Figure 3.2. Effect of hatch spacing, and thus VED on dual walls with (a-f) LED = 1.2 J/mm resulting in no columnar ferrite under any printing condition. (g-l) LED = 0.3 J/mm resulting in columnar ferrite forming under hatch spacings of (g) 100μm and (h) 150μm.

From Figure 3.2, approximate melt pool sizes of 160μm and 320μm can be extracted, for LED = 0.3 J/mm and 1.2 J/mm, respectively. In comparison, the laser spot diameter is approximately 80μm. Thus, when the hatch spacing is much smaller than the melt pool size, the already solidified first melt pool is essentially being rescanned and fully remelted upon scanning of the adjacent line. This effectively increases (up to nearly doubling) the LED for a given melt pool. The implication of this phenomenon on phase evolution is discussed in detail in section 3.3.

3.3.2 Thermodynamic Phase Stability from Global and Local Chemistry

As discussed in the introduction, the differences in microstructural evolution as a function of processing parameters may be attributable to thermodynamics (i.e., differences in sample chemistry due to selective evaporation of low-boiling point elements during laser fusion) or kinetics (i.e., differences in cooling rates and thermal histories) - and possibly the interplay of both.

To deconvolute these effects, we utilize Differential Scanning Calorimetry (DSC). DSC uses very slow cooling rates (<1^{o}C/s, compared to 10^4-10^7^{o}C/s for LPBF) to identify near-equilibrium phase transformations. Samples printed with fully martensitic microstructures (LED = 1.2 J/mm and VED = 400 J/mm^3, Figure 3.3c) and dual phase ferritic/martensitic microstructures (LED = 0.3 J/mm and VED = 100 J/mm^3, Figure 3.3f) are inserted in the DSC furnace, melted at 1500^{o}C and subsequently cooled down at different cooling rates (5-50 C/min). Heat flow-temperature profiles are displayed in Fig. 3.3. A key result emerges: samples printed with high VED and LED show a single liquid – austenite transformation peak at ~1400C with no evidence of additional solid-solid phase transitions (Figure 3.3a-b), consistent with the fully martensitic microstructure observed after LBPF (Figure 3.3c); by contrast, samples printed with low VED and LED show an additional δ-ferrite – austenite transformation peak at ~1220C (Figure 3.3d-e), clearly confirming a thermodynamic stability region for the δ-ferrite phase. Consistent with the fully martensitic microstructure observed after LBPF; this could help explain the presence of δ-ferrite in the final LPBF microstructure (Figure 3.3f).

DSC experiments are conducted with cooling rates down to 5^{o}C/min (0.1^{o}C/s), essentially eliminating the effect of cooling rate on solidification, and indicating that the δ-ferrite phase is only thermodynamically stable in our LED = 0.3 J/mm and VED = 100 J/mm^3 sample. Since these fully melted samples have their as-printed microstructures erased and are cooled slowly, this difference in observed phase stability is purely a chemistry effect. Thus, it is necessary to thoroughly analyze the effects of different processing parameters on chemistry.

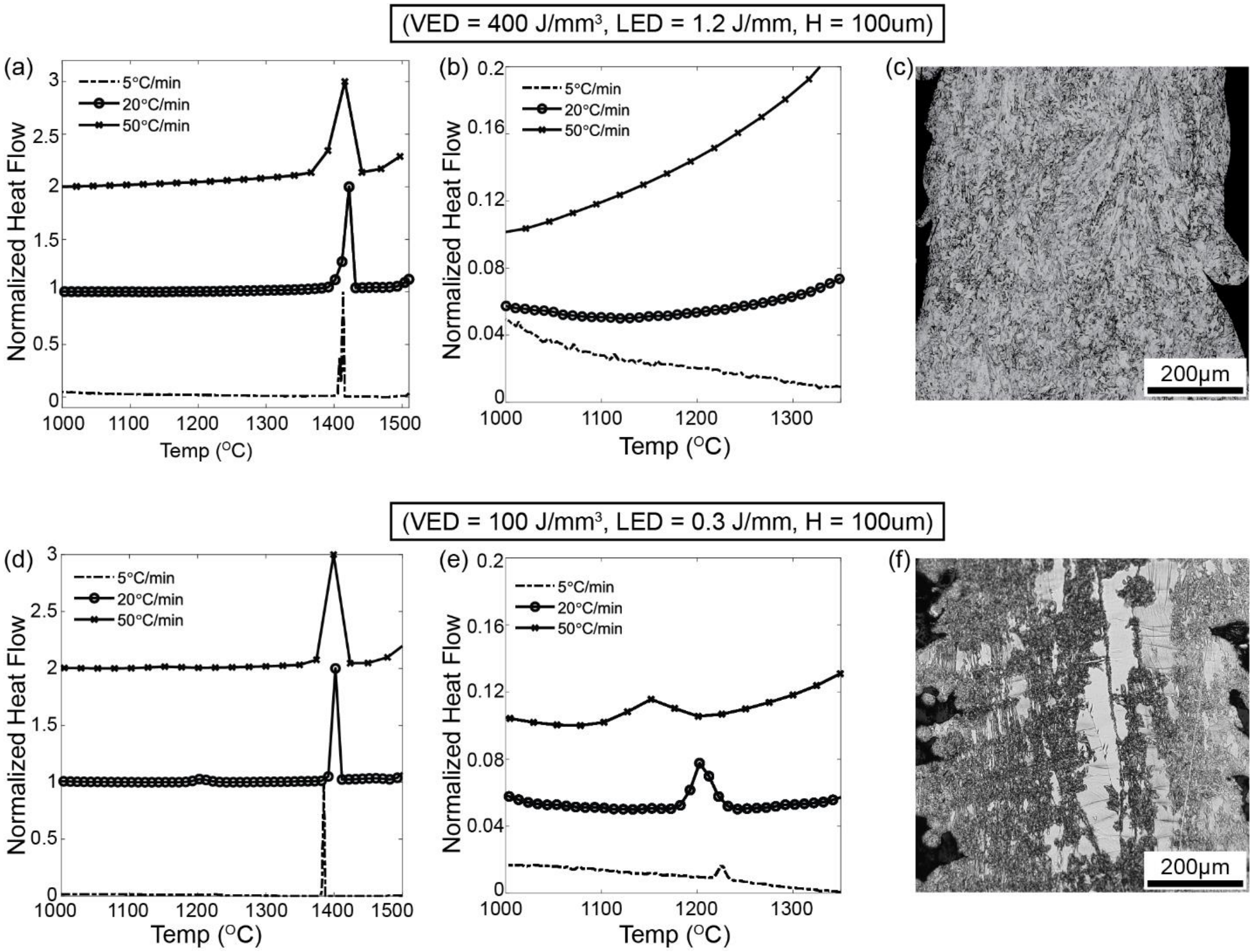

Figure 3.3. (a,b) DSC of LED = 1.2 J/mm & VED = 400 J/mm^3 and (c) the corresponding fully martensitic microstructure. (d) DSC of LED = 0.3 J/mm & VED = 100 J/mm^3 and (e) magnification near 1150°C where the exothermic δ-ferrite to γ-austenite phase transformation is observed. (f) The corresponding dual phase microstructure.

Differences in chemistry in the bulk samples are attributed to different heat inputs during laser melting (and possible remelting, for closely spaced scan lines), which is related to both LED and VED. Although 17-4PH is not as susceptible to large compositional changes upon LPBF as other alloys with very high-volatility components, such as Mg, Zn, and Li [118,207], the Fe-Cr-Ni system is extremely sensitive to very small changes in chemistry.

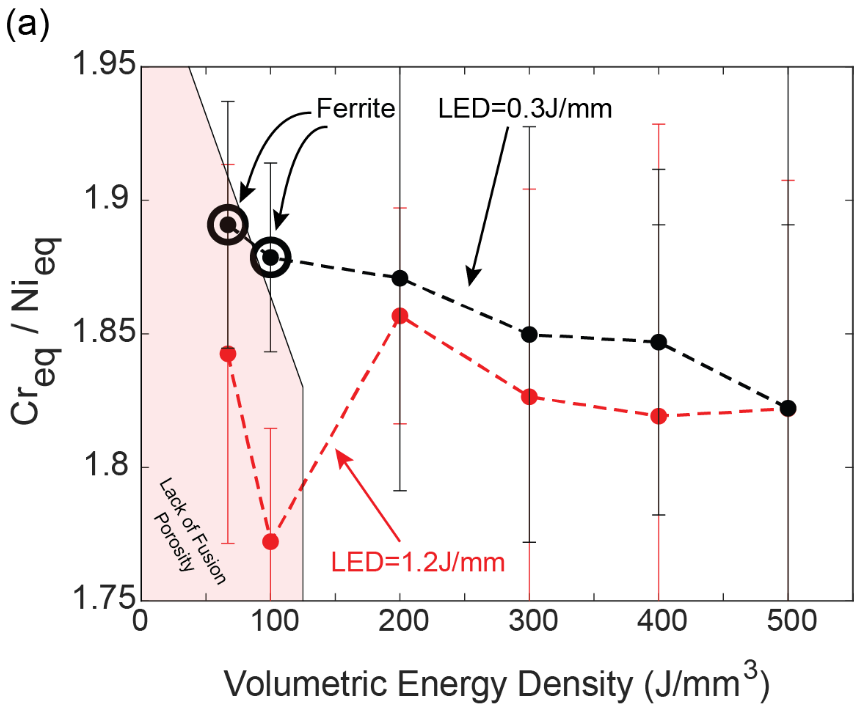

Figure 3.4. Post Print Cr_{eq}/Ni_{eq} ratio.

The measured elemental compositions can be combined into empirical Cr equivalent (Cr_{eq}) and Ni equivalent (Ni_{eq}) parameters, with the ratio of these representing the tendency for δ-ferrite phase stability [192]. The most recent versions of these empirical parameters are provided by the 1992 Welding Research Council [192] as:

$$Cr_{eq} = Cr + Mo + 0.7Nb \tag{1}$$

$$Ni_{eq} = Ni + 35C + 20N + 0.25Cu \tag{2}$$

The results are presented in Figure 3.4. Notice that the Cr_{eq}/Ni_{eq} ratio is lower for all samples processed with LED = 1.2 J/mm than for samples processed with LED = 0.3 J/mm. Consistent with the higher melt pool temperature resulting from higher LED, and the relatively high volatility of Chromium relative to Nickel. Also notice that the samples with the two highest Cr_{eq}/Ni_{eq} ratios are those where columnar ferrite is observed. For reference, consider that 15-5PH stainless steel, which has a composition designed to prevent any ferrite formation, has

Cr_{eq}/Ni_{eq}=1.85 [208]; hence, we can expect that any sample with Cr_{eq}/Ni_{eq} <1.85 should have a fully martensitic microstructure, in agreement with our experimental measurements.

The volume fraction of the individual elements contributing to Cr_{eq} and Ni_{eq} are shown in Figure S3.3. Notice that nitrogen and carbon contents are noticeably higher in the LED = 1.2 J/mm samples than in the LED = 0.3 J/mm samples. The results for nitrogen can be attributed to different absorption while printing in a nitrogen atmosphere: the higher LED = 1.2 J/mm samples are processed with a much lower scan speed (167mm/s, compared to 667mm/s in the LED = 0.3 J/mm samples), providing more time for the liquid melt pool to absorb nitrogen from the build chamber. This increase in absorption time from a much slower scan speed, must also allow for more absorption of the residual carbon in the printing chamber.

While Figure 3.4 clearly shows that the samples that experimentally exhibit large ferritic grains in the microstructure have the highest Cr_{eq}/Ni_{eq} ratios, CALPHAD equilibrium phase diagrams calculations performed with ThermoCalc’s TCFE13 database suggest that the measured values of Cr_{eq}/Ni_{eq} = 1.85-1.9 are still too low to stabilize the δ-ferrite phase, and predict that even the samples with highest Cr_{eq}/Ni_{eq} ratios should display an equilibrium phase composition of 100% austenite.

To better understand the origin of the observed ferritic grains, as well as explain why their presence is largely localized to the in-hatch regions between adjacent scan lines, we resort to local chemistry measurements by X-Ray Fluorescence (XRF); this technique is chosen over more conventional SEM-EDS measurements thanks to its high chemical detection resolution of 0.01%.

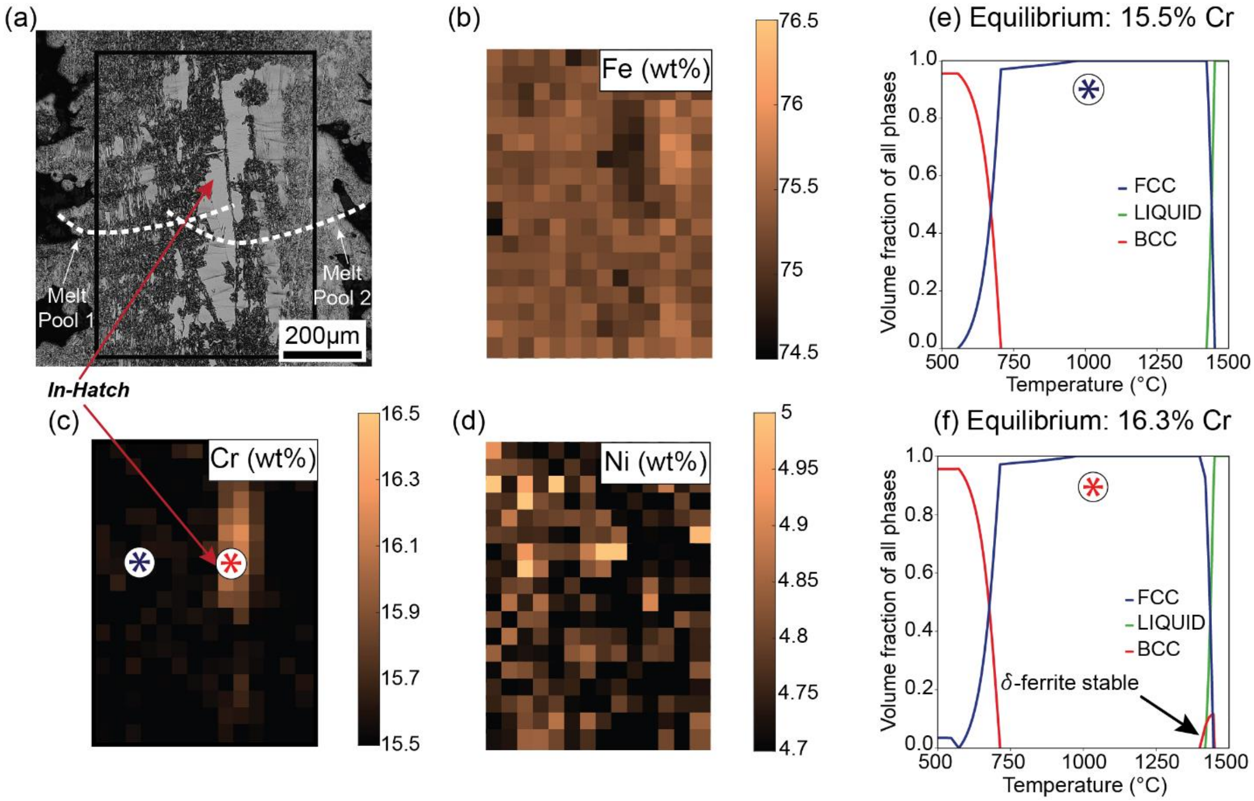

Figure 3.5. (a) Optical micrograph of LED = 0.3 J/mm & VED = 100 J/mm^3 sample with the boxed region to be XRF'd. XRF measurements of (b) Fe, (c) Cr segregation, and (d) Ni depletion in the ferrite region. Thermodynamic equilibrium step diagrams calculated for the (e) *In-Hatch* Cr enriched (16.3 wt%) regions and the (f) *In-Track* Cr depleted (15.5 wt%) regions. Notice δ-ferrite is only thermodynamically stable in the Cr enriched region.

Figure 3.5 displays XRF maps of a multi-phase region in the sample (Figure 3.5a) printed with LED = 0.3 J/mm and VED = 100 J/mm^3. Significant Cr segregation to the in-hatch region (in clear correspondence with the location of the large ferritic grains) is clearly observed (Figure 3.5c), accompanied by Fe (Figure 3.5b) and Ni (Figure 3.5d) depletion. Interestingly, Cr concentrations as high as 16.3% are measured in those regions, compared with baseline values of 15.5% in the largely martensitic domains. These local differences (0.8%) are much more pronounced than the largest difference in average Cr concentration among all printed samples, which is 0.15% (Figure S3.3). CALPHAD equilibrium phase diagrams calculations, again performed using ThermoCalc's TCFE13 database, clearly show that these local differences can explain the observed microstructural differences. While the *In-track* regions are sufficiently Cr-depleted to completely eliminate δ-ferrite stability (Figure 3.5e), the Cr content in the *In-hatch* region is Cr-enriched enough for δ-ferrite to be thermodynamically stable (Figure 3.5f). Similar XRF analyses were conducted on selected fully martensitic samples printed with higher VED and LED, and confirmed low enough Cr content to fully destabilize the δ-ferrite phase across the samples.

These local chemistry measurements, combined with CALPHAD simulations, help explain the microstructural differences observed among the samples printed in this study. When the feedstock powder is locally melted by the scanning laser beam, primarily Cr evaporates, depressing Cr_{eq}. In all samples printed with sufficiently high VED and LED, Cr_{eq} drops below the level required to stabilize the δ-ferrite phase. As a result, only austenite forms upon solidification. By contrast, in the *In-hatch* regions, sufficient amount of Cr remains to allow formation of some δ-ferrite phase. Upon solidification, both δ-ferrite and austenite form.

While the explanation above convincingly relates local chemistry with phase stability, the solid state transformation occurring during rapid cooling, as well as the mechanisms leading to Cr segregation into the *In-hatch* regions for the samples printed at low VED and LED remain unexplained. Kinetic considerations, explored in the next section, are necessary to shed light on these phenomena.

3.3.3 The Effect of Kinetics: Cooling Rates, Melt Pool Diffusion, and Segregation

Differences in local chemistry and thus thermodynamic stability explain why we observe different phases in our *In-Hatch* and *In-Track* regions of the LED = 0.3 J/mm and VED = 100 J/mm^3 sample. To further explain how this high temperature δ-ferrite is retained at room temperature, as well as how austenite transforms into martensite, it is necessary to understand the kinetics regarding thermal history of each sample during processing.

The application of kinetics models requires at least approximate knowledge of the thermal history (and in particular, the cooling rates) experienced by the samples during melting and solidification, as a function of the processing parameters. Reasonable estimates can be extracted by Finite Elements Analyses (FEA), described in detail in Appendix 1. FEA predictions of the thermal histories experienced at two locations, contained in the *In-hatch* and *In-track* regions, of two samples printed with different processing conditions (LED = 0.3 J/mm, VED = 100 J/mm^3, and LED = 1.2 J/mm, VED = 400 J/mm^3) are depicted in Figure 3.6. Printing of two lines and four layers is simulated for each sample, resulting in 8 temperature cycles.

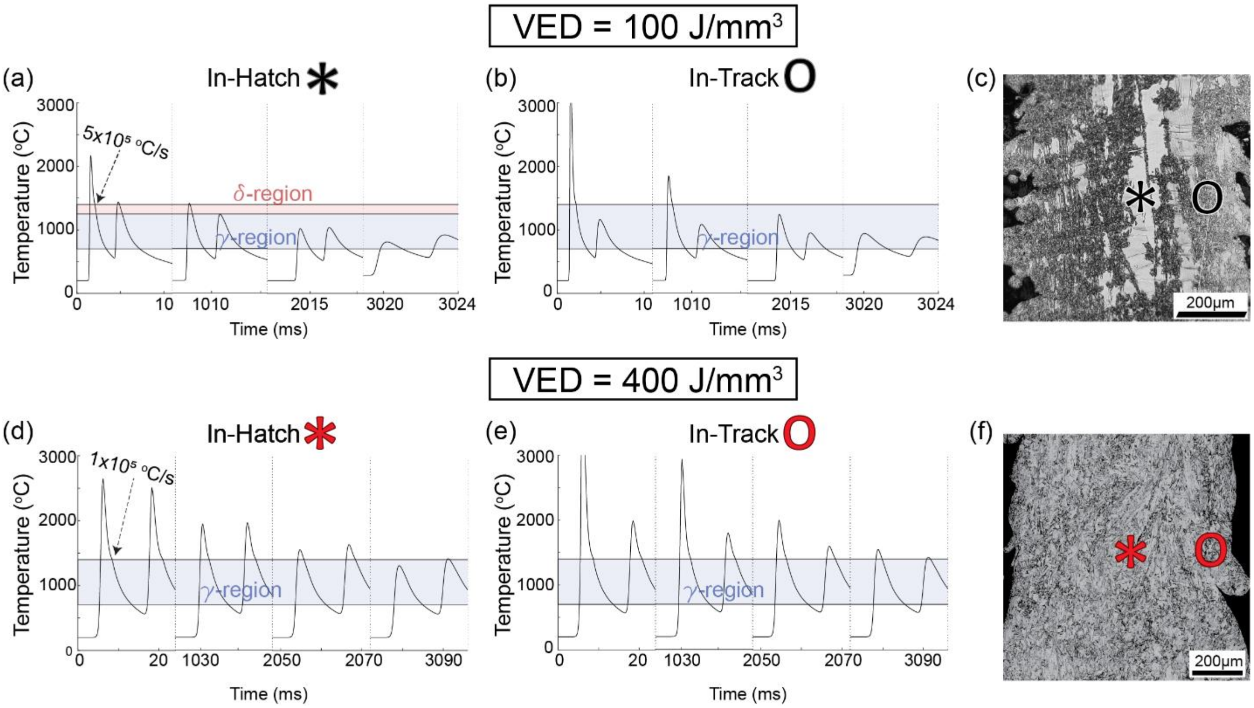

Figure 3.6. Simulated thermal history with overlayed experimentally measured phase stability for the LED = 0.3 J/mm & VED = 100 J/mm^3 (a) In-Hatch region and (b) In-Track region. Simulated thermal history for LED = 1.2 J/mm & VED = 400 J/mm^3 (d) In-Hath region and (e) In-Track region. The corresponding microstructures are shown for (c) VED = 100 J/mm^3 and (f) VED = 400 J/mm^3.

The experimentally measured temperature ranges for stability of the austenite and ferrite phases are included for reference. While the thermophysical model does not contain information on the latent heat of vaporization, resulting in overprediction of the peak temperature upon melting, the rest of the thermal history is expected to be accurate. Cooling rates from the melt of ~1x10^5 ^{o}C/s and ~5 x 10^5 ^{o}C/s for the VED = 400 J/mm^3 and VED = 100 J/mm^3 samples, respectively, are extracted from the simulations. In all cases, these cooling rates vastly exceed the critical cooling rates for martensitic transformation (10^1 – 10^3 for most martensitic steels [200], clearly explaining why no austenite is observed in the room temperature microstructures. These cooling rates are also fast enough to skip the nose in the δ-ferrite – austenite CCT diagram [200] suggesting that the δ-ferrite phase could remain in metastable state at room temperature, in agreement with experimental observations.

To further confirm this hypothesis, Scheil solidification calculations for different regions of the VED = 100 J/mm^3 sample are conducted within the ThermoCalc simulation package, using the cooling rates extracted from the FEA simulations and the experimentally measured chemical compositions. The model is able to capture back diffusion into the primary phase, as well as the δ-ferrite to austenite phase transformation during solidification. Results for the *In-hatch* and *In-track* regions are reported in Figure 3.7a-b and Figure 3.7c-d, respectively. The evolution of the mass fractions of austenite and δ-ferrite with temperature is shown in Figures 3.7a,c and 3.7b,d, respectively. In the Cr enriched *In-hatch* region, δ-ferrite is the primary solidified phase (Figure 3.7b), which hits a peak mass fraction of 20%, before only partially transforming into austenite. The growth of the austenitic phase continues (Figure 3.7a) until the material is fully solidified, with a final composition of 85% austenite and 15% δ-ferrite. This unequivocally confirms that the δ-ferrite phase is kinetically stabilized at room temperature in the *In-hatch* region of the VED = 100 J/mm^3 sample. By contrast, only austenite forms in the *In-track* region of the same sample, which fully transforms to martensite upon cooling to room temperature.

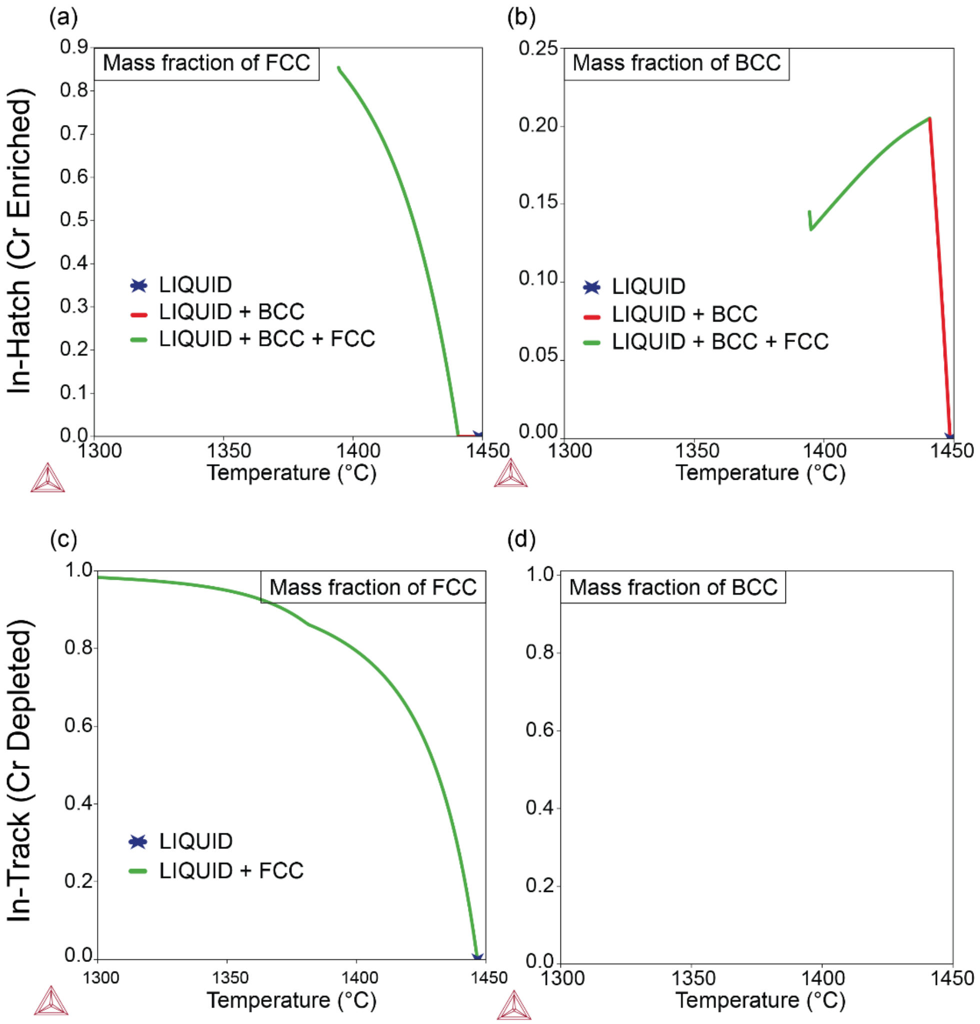

Figure 3.7. Scheil solidification calculations accounting for both back diffusion into the primary phase, and the δ to γ transformation for our LED = 0.3 J/mm & VED = 100 J/mm^3 sample. The mass fraction during solidification of (a) FCC and (b) BCC for the Cr enriched region. The mass fraction during solidification of (a) FCC and (b) BCC for the Cr depleted region.

Another mechanism that is not accounted for in Figures 3.6 and 3.7 is the increased stability of Cr in the BCC (δ) compared to the FCC (γ). Figure S3.4 shows mass percent Cr stable in BCC vs FCC under different conditions. The important takeaway is that regardless of solidification model, the BCC has a higher Cr stability compared to in the FCC by at minimum 2% Cr in equilibrium. Therefore, in addition to our thermodynamic equilibrium and solidification models, Cr has a natural driving force to selectively enrich into the BCC and grow epitaxially once nucleated by nature of being more stable in that crystal structure.

To elucidate possible mechanisms resulting in the segregation of Cr in the *-Hatch* region of samples printed with low VED and LED, diffusion calculations are performed using ThermoCalc's DICTRA software with the MOBFE8 steel database. A simple one-dimensional model is analyzed, capturing the time evolution of the Cr concentration profile during melting of the second track (on the right), separated from the previously solidified track (on the left) by an *In-hatch* region. The concentration of the right track is justified by the virgin powder chemistry, shown in Table S1. The domain spans the distance between the centerlines of two adjacent scan lines. The boundary condition at the left end of the domain (corresponding to the center of the previously solidified track) is set to the experimentally measured Cr content in the *In-track* region (simulating the Cr content in the previously solidified track). In contrast, a Cr gas activity boundary condition is applied to the right end of the domain, simulating evaporation of Cr through the surface of the melt pool for the second track. The concentration of Cr in the virgin powder is used as initial conditions for the melt pool (Table S1). Results are shown in Figure 3.8. Cr diffusion from the enriched region (representing virgin powder) towards the depleted region (representing the first solidified melt pool) are shown at different times during solidification (with time scales extracted from the FEA simulations in Figure 3.6). Note that at a time of ~40ms, the Cr concentration profile predicted by this simplified 1D diffusion/evaporation model qualitatively matches the experimental Cr concentration line profile extracted from the XRF measurements (Figure 3.8a). We emphasize that this model significantly oversimplifies the physics of melt pool solidification and Cr evaporation and diffusion, by reducing a complex three-dimensional phenomenon to a 1D problem, lumping all evaporation through the surface of the melt pool to a point-wise boundary condition, and neglecting any convective phenomenon (e.g., Marangoni flows) within the melt pool. Consequently, its predictions should only be interpreted in a qualitative way. Nonetheless, the important result is that noticeable segregation of Cr may occur during solidification in the VED = 100 J/mm^3, LED = 0.3 J/mm sample, leaving the *In-Hatch* regions richer in Cr than the *In-track* regions, in agreement with experimental evidence. While the same model does not predict a flat concentration profile for the fully martensitic samples (e.g., the VED = 400 J/mm^3, LED = 1.2 J/mm sample), we emphasize that neglecting convective Marangoni flows is particularly inaccurate for the high LED samples, where the melt pool is expected to be much more turbulent [209,210]. Hence, we expect Marangoni flows to strongly homogenize the chemical composition of high LED samples, resulting in local compositions nearly equal to the average compositions measured by OES (Figure S3.3); these compositions result in Cr_{eq}/Ni_{eq} ratios that are consistent with a fully martensitic microstructure (Figure 3.4). Finally, to explain why no δ-ferrite is observed in samples printed at low LED (0.3 J/mm), but larger VED (>100 J/mm^3), we notice that the melt pool heavily overlap under these conditions (see Figure 3.2), resulting in repeated melting of the same volume of material, with an associated increase in Cr evaporation, which brings the Cr_{eq}/Ni_{eq} ratio to the limit below which δ-ferrite can be stable.

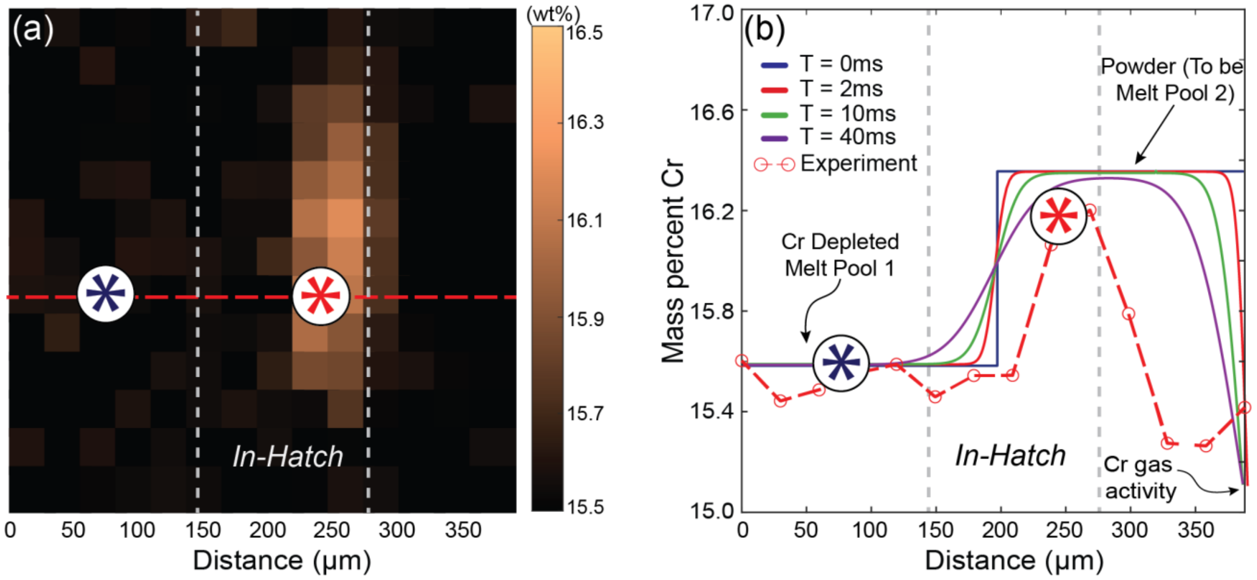

Figure 3.8. (a) XRF Cr segregation in the *In-Hatch* region. (b) CALPHAD liquid diffusion calculation with a 1% chromium concentration gradient across a 380um region. The diffusion kinetics are fast enough that under a few ms solidification time (as in LPBF), segregation of Cr across the melt pools can be induced.

3.4. Chapter 3 Summary and Conclusions

Multiple thin-wall samples were printed with 2 and 4 scan lines across the thickness via LPBF in 17-4PH stainless steel, covering a wide range of VED and LED. Microstructural characterization reveals that nearly all samples display a uniform, single-phase martensitic microstructure, with the exception of 2 samples printed with simultaneously low LED (0.3 J/mm) and low VED (<100 J/mm^3), which exhibit a more complex two-phase microstructure, with martensitic *In-track* regions separated by ferritic *In-hatch* regions. Average and local chemical analysis performed with Spark-OES and XRF, respectively, coupled with CALPHAD thermodynamic calculations, confirm that all high-energy samples have experienced sufficient evaporation of Cr to effectively suppress the thermodynamic stability of δ-ferrite; when combined with Finite Element simulations of thermal history, which predict cooling rates of the order of $1 \cdot 10^5$ °C/s (far exceeding the critical cooling rates for martensitic transformation), these results fully explain the fully martensitic microstructure observed in these samples. The situation is more complex for the low energy samples: for these samples, while the average chemical composition is still too low in Cr to predict δ-ferrite stability, *In-hatch* regions display significantly higher Cr content than *In-track* regions, for which CALPHAD simulations predict a window of δ-ferrite stability. Scheil solidification simulations confirm that δ-ferrite will remain in metastable form at room temperature, in agreement with microstructural observations (with the austenitic regions transforming to martensite upon cooling, as in the high energy samples). We invoke a simple 1D diffusion model to provide an explanation for the segregation on Cr in the *In-hatch* regions, and attribute the absence of segregation in the high-energy samples to the presence of strong

Marangoni flows associated with high LED. Collectively, these results provide a mechanistic understanding of microstructural evolution of 17-4PH steel processed in LPBF, and explain the origin of complex spatially heterogeneous two-phase microstructures that were observed in previous studies. The relationship between LED and VED can also be expressed in terms of LED and hatch spacing; the implication of hatch spacing on microstructural evolution is schematically illustrated in Figure 3.9a and 3.9b, for LED = 1.2 J/mm and LED = 0.3 J/mm, respectively.

The results can be used for intentional local design of specific microstructures in 17-4 PH steel, as summarized with the decision tree in Figure 3.9c.

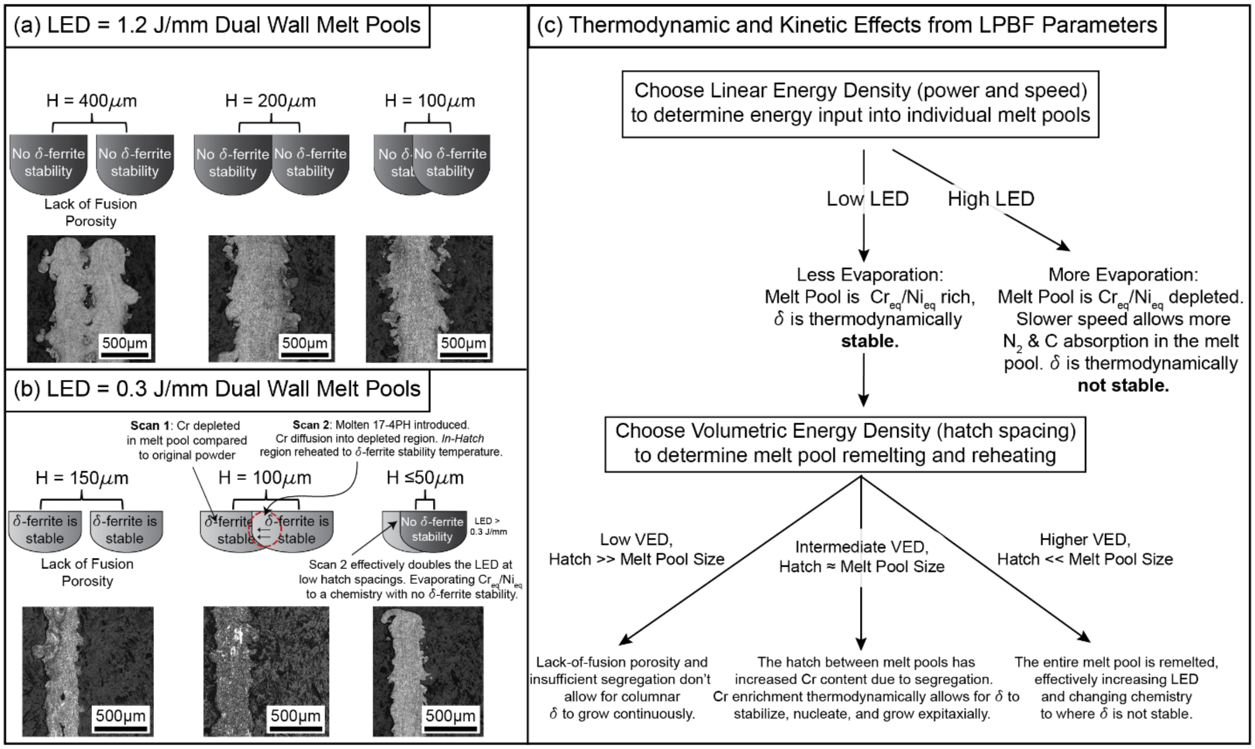

Figure 3.9. (a) Dual wall melt pools of LED = 1.2 J/mm with various hatch spacings. (b) Dual wall melt pools of LED = 0.3 J/mm with various hatch spacings. (c) Thermodynamic and Kinetic effects from LPBF process parameters.

REFERENCES

[1] A. Mcwilliams, C. Spivey, **2017**.

[2] D. Sher, “GE Aviation ships 100,000th 3D printed nozzle tip,” can be found under https://www.3dprintingmedia.network/ge-aviation-ships-100000th-3d-printed-nozzle-tip/, **2021**.

[3] P. V. Cobbinah, R. A. Nzeukou, O. T. Onawale, W. R. Matizamhuka, *Metals (Basel)* **2021**, *11*, 1.

[4] S. Mirzababaei, S. Pasebani, *Journal of Manufacturing and Materials Processing* **2019**, *3*, 8.

[5] M. Galati, L. Iuliano, *Addit Manuf* **2018**, *19*, 1.

[6] L. P. Raut, R. V. Taiwade, *J Mater Eng Perform* **2021**, *30*, 4768.

[7] D. G. Ahn, *Directed Energy Deposition (DED) Process: State of the Art*, Korean Society For Precision Engineering, **2021**.

[8] G. Prashar, H. Vasudev, *J Clean Prod* **2021**, *310*, 127606.

[9] S. Dadbakhsh, R. Mertens, L. Hao, J. Van Humbeeck, J. P. Kruth, *Adv Eng Mater* **2019**, *21*, 1.

[10] A. Mcwilliams, *BCC Research studies* **2022**.

[11] C. Körner, *International Materials Reviews* **2016**, *61*, 361.

[12] S. R. Narasimharaju, W. Zeng, T. L. See, Z. Zhu, P. Scott, X. Jiang, S. Lou, *J Manuf Process* **2022**, *75*, 375.

[13] X. Liu, Y. Liu, Z. Zhou, Q. Zhan, *J Mater Sci Technol* **2022**, *124*, 41.

[14] J. H. Martin, B. D. Yahata, J. M. Hundley, J. A. Mayer, T. A. Schaedler, T. M. Pollock, *Nature* **2017**, *549*, 365.

[15] M. Shunmugavel, A. Polishetty, G. Littlefair, *Procedia Technology* **2015**, *20*, 231.

[16] D. Agius, K. I. Kourousis, C. Wallbrink, *Metals (Basel)* **2018**, *8*, DOI 10.3390/met8010075.

[17] Y. Zhao, Q. Guo, Z. Ma, L. Yu, *Materials Science and Engineering A* **2020**, *791*, 139735.

[18] B. Song, X. Zhao, S. Li, C. Han, Q. Wei, S. Wen, J. Liu, Y. Shi, *Frontiers of Mechanical Engineering* **2015**, *10*, 111.

[19] J. Bedmar, A. Riquelme, P. Rodrigo, B. Torres, J. Rams, *Materials* **2021**, *14*, DOI 10.3390/ma14216504.

[20] P. A. Hooper, *Addit Manuf* **2018**, *22*, 548.

[21] U. Scipioni Bertoli, G. Guss, S. Wu, M. J. Matthews, J. M. Schoenung, *Mater Des* **2017**, *135*, 385.

[22] P. Ponnusamy, R. A. R. Rashid, S. H. Masood, D. Ruan, S. Palanisamy, *Materials* **2020**, *13*, 1.

[23] L. Guo, H. Wang, H. Liu, Y. Huang, Q. Wei, C. L. A. Leung, Y. Wu, H. Wang, *Int J Mach Tools Manuf* **2023**, *184*, DOI 10.1016/j.ijmachtools.2022.103977.

[24] L. Xi, L. Feng, D. Gu, R. Wang, B. Sarac, K. G. Prashanth, J. Eckert, *Journal of Materials Research and Technology* **2022**, *19*, 4645.

[25] Y. Qi, H. Zhang, W. Zhang, Z. Hu, H. Zhu, *Mater Charact* **2023**, *195*, 112505.

[26] D. Li, Z. Zhang, S. Li, J. Yang, S. Zhang, X. Bian, Y. Zhang, L. Qi, O. A. Ojo, *Int J Fatigue* **2023**, *172*, 107636.

[27] N. T. Aboulkhair, M. Simonelli, L. Parry, I. Ashcroft, C. Tuck, R. Hague, *Prog Mater Sci* **2019**, *106*, 1.

[28] H. R. Kotadia, G. Gibbons, A. Das, P. D. Howes, *Addit Manuf* **2021**, *46*, DOI 10.1016/j.addma.2021.102155.

[29] P. Ponnusamy, R. A. R. Rashid, S. H. Masood, D. Ruan, S. Palanisamy, *Materials* **2020**, *13*, 1.

[30] S. Kou, *Acta Mater* **2015**, *88*, 366.

[31] N. Kaufmann, M. Imran, T. M. Wischeropp, C. Emmelmann, S. Siddique, F. Walther, *Phys Procedia* **2016**, *83*, 918.

[32] J. Zhang, J. Gao, B. Song, L. Zhang, C. Han, C. Cai, K. Zhou, Y. Shi, *Addit Manuf* **2021**, *38*, 101829.

[33] H. Zhang, H. Zhu, X. Nie, J. Yin, Z. Hu, X. Zeng, *Scr Mater* **2017**, *134*, 6.

[34] N. Li, T. Wang, L. Zhang, L. Zhang, *Mater Charact* **2023**, *195*, 112415.

[35] M. Sokoluk, J. I. E. Yuan, S. Pan, X. Li, *Metallurgical and Materials Transactions A* **2021**, DOI 10.1007/s11661-021-06302-9.

[36] W. Stopyra, K. Gruber, I. Smolina, T. Kurzynowski, B. Kuźnicka, *Addit Manuf* **2020**, *35*, DOI 10.1016/j.addma.2020.101270.

[37] L. Zhao, L. Song, J. G. Santos Macías, Y. Zhu, M. Huang, A. Simar, Z. Li, *Addit Manuf* **2022**, *56*, 102914.

[38] Z. Xiao, W. Yu, H. Fu, Y. Deng, Y. Wu, H. Zheng, *Virtual Phys Prototyp* **2023**, *18*, DOI 10.1080/17452759.2022.2125880.

[39] T. M. Pollock, A. J. Clarke, S. S. Babu, *Metall Mater Trans A Phys Metall Mater Sci* **2020**, *51*, 6000.

[40] P. A. Rometsch, Y. Zhu, X. Wu, A. Huang, *Mater Des* **2022**, *219*, 110779.

[41] T. Minasyan, I. Hussainova, *Materials* **2022**, *15*, DOI 10.3390/ma15072467.

[42] Y. Karabulut, R. Ünal, *J Mater Sci* **2022**, *57*, 19212.

[43] Y. Shi, K. Yang, S. K. Kairy, F. Palm, X. Wu, P. A. Rometsch, *Materials Science and Engineering A* **2018**, *732*, 41.

[44] B. Mehta, T. Mishurova, S. Evsevleev, H. Markötter, G. Bruno, E. Hryha, L. Nyborg, E. Virtanen, *Mater Des* **2023**, *226*, 111602.

[45] X. Liu, Y. Liu, Z. Zhou, W. Luo, Z. Zeng, *Materials Science and Engineering A* **2022**, *856*, 144010.

[46] J. Choe, K. T. Kim, J. H. Yu, J. M. Park, D. Y. Yang, S. ho Jung, S. Jo, H. Joo, M. Kang, S. Y. Ahn, S. G. Jeong, E. S. Kim, H. Lee, H. S. Kim, *Addit Manuf* **2023**, *62*, 103370.

[47] A. B. Spierings, D. Y. Ozherelkov, F. Kneubühler, S. A. Eremin, I. A. Pelevin, A. Y. Nalivaiko, E. A. Petrov, A. A. Gromov, K. Wegener, *J Alloys Compd* **2023**, *947*, 169421.

[48] Z. Zhang, J. Sun, J. Wu, J. Xia, B. Zhang, P. Zuo, B. Zhang, *Journal of Materials Research and Technology* **2023**, *23*, 4734.

[49] P. Chernyshova, T. Guraya, A. Martinez-Amesti, H. Andonegi, S. Singamneni, Z. W. Chen, *Adv Eng Mater* **2023**, *2300135*, 1.

[50] F. Li, Z. Li, C. Tang, L. Zhang, Q. Tan, C. Chen, M. X. Zhang, K. Zhou, *Materials Science and Engineering A* **2023**, *864*, 144591.

[51] X. Zhu, Z. Zhu, T. Liu, W. Liao, Y. Du, H. Wei, *J Mater Sci Technol* **2023**, *156*, 183.

[52] Y. J. Bhatt, S. P. Garg, *Metallurgical Transactions B* **1976**, *7*, 271.

[53] S. Vunnam, A. Saboo, C. Sudbrack, T. L. Starr, *Addit Manuf* **2019**, *30*, 100876.

[54] L. Zai, C. Zhang, Y. Wang, W. Guo, D. Wellmann, X. Tong, Y. Tian, *Metals (Basel)* **2020**, *10*, 1.

[55] P. Bajaj, A. Hariharan, A. Kini, P. Kürnsteiner, D. Raabe, E. A. Jägle, *Materials Science and Engineering A* **2020**, *772*, DOI 10.1016/j.msea.2019.138633.

[56] T. Nadu, **2023**, *55*, 21.

[57] T. H. Hsu, Y. J. Chang, C. Y. Huang, H. W. Yen, C. P. Chen, K. K. Jen, A. C. Yeh, *J Alloys Compd* **2019**, *803*, 30.

[58] T. LeBrun, T. Nakamoto, K. Horikawa, H. Kobayashi, *Mater Des* **2015**, *81*, 44.

[59] A. Kudzal, B. McWilliams, C. Hofmeister, F. Kellogg, J. Yu, J. Taggart-Scarff, J. Liang, *Mater Des* **2017**, *133*, 205.

[60] S. D. Meredith, J. S. Zuback, J. S. Keist, T. A. Palmer, *Materials Science and Engineering A* **2018**, *738*, 44.

[61] A. Barroux, N. Ducommun, E. Nivet, L. Laffont, C. Blanc, *Corros Sci* **2020**, *169*, DOI 10.1016/j.corsci.2020.108594.

[62] Z. Zhao, H. Wang, P. Huo, P. Bai, W. Du, X. Li, J. Li, W. Zhang, *Metals (Basel)* **2022**, *12*, 425.

[63] P. Auguste, A. Mauduit, L. Fouquet, S. Pillot, *UPB Scientific Bulletin, Series B: Chemistry and Materials Science* **2018**, *80*, 197.

[64] A. Yadollahi, N. Shamsaei, S. M. Thompson, A. Elwany, L. Bian, *ASME International Mechanical Engineering Congress and Exposition, Proceedings (IMECE)* **2015**, *2A-2015*, DOI 10.1115/IMECE2015-52362.

[65] D. J. Shaffer, A. E. Wilson-Heid, J. S. Keist, A. M. Beese, T. A. Palmer, *Materials Science and Engineering A* **2021**, *817*, DOI 10.1016/j.msea.2021.141363.

[66] T. H. Hsu, Y. J. Chang, C. Y. Huang, H. W. Yen, C. P. Chen, K. K. Jen, A. C. Yeh, *J Alloys Compd* **2019**, *803*, 30.

[67] A. Caballero, J. Ding, S. Ganguly, S. Williams, *J Mater Process Technol* **2019**, *268*, 54.

[68] X. Lou, P. L. Andresen, R. B. Rebak, *Journal of Nuclear Materials* **2018**, *499*, 182.

[69] G. Jacob, *NIST Advanced Manufacturing Series 100-14* **2018**, 1.

[70] F. Zhang, M. R. Stoudt, S. Hammadi, C. E. Campbell, E. A. Lass, M. E. Williams, *Metals (Basel)* **2021**, *11*, DOI 10.3390/met11121924.

[71] Y. Yang, W. H. Zeng, X. Z. Gong, L. H. Niu, Y. H. Wang, S. Li, X. Xu, C. Y. Wang, L. C. Zhang, *Mater Charact* **2023**, *200*, DOI 10.1016/j.matchar.2023.112912.

[72] M. P. Haines, M. S. Moyle, V. V. Rielli, V. Luzin, N. Haghdadi, S. Primig, *Addit Manuf* **2023**, *73*, 103686.

[73] S. An, D.-R. Eo, I. Sohn, K. Choi, *J Mater Sci Technol* **2023**, *166*, 47.

[74] H. R. Lashgari, E. Adabifiroozjaei, C. Kong, L. Molina-Luna, S. Li, *Mater Charact* **2023**, *197*, DOI 10.1016/j.matchar.2023.112661.

[75] C. N. Hsiao, C. S. Chiou, J. R. Yang, *Mater Chem Phys* **2002**, *74*, 134.

[76] Y. Sun, R. J. Hebert, M. Aindow, *Mater Des* **2018**, *156*, 429.

[77] A. Review, **2023**.

[78] D. Wang, L. Liu, G. Deng, C. Deng, Y. Bai, Y. Yang, W. Wu, J. Chen, Y. Liu, Y. Wang, X. Lin, C. Han, *Virtual Phys Prototyp* **2022**, *17*, 329.

[79] A. G. Demir, J. Kim, F. Caltanissetta, A. J. Hart, C. C. Tasan, B. Previtali, B. M. Colosimo, *J Mater Process Technol* **2022**, *301*, DOI 10.1016/j.jmatprotec.2021.117439.

[80] Z. Hu, S. Gao, J. Tai, S. Qu, J. Ding, X. Song, Z. Fan, *Mater Res Lett* **2023**, *11*, 231.

[81] K. Sofinowski, M. Wittwer, M. Seita, *Addit Manuf* **2022**, *52*, 102683.

[82] J. Zou, Y. Gaber, G. Voulazeris, S. Li, L. Vazquez, L. F. Liu, M. Y. Yao, Y. J. Wang, M. Holynski, K. Bongs, M. M. Attallah, *Acta Mater* **2018**, *158*, 230.

[83] R. R. Dehoff, M. Kirka, W. J. Sames, H. Bilheux, A. S. Tremsin, L. E. Lowe, S. S. Babu, *Materials Science and Technology (United Kingdom)* **2015**, *31*, 931.

[84] O. Gokcekaya, N. Hayashi, T. Ishimoto, K. Ueda, T. Narushima, T. Nakano, *Addit Manuf* **2020**, *36*, 101624.

[85] A. Arabi-Hashemi, X. Maeder, R. Figi, C. Schreiner, S. Griffiths, C. Leinenbach, *Appl Mater Today* **2020**, *18*, 100512.

[86] T. Mukherjee, J. W. Elmer, H. L. Wei, T. J. Lienert, W. Zhang, S. Kou, T. DebRoy, *Prog Mater Sci* **2023**, *138*, 101153.

[87] K. A. Sofinowski, S. Raman, X. Wang, B. Gaskey, M. Seita, *Addit Manuf* **2021**, *38*, 101809.

[88] S. Tekumalla, J. E. Chew, S. W. Tan, M. Krishnan, M. Seita, *Addit Manuf* **2022**, *59*, 103111.

[89] S. , et al. , Gao, *Under Review.* **2023**, DOI 10.1038/s41467-023-42326-y.

[90] A. Plotkowski, J. Ferguson, B. Stump, W. Halsey, V. Paquit, C. Joslin, S. S. Babu, A. Marquez Rossy, M. M. Kirka, R. R. Dehoff, *Addit Manuf* **2021**, *46*, 102092.

[91] S. Tekumalla, B. Selvarajou, S. Raman, S. Gao, M. Seita, *Materials Science and Engineering A* **2022**, *833*, 142493.

[92] M. R. O'Masta, E. C. Clough, J. H. Martin, *Comput Mater Sci* **2021**, *192*, 110317.

[93] J. H. Martin, B. Yahata, J. Mayer, R. Mone, E. Stonkevitch, J. Miller, M. R. O'Masta, T. Schaedler, J. Hundley, P. Callahan, T. Pollock, *Acta Mater* **2020**, *200*, 1022.

[94] M. L. Montero Sistiaga, R. Mertens, B. Vrancken, X. Wang, B. van Hooreweder, J. P. Kruth, J. van Humbeeck, *J Mater Process Technol* **2016**, *238*, 437.

[95] A. B. Spierings, K. Dawson, K. Kern, F. Palm, K. Wegener, *Materials Science and Engineering A* **2017**, *701*, 264.

[96] K. Schmidtke, F. Palm, A. Hawkins, C. Emmelmann, *Phys Procedia* **2011**, *12*, 369.

[97] D. Bayoumy, W. Kan, X. Wu, Y. Zhu, A. Huang, *J Mater Sci Technol* **2023**, *149*, 1.

[98] R. Ma, C. Peng, Z. Cai, R. Wang, Z. Zhou, X. Li, X. Cao, *J Alloys Compd* **2020**, *831*, 154773.

[99] R. Li, M. Wang, Z. Li, P. Cao, T. Yuan, H. Zhu, *Acta Mater* **2020**, *193*, 83.

[100] L. Zhou, H. Hyer, S. Thapliyal, R. S. Mishra, B. McWilliams, K. Cho, Y. Sohn, *Metall Mater Trans A Phys Metall Mater Sci* **2020**, *51*, 3215.

[101] S. Griffiths, J. R. Croteau, M. D. Rossell, R. Erni, A. De Luca, N. Q. Vo, D. C. Dunand, C. Leinenbach, *Acta Mater* **2020**, *188*, 192.

[102] J. Bi, Z. Lei, Y. Chen, X. Chen, Z. Tian, X. Qin, J. Liang, X. Zhang, *Intermetallics (Barking)* **2020**, *123*, DOI 10.1016/j.intermet.2020.106822.

[103] J. Bi, Z. Lei, Y. Chen, X. Chen, Z. Tian, N. Lu, X. Qin, J. Liang, *J Mater Sci Technol* **2021**, *69*, 200.

[104] H. Zhang, L. C. Zhang, H. Liu, X. Niu, M. C. Lam, W. Zhang, X. Jin, F. Chu, X. Wu, S. Cao, *Virtual Phys Prototyp* **2023**, *18*, DOI 10.1080/17452759.2023.2250769.

[105] J. Yuan, M. Zuo, M. Sokoluk, G. Yao, S. Pan, X. Li, *Minerals, Metals and Materials Series* **2020**, 318.

[106] T. Zheng, S. Pan, N. Murali, B. Li, X. Li, *Mater Lett* **2022**, *319*, 132268.

[107] S. Y. Zhou, Y. Su, H. Wang, J. Enz, T. Ebel, M. Yan, *Addit Manuf* **2020**, *36*, DOI 10.1016/j.addma.2020.101458.

[108] D. G. McCartney, *International Materials Reviews* **1989**, *34*, 247.

[109] L. Xinwei, S. Shi, H. Shuang, H. Xiaogang, Z. Qiang, L. Hongxing, L. Wenwu, S. Yusheng, D. Hui, *Addit Manuf* **2020**, *34*, DOI 10.1016/j.addma.2020.101326.

[110] B. Huang, Y. Liu, Z. Zhou, W. Cheng, X. Liu, *Vacuum* **2022**, *200*, 111030.

[111] M. Zuo, M. Sokoluk, C. Cao, J. Yuan, S. Zheng, X. Li, *Sci Rep* **2019**, *9*, 1.

[112] M. Sokoluk, C. Cao, S. Pan, X. Li, *Nat Commun* **2019**, *10*, 1.

[113] P. Wang, C. Gammer, F. Brenne, T. Niendorf, J. Eckert, S. Scudino, *Compos B Eng* **2018**, *147*, 162.

[114] A. Javadi, C. Cao, X. Li, *Procedia Manuf* **2017**, *10*, 531.

[115] R. Mertens, L. Baert, K. Vanmeensel, B. Van Hooreweder, *Material Design and Processing Communications* **2021**, *3*, DOI 10.1002/mdp2.161.

[116] A. Martin, M. Vilanova, E. Gil, M. S. Sebastian, C. Y. Wang, S. Milenkovic, M. T. Pérez-Prado, C. M. Cepeda-Jiménez, *Mater Charact* **2022**, *183*, DOI 10.1016/j.matchar.2021.111650.

[117] K. Wei, Z. Wang, X. Zeng, *Mater Lett* **2015**, *156*, 187.

[118] J. Liu, P. Wen, *Mater Des* **2022**, *215*, 110505.

[119] L. Deillon, F. Jensch, F. Palm, M. Bambach, *J Mater Process Technol* **2022**, *300*, 117416.

[120] A. Singh, A. Ramakrishnan, D. Baker, A. Biswas, G. P. Dinda, *J Alloys Compd* **2017**, *719*, 151.

[121] J. Bi, Z. Lei, Y. Chen, X. Chen, N. Lu, Z. Tian, X. Qin, *J Mater Sci Technol* **2021**, *67*, 23.

[122] A. Azimi, A. Shokuhfar, O. Nejadseyfi, H. Fallahdoost, S. Salehi, *Transactions of Nonferrous Metals Society of China (English Edition)* **2015**, *25*, 2499.

[123] N. Raja, B. S. S. Daniel, *Mater Perform Charact* **2019**, *8*, 1050.

[124] J. Osten, B. Milkereit, M. Reich, B. Yang, A. Springer, K. Nowak, O. Kessler, *Materials* **2020**, *13*, 1.

[125] A. Kumar, G. P. Chaudhari, S. K. Nath, *Mater Charact* **2022**, *191*, 112133.

[126] Kaiser Aluminium, **2008**, 1.

[127] N. Li, T. Wang, L. Zhang, L. Zhang, *J Alloys Compd* **2023**, *965*, 171463.

[128] D. G. Pekok, Mulla Ahmet, Rossitza Setchi, Michael Ryan, Emmanuel Brousseau, Quanquan Han, **n.d.**

[129] ASTM E8, *Annual Book of ASTM Standards 4* **2010**, 1.

[130] C. A. Schneider, W. S. Rasband, K. W. Eliceiri, *Nat Methods* **2012**, *9*, 671.

[131] X. liang ZOU, H. YAN, X. hui CHEN, *Transactions of Nonferrous Metals Society of China (English Edition)* **2017**, *27*, 2146.

[132] T. Liu, C. nian He, G. Li, X. Meng, C. sheng Shi, N. qin Zhao, *International Journal of Minerals, Metallurgy and Materials* **2015**, *22*, 516.

[133] A. M. Rubenchik, W. E. King, S. S. Wu, *J Mater Process Technol* **2018**, *257*, 234.

[134] A. K. Agrawal, B. Rankouhi, D. J. Thoma, *Curr Opin Solid State Mater Sci* **2022**, *26*, 101024.

[135] Z. Wang, R. Ummethala, N. Singh, S. Tang, C. Suryanarayana, J. Eckert, K. G. Prashanth, *Materials* **2020**, *13*, 1.

[136] M. Awd, F. Stern, A. Kampmann, D. Kotzem, J. Tenkamp, F. Walther, *Metals (Basel)* **2018**, *8*, DOI 10.3390/met8100825.

[137] W. D. Mirko Sinico, Suraj Dinkar Jadhav, Ann Witvrouw, Kim Vanmeensel, **2021**.

[138] J. Yin, D. Wang, L. Yang, H. Wei, P. Dong, L. Ke, G. Wang, H. Zhu, X. Zeng, *Addit Manuf* **2020**, *31*, 100958.

[139] J. T. Staley, *Technical Paper - Society of Manufacturing Engineers. EM* **1977**, *4*, DOI 10.1361/asmhba000.

[140] A. Woźnicki, B. Leszczyńska-madej, G. Włoch, J. Grzyb, J. Madura, D. Leśniak, *Metals (Basel)* **2021**, *11*, 1.

[141] N. Mahathaninwong, T. Plookphol, J. Wannasin, S. Wisutmethangoon, *Materials Science and Engineering A* **2012**, *532*, 91.

[142] Y. Lu, S. Su, S. Zhang, Y. Huang, Z. Qin, X. Lu, W. Chen, *Acta Mater* **2021**, *206*, 116632.

[143] A. Reichardt, R. P. Dillon, J. P. Borgonia, A. A. Shapiro, B. W. McEnerney, T. Momose, P. Hosemann, *Mater Des* **2016**, *104*, 404.

[144] D. Lehmhus, M. Busse, A. Von Hehl, E. Jägle, *MATEC Web of Conferences* **2018**, *188*, DOI 10.1051/matecconf/201818803013.

[145] C. Zhang, F. Chen, Z. Huang, M. Jia, G. Chen, Y. Ye, Y. Lin, W. Liu, B. Chen, Q. Shen, L. Zhang, E. J. Lavernia, *Materials Science and Engineering A* **2019**, *764*, 138209.

[146] A. Reichardt, A. A. Shapiro, R. Otis, R. P. Dillon, J. P. Borgonia, B. W. McEnerney, P. Hosemann, A. M. Beese, *International Materials Reviews* **2021**, *66*, 1.
[147] J. Noronha, J. Dash, M. Leary, M. Watson, M. Qian, E. Kyriakou, M. Brandt, *Jom* **2023**, *75*, 5729.
[148] K. Sanjeeviprakash, A. R. Kannan, N. S. Shanmugam, *Additive Manufacturing of Metal-Based Functionally Graded Materials: Overview, Recent Advancements and Challenges*, Springer Berlin Heidelberg, **2023**.
[149] C. Schneider-Maunoury, L. Weiss, P. Acquier, D. Boisselier, P. Laheurte, *Addit Manuf* **2017**, *17*, 55.
[150] T. Krajňák, M. Janeček, D. Preisler, J. Stráský, J. Kozlík, T. Škraban, M. Brázda, J. Džugan, *Journal of Materials Research and Technology* **2023**, *23*, 4527.
[151] D. K. Kim, W. Woo, E. Y. Kim, S. H. Choi, *J Alloys Compd* **2019**, *774*, 896.
[152] B. E. MacDonald, B. Zheng, B. Fields, X. Wang, S. Jiang, P. Cao, L. Valdevit, E. J. Lavernia, J. M. Schoenung, *Addit Manuf* **2023**, *61*, 103328.
[153] B. E. Carroll, R. A. Otis, J. P. Borgonia, J. O. Suh, R. P. Dillon, A. A. Shapiro, D. C. Hofmann, Z. K. Liu, A. M. Beese, *Acta Mater* **2016**, *108*, 46.
[154] L. D. Bobbio, B. Bocklund, E. Simsek, R. T. Ott, M. J. Kramer, Z. K. Liu, A. M. Beese, *Addit Manuf* **2022**, *51*, 102649.
[155] L. D. Bobbio, B. Bocklund, Z. K. Liu, A. M. Beese, *Materialia (Oxf)* **2021**, *18*, 101151.
[156] L. Li, *Heat Treating of Irons and Steels* **2018**, *4*, 397.
[157] P. Bassani, J. Fiocchi, A. Tuissi, C. A. Biffi, *Applied Sciences (Switzerland)* **2023**, *13*, DOI 10.3390/app13020882.
[158] C. Lesko, J. Walker, J. Middendorf, J. Gockel, *Jom* **2021**, *73*, 2878.
[159] T. Mukherjee, H. L. Wei, A. De, T. DebRoy, *Comput Mater Sci* **2018**, *150*, 369.
[160] C. Zhang, J. Zhu, H. Zheng, H. Li, S. Liu, G. J. Cheng, *International Journal of Extreme Manufacturing* **2020**, *2*, DOI 10.1088/2631-7990/ab9ead.
[161] W. Zhang, A. Chabok, B. J. Kooi, Y. Pei, *Mater Des* **2022**, *220*, 110875.
[162] I. Ferretto, D. Kim, N. M. Della Ventura, M. Shahverdi, W. Lee, C. Leinenbach, *Addit Manuf* **2021**, *46*, DOI 10.1016/j.addma.2021.102071.
[163] N. Sohrabi, R. Ran, P. A. Duro, C. Cayron, J. Jhabvala, V. Pejchal, O. Sereda, R. E. Logé, *J Alloys Compd* **2023**, *945*, 169209.
[164] K. Safaei, H. Abedi, M. Nematollahi, F. Kordizadeh, H. Dabbaghi, P. Bayati, R. Javanbakht, A. Jahadakbar, M. Elahinia, B. Poorganji, *Jom* **2021**, *73*, 3771.
[165] D. B. Miracle, O. N. Senkov, *Acta Mater* **2017**, *122*, 448.
[166] W. J. Davids, H. Chen, K. Nomoto, H. Wang, S. Babu, S. Primig, X. Liao, A. Breen, S. P. Ringer, *Acta Mater* **2021**, *215*, 117131.
[167] J. Yang, H. Yu, J. Yin, M. Gao, Z. Wang, X. Zeng, *Mater Des* **2016**, *108*, 308.
[168] H. D. Nguyen, A. Pramanik, A. K. Basak, Y. Dong, C. Prakash, S. Debnath, S. Shankar, I. S. Jawahir, S. Dixit, D. Buddhi, *Journal of Materials Research and Technology* **2022**, *18*, 4641.
[169] B. Soundararajan, D. Sofia, D. Barletta, M. Poletto, *Addit Manuf* **2021**, *47*, 102336.
[170] J. F. Lancaster, *Metallurgy of Welding* **1999**, 310.
[171] U. Scipioni Bertoli, B. E. MacDonald, J. M. Schoenung, *Materials Science and Engineering A* **2019**, *739*, 109.
[172] M. S. Moyle, N. Haghdadi, X. Z. Liao, S. P. Ringer, S. Primig, *J Mater Sci Technol* **2022**, *117*, 183.
[173] I. Superalloys, L. Li, *Heat Treating of Irons and Steels* **2018**, *4*, 397.
[174] S. M. Yeon, J. Yoon, T. B. Kim, S. H. Lee, T. S. Jun, Y. Son, K. Choi, *Metals (Basel)* **2022**, *12*, DOI 10.3390/met12050704.
[175] S. N. Lekakh, J. Qing, *Metals (Basel)* **2023**, *13*, 1154.
[176] T. Das, B. R. Kumar, B. K. Sahoo, H. Roy, A. K. Lohar, S. K. Samanta, K. Ghosh, *Mater Today Commun* **2024**, *38*, 108533.
[177] H. S. Oh, J. Kang, M. Jiang, C. C. Tasan, *Materials Science and Engineering: A* **2024**, *895*, 146122.
[178] F. Cantaboni, M. Tocci, P. S. Ginestra, A. Pola, *Procedia Structural Integrity* **2024**, *53*, 65.
[179] N. Li, Q. Wang, M. Bermingham, W. Niu, P. Han, N. Guo, S. Li, *Int J Plast* **2024**, *173*, 103885.
[180] S. A. Tyagi, M. Manjaiah, *Mater Today Commun* **2024**, *38*, 108267.
[181] M. S. Moyle, N. Haghdadi, F. Theska, M. P. Haines, X. Z. Liao, S. P. Ringer, S. Primig, *Mater Charact* **2024**, *209*, 113768.
[182] A. Dash, A. Bandyopadhyay, *Virtual Phys Prototyp* **2024**, *19*, DOI 10.1080/17452759.2023.2292695.

[183] J. Negron, M. Ali, A. Almotari, A. Algamal, A. Alafaghani, A. Qattawi, *Metallography, Microstructure, and Analysis* **2024**, DOI 10.1007/s13632-024-01051-8.

[184] P. Moreno-Garibaldi, M. Alvarez-Vera, J. A. Beltrán-Fernández, R. Carrera-Espinoza, H. M. Hdz-García, J. C. Díaz-Guillen, R. Muñoz-Arroyo, J. A. Ortega, P. Molenda, *Journal of Manufacturing and Materials Processing* **2024**, *8*, 48.

[185] S. Cao, H. Liu, J. Jiang, K. He, B. Lv, H. Zhang, L. Zhang, J. Meng, H. Deng, X. Niu, *Acta Metallurgica Sinica (English Letters)* **2024**, *37*, 181.

[186] M. Q. Kareem, T. Mikó, G. Gergely, Z. Gácsi, *Sci Prog* **2023**, *106*, 1.

[187] A. Yadollahi, N. Shamsaei, S. M. Thompson, A. Elwany, L. Bian, *ASME International Mechanical Engineering Congress and Exposition, Proceedings (IMECE)* **2015**, *2A-2015*, DOI 10.1115/IMECE2015-52362.

[188] B. Fields, M. Amiri, J. Lim, J. T. Pürstl, M. R. Begley, D. Apelian, L. Valdevit, **2024**, *2301037*, 1.

[189] F. Material, V. Kain, **2011**, *30*.

[190] A. L. Schaeffler, *Metal Progress* **1949**, 680.

[191] S. Austenitic, S. Steel, *Hot Cracking Phenomena in Welds III* **2011**, DOI 10.1007/978-3-642-16864-2.

[192] Z. T. Hilton, J. W. Newkirk, R. J. O'Malley, *Solid Freeform Fabrication 2017: Proceedings of the 28th Annual International Solid Freeform Fabrication Symposium - An Additive Manufacturing Conference, SFF 2017* **2020**, 377.

[193] H. Zhang, Y. Hou, X. Wang, X. Li, Y. He, F. Li, Y. Lu, H. Su, *Addit Manuf* **2024**, *81*, 103996.

[194] I. Ferretto, A. Sharma, D. Kim, N. M. Della Ventura, X. Maeder, J. Michler, E. Hosseini, W. J. Lee, C. Leinenbach, *Addit Manuf* **2023**, *78*, 103835.

[195] D. Kim, I. Ferretto, G. W. Park, C. Leinenbach, W. Kim, W. Lee, *J Alloys Compd* **2024**, *976*, 173226.

[196] K. Kubášová, V. Drátovská, M. Losertová, P. Salvetr, M. Kopelent, F. Kořínek, V. Havlas, J. Džugan, M. Daniel, *Materials* **2024**, *17*, 1248.

[197] J. Hu, Y. Jiang, Y. Yang, H. Xing, F. Han, G. Zhou, *Scr Mater* **2024**, *246*, 116066.

[198] M. Kas, T. Muslim, O. Yilmaz, T. Karagoz, E. Turedi, S. Gumus, A. Bayram, *International Journal of Advanced Manufacturing Technology* **2024**, DOI 10.1007/s00170-024-13411-3.

[199] A. Mansoura, N. Omidi, N. Barka, S. S. Kangranroudi, S. Dehghan, *Metals and Materials International* **2024**, DOI 10.1007/s12540-024-01650-8.

[200] F. Villaret, X. Boulnat, P. Aubry, J. Zollinger, D. Fabrègue, Y. de Carlan, *Materialia (Oxf)* **2021**, *18*, 101157.

[201] T. Hatakeyama, K. Sawada, M. Suzuki, M. Watanabe, *Addit Manuf* **2023**, *61*, 103350.

[202] S. Alsultan, C. Quitzke, Z. Cheng, L. Krüger, O. Volkova, M. Wendler, *Steel Res Int* **2021**, *92*, 1.

[203] A. Cladera, B. Weber, C. Leinenbach, C. Czaderski, M. Shahverdi, M. Motavalli, *Constr Build Mater* **2014**, *63*, 281.

[204] H. R. Dietterich, E. Lev, J. Chen, J. A. Richardson, K. V. Cashman, *Journal of Applied Volcanology* **2017**, *6*, DOI 10.1186/s13617-017-0061-x.

[205] P. Ninpetch, P. Kowitwarangkul, S. Mahathanabodee, P. Chalermkarnnon, P. Ratanadecho, *AIP Conf Proc* **2020**, *2279*, DOI 10.1063/5.0022974.

[206] B. Rankouhi, A. K. Agrawal, F. E. Pfefferkorn, D. J. Thoma, *Manuf Lett* **2021**, *27*, 13.

[207] B. Fields, M. Amiri, B. E. MacDonald, J. T. Pürstl, C. Dai, X. Li, D. Apelian, L. Valdevit, *Materials Science and Engineering: A* **2023**, *891*, 145901.

[208] Ati$^{\mathrm{TM}}$, **2012**, *1*, 1.

[209] M. Chen, S. Van Petegem, Z. Zou, M. Simonelli, Y. Y. Tse, C. S. T. Chang, M. G. Makowska, D. Ferreira Sanchez, H. Moens-Van Swygenhoven, *Addit Manuf* **2022**, *59*, 103173.

[210] M. Chen, M. Simonelli, S. Van Petegem, Y. Yau Tse, C. Sin Ting Chang, M. Grazyna Makowska, D. Ferreira Sanchez, H. Moens-Van Swygenhoven, *Mater Des* **2023**, *225*, 111458.

[211] A. Klassen, V. E. Forster, C. Körner, *Model Simul Mat Sci Eng* **2017**, *25*, DOI 10.1088/1361-651X/aa5289.

[212] T. Mukherjee, J. S. Zuback, A. De, T. DebRoy, *Sci Rep* **2016**, *6*, 1.

[213] K. Ma, H. Wen, T. Hu, T. D. Topping, D. Isheim, D. N. Seidman, E. J. Lavernia, J. M. Schoenung, *Acta Mater* **2014**, *62*, 141.

[214] N. Hansen, *Scr Mater* **2004**, *51*, 801.

[215] H. Wen, T. D. Topping, D. Isheim, D. N. Seidman, E. J. Lavernia, *Acta Mater* **2013**, *61*, 2769.

[216] Ø. Ryen, O. Nijs, E. Sjölander, B. Holmedal, H. E. Ekström, E. Nes, *Metall Mater Trans A Phys Metall Mater Sci* **2006**, *37*, 1999.
[217] J. E. Bailey, P. B. Hirsch, *Philosophical Magazine* **1960**, *5*, 485.
[218] Z. Guo, W. Sha, *Mater Trans* **2002**, *43*, 1273.
[219] B. Cheng, K. Chou, *Proceedings - 26th Annual International Solid Freeform Fabrication Symposium - An Additive Manufacturing Conference, SFF 2015* **2020**, 1182.
[220] G. Liu, C. Huang, R. Su, T. Özel, Y. Liu, L. Xu, *Int J Mech Sci* **2019**, *155*, 417.
[221] C. Körner, M. Markl, J. A. Koepf, *Metall Mater Trans A Phys Metall Mater Sci* **2020**, *51*, 4970.
[222] D. S. Wire, A. Additive, **2023**, 1.

SUPPLEMENTARY FIGURES

Chapter 1 Supplementary

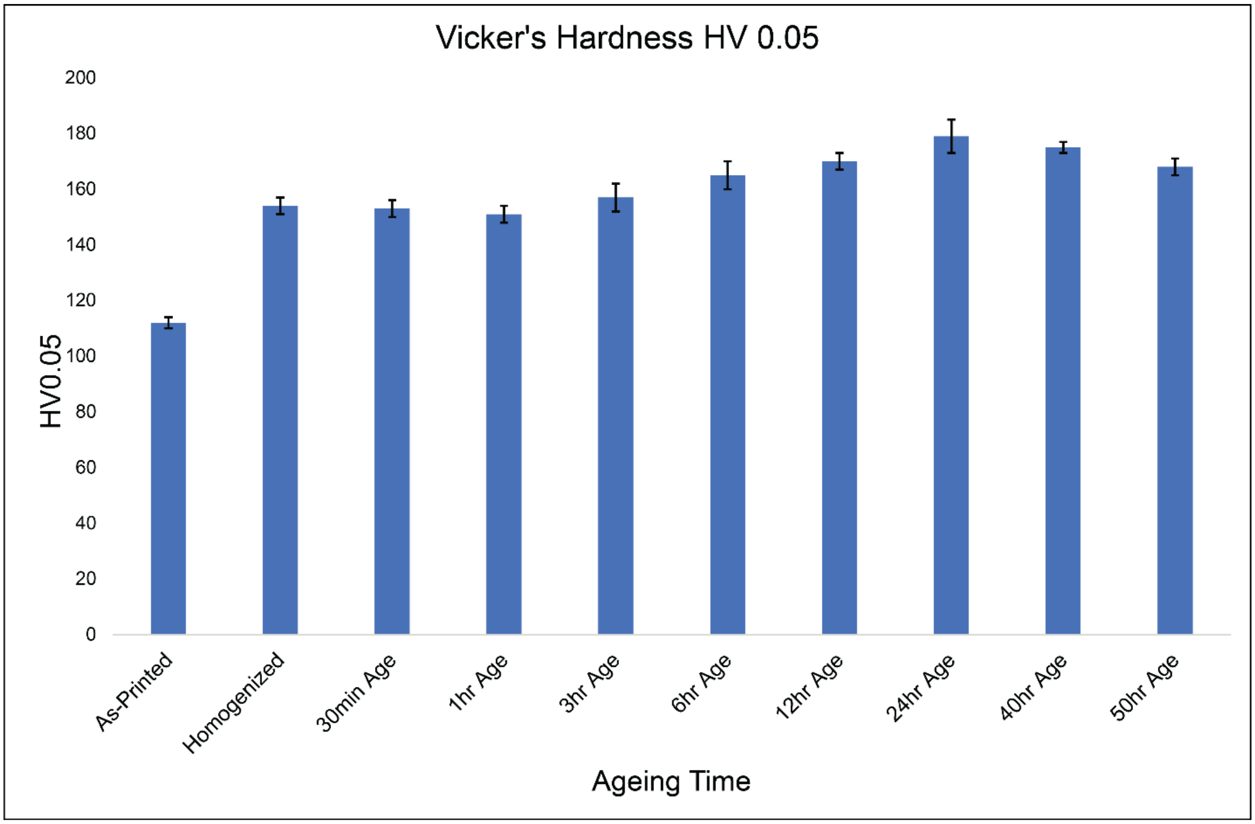

Figure S1.1. Vicker’s hardness across diferent ageing times at 130ºC. Peak age occurs at 24 hours.

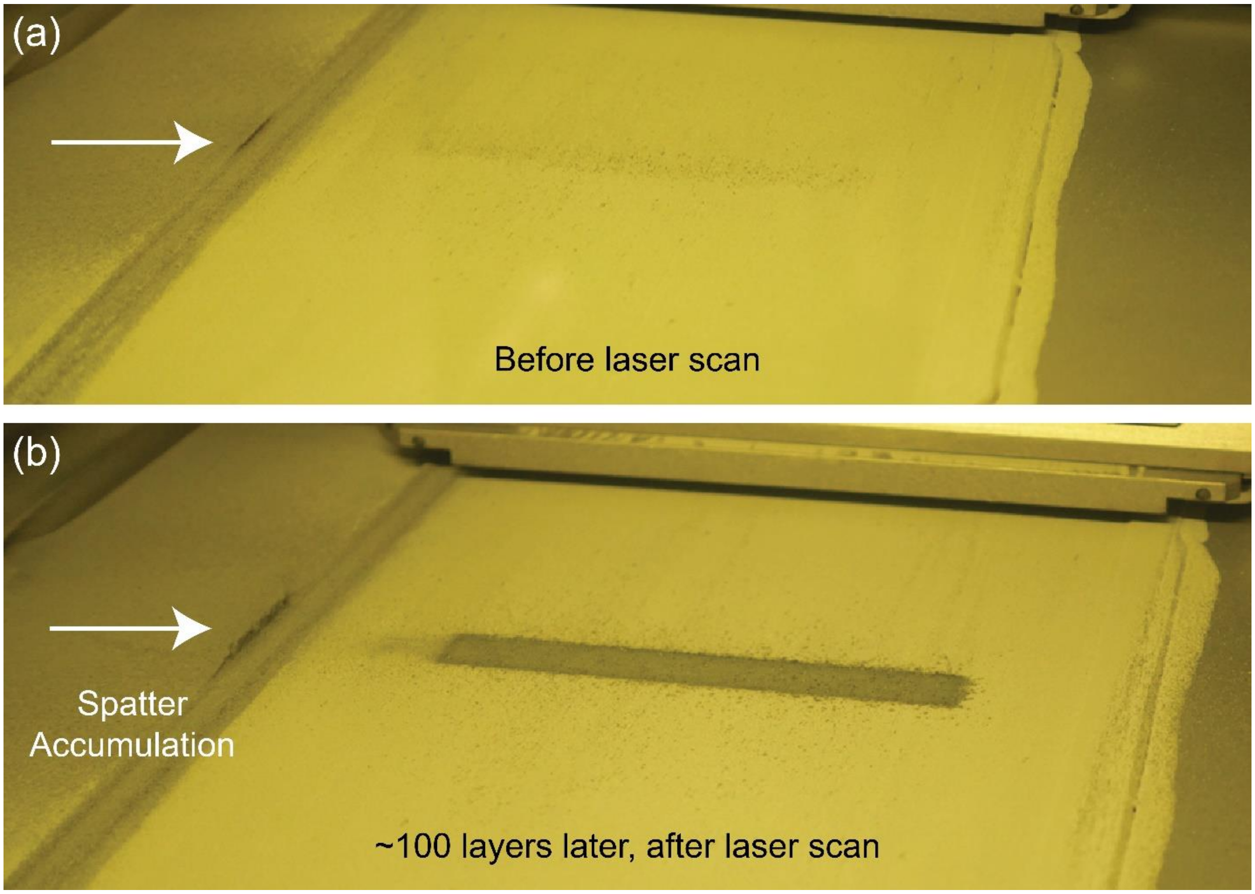

Figure S1.2. Snapshot of the powder bed (a) before the laser scan and (b) after the laser scan 100 layers later. The spattered powder can be seen on the powder bed where the laser does not scan. Most of the spatter accumlates on the left of the build chamber, as directed by the inlet gas flow from right to left.

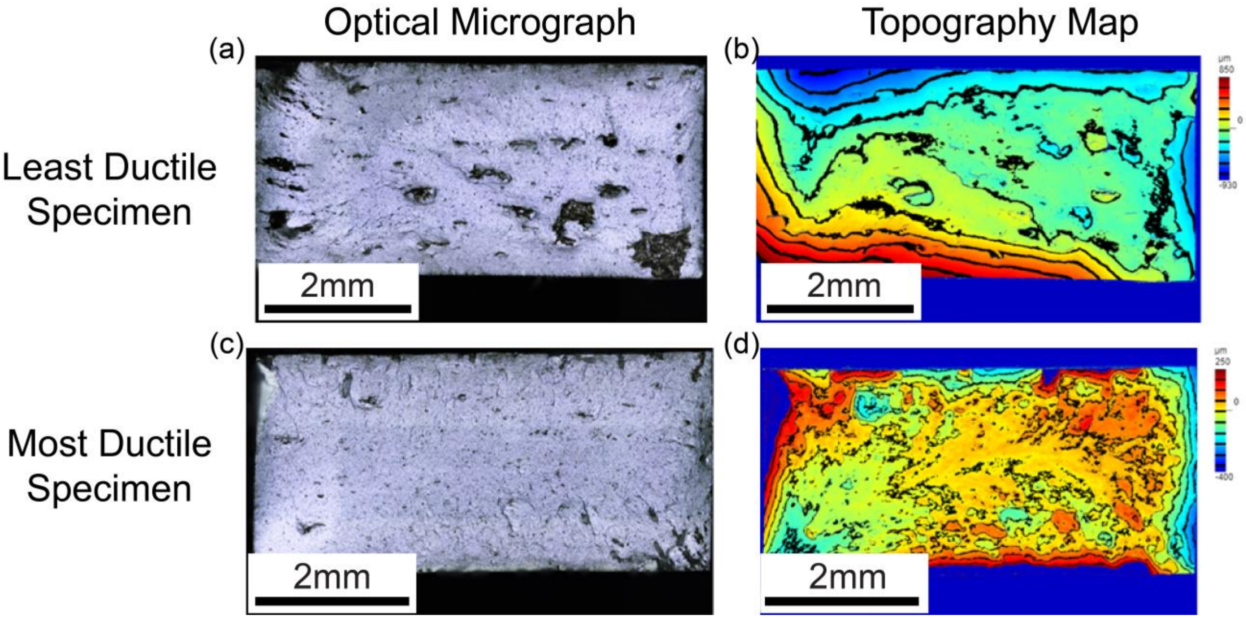

Figure S1.3: Post-HIP homogenized (a) optical and (b) topography map of the least ductile specimen fracture surface, further analyzed in Figure 1.13. Post-HIP homogenized (c) optical and (d) topography map of the most ductile specimen fracture surface. There is an abundance of discolored inclusions in the least ductile specimen in comparison the most ductile specimen.

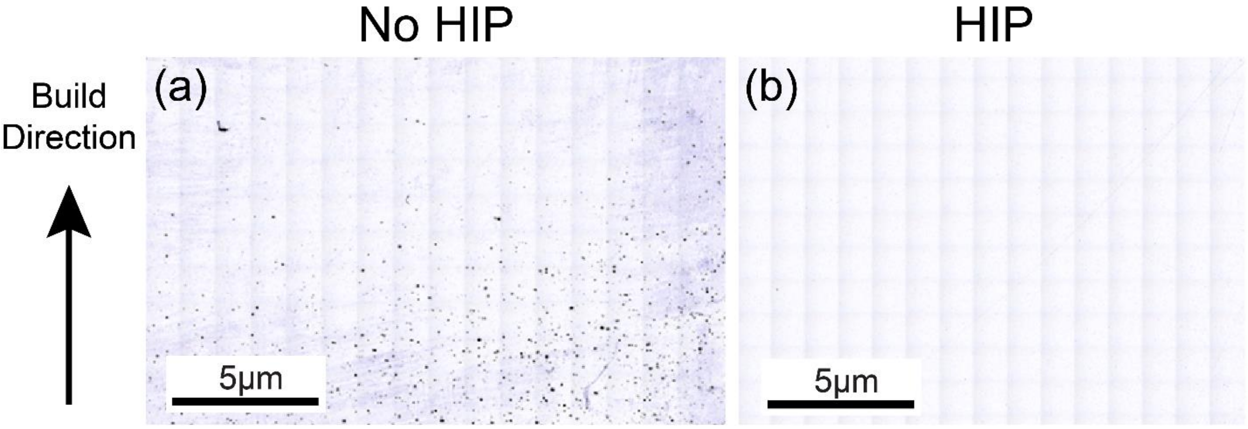

Figure S1.4: Representative porosity in a tensile specimen (a) Pre-HIP and (b) Post-HIP.

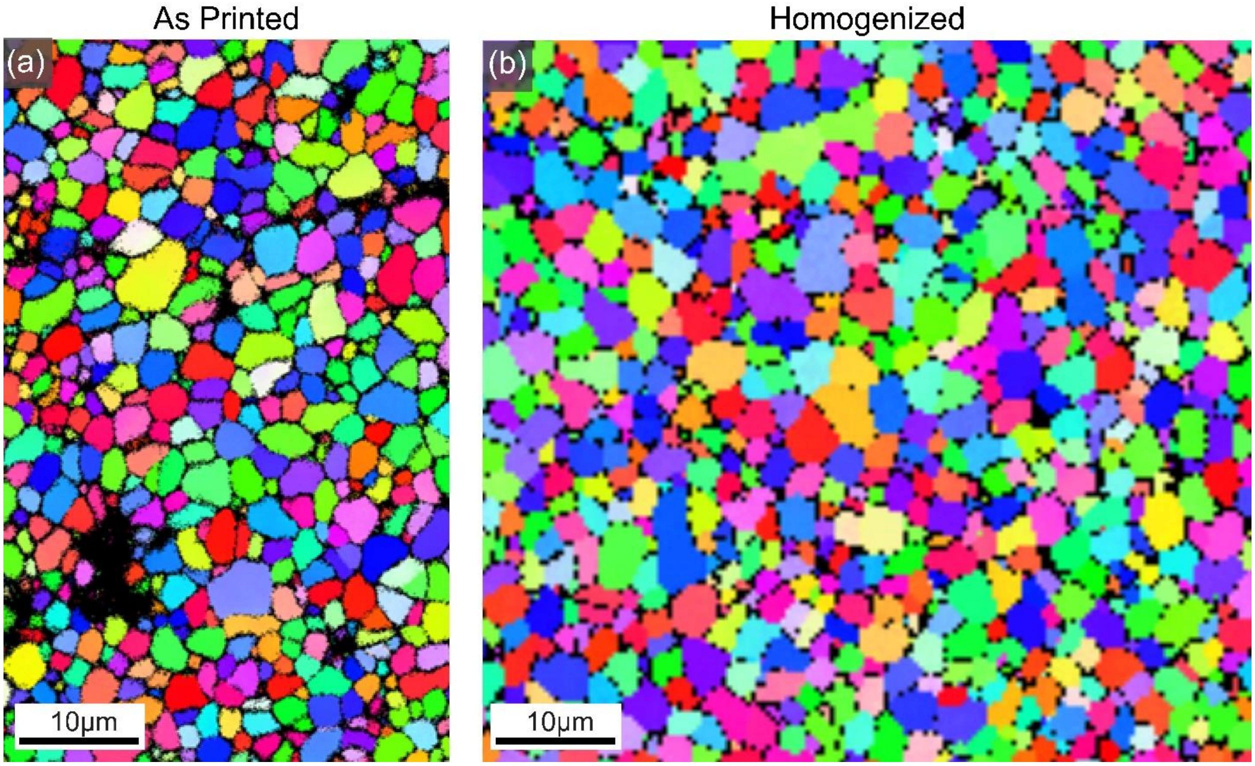

Figure S1.5: EBSD of (a) As Printed and (B) Homogenized *400W* samples.

Table S1.1. Chemical composition (wt%) of each printed sample obtained from ICP-MS, with TiC percentage provided by MetaLi^{TM}. The optimal conditions referred to as *200W* and *400W* are the 200W, 400mm/s and 400W, 750mm/s samples respectively.

Laser Power (W), Scan Speed (mm/s)	Energy Density (J/mm^3)	Al	Zn	Mg	Cu	TiC
200, 200	333	Bal.	8.6	2.5	2.2	1.5
200, 300	222	Bal.	9.5	2.6	2.2	1.5
200, 400	**167**	**Bal.**	**10.3**	**2.7**	**2.2**	**1.5**
200, 500	133	Bal.	9.7	2.6	2.1	1.5
200, 750	89	Bal.	10.8	2.8	2.1	1.5
200, 1000	67	Bal.	11.5	2.9	2.1	1.5
300, 250	400	Bal.	7.6	2.4	2.3	1.5
300, 500	200	Bal.	9.5	2.7	2.2	1.5
300, 750	133	Bal.	10.3	2.7	2.1	1.5
300, 1000	100	Bal.	10.6	2.8	2.1	1.5
300, 1250	80	Bal.	10.9	2.8	2.0	1.5
400, 250	533	Bal.	7.6	2.3	2.2	1.5
400, 500	267	Bal.	9.8	2.8	2.3	1.5
400, 750	**178**	**Bal.**	**10.5**	**2.7**	**2.0**	**1.5**
400, 1000	133	Bal.	11.1	2.7	2.1	1.5
400, 1250	107	Bal.	10.7	2.8	2.1	1.5

Chapter 2 Supplementary

17-4 PH Sample geometry and printing strategy

The geometry and printing strategies for all samples printed in this work are depicted in Figure S2.1.

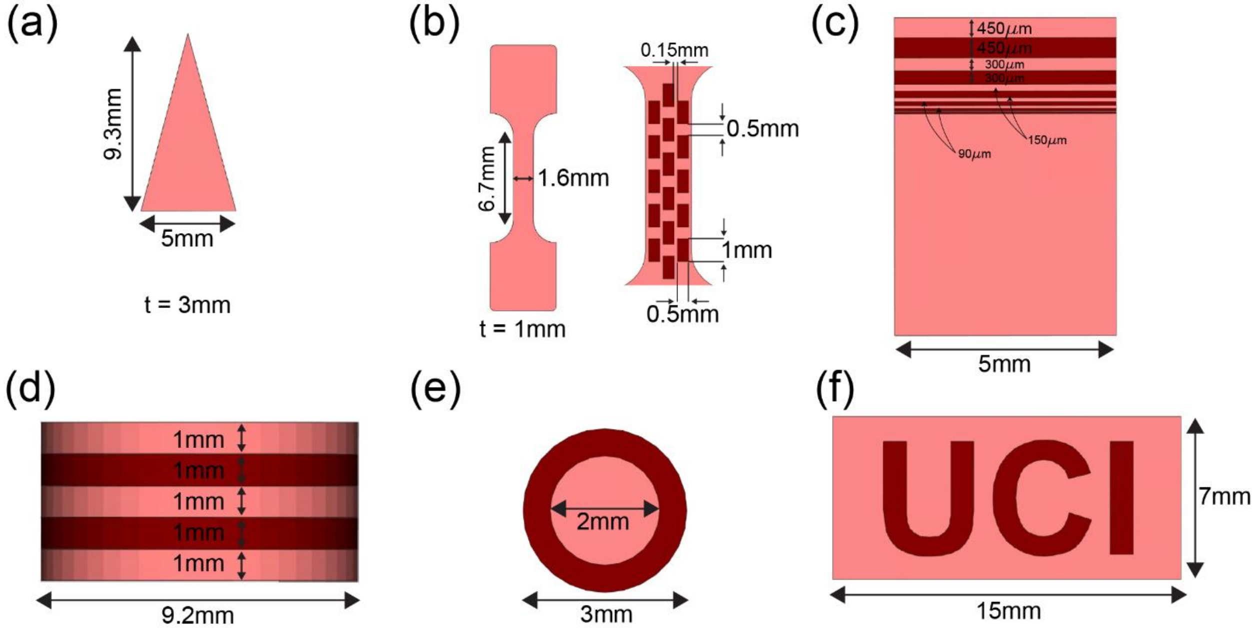

Figure S2.1. Geometry of all printed samples. (a) Wedge specimens are printed with four different energy densities (50, 100, 250 and 400 J/mm^3) and two different printing orientations (with triangles parallel and perpendicular to the build platform); (b) Dog bone specimens are printed perpendicular to the build platform, with three different strategies: uniform energy density of 100 J/mm^3, uniform energy density of 400 J/mm^3, and hybrid 'brick-and-mortar' strategy, with bricks printed at 400 J/mm^3 embedded in a mortar printed at 100 J/mm^3; (c,d): Gradient blocks are printed with the gradient perpendicular to the build platform, alternating layers printed with energy densities of 100 (light) and 400 J/mm^3 (dark). (e) The hybrid cylindrical specimen is printed with the cylinder axis perpendicular to the build platform, with a shell printed at 400 J/mm^3 (dark) encompassing a core printed at 100 J/mm^3 (light); (f) The UCI logo is printed parallel to the build platform, with letters printed at 400 J/mm^3 (dark) embedded in a volume at 100 J/mm^3.

Photographs of the dog bone specimens printed with energy densities of 100J/mm^3 and 400J/mm^3 are shown in Figure S2.2a. The hybrid 'brick-and-mortar'-inspired sample is shown in Figure S2.2b.

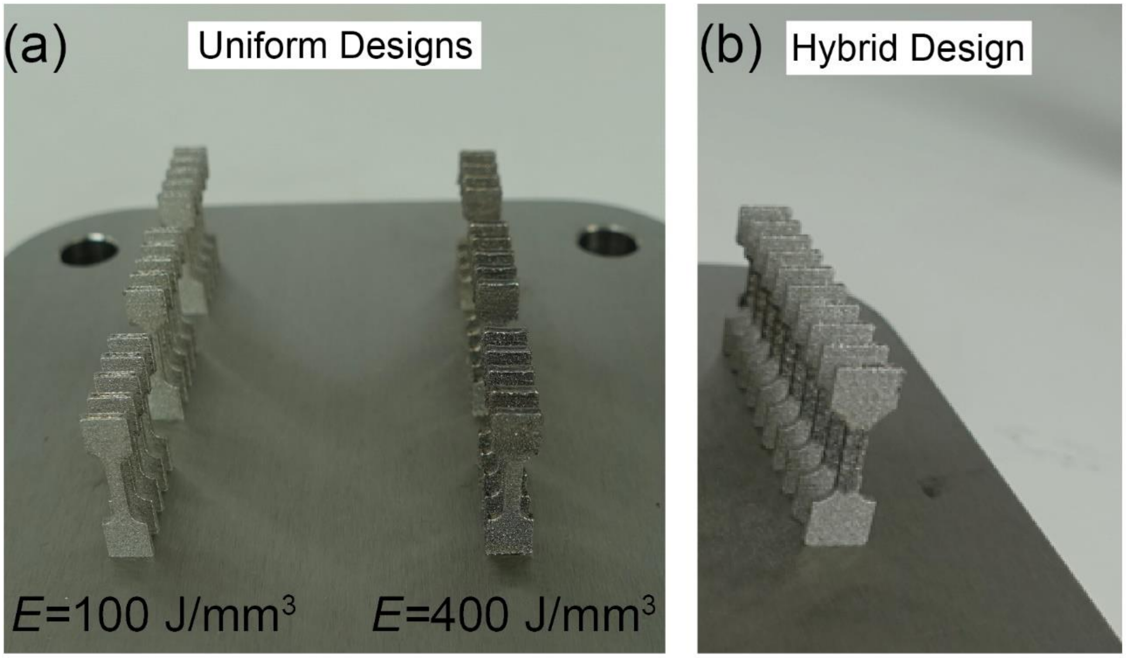

Figure S2.2. (a) Builds of dog bone specimens printed with energy densities of 100 J/mm^3 and 400 J/mm^3. (b) Build of the hybrid 'brick-and-mortar'-inspired dog bone specimens.

Microstructure of 17-4PH specimens printed with energy density of 100 J/mm^3

Figure S2.3 depicts optical images of different samples, etched to reveal the microstructure, printed with energy densities of 100 J/mm^3: (a) a wedge sample printed with the triangle parallel to the build platform; (b) the E=100 J/mm^3 portion of a gradient block specimen, printed with the gradient perpendicular to the build platform; (c) a dual-track thin-wall specimen, printed perpendicular to the build platform. Two important results emerge: (i) the martensitic and ferritic microstructures are qualitatively similar in all samples; (ii) the outer borders of all specimens clearly show a fully martensitic microstructure, with ferritic regions occupying the space between adjacent laser tracks. EBSD band contrast, phase map, and IPF-X for a selected region in the thin-wall specimen are shown in Figure S2.3d-f, respectively. The phase map in Figure 2.3e confirms the presence of fine martensitic regions (shown in blue) along the border of the wall, with columnar ferritic grains (shown in red) epitaxially growing near the center of the specimen, extending through multiple build layers. As the outer border of all specimens is always the final scan for our ‘borders inside-out’ scan strategy, these findings prove that initial solidification from the molten powder state always produces a martensitic microstructure, regardless of the energy density, and that ferritic grains exclusively form between adjacent laser scan lines, upon reheating/cooling cycles, as long as the energy density is sufficiently low.

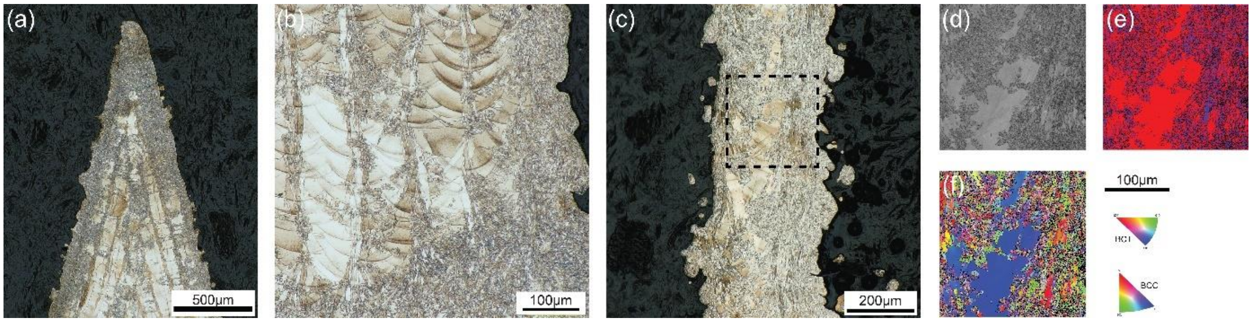

Figure S2.3. Optical images of different samples, etched to reveal the microstructure, printed with energy densities of 100 J/mm3: (a) a wedge sample printed with the triangle parallel to the build platform; (b) the E=100 J/mm3 portion of a gradient block specimen, printed with the gradient perpendicular to the build platform; (c) a dual-track thin-wall specimen, printed perpendicular to the build platform. (d) BSD band contrast, (e) phase map (red = ferrite, blue = martensite), and (f) IPF-X for a selected region from (c).

Selected-Area-Diffraction-Patterns (SADPs) are extracted from as-printed samples, processed with energy densities of 100 J/mm^3 and 400 J/mm^3, as shown in Figure S2.4. Notice the polycrystalline microstructure consisting of small martensitic laths for the *E*=400 J/mm^3 sample (Figure S2.4c), in contrast with the single grain structure of the 100 J/mm^3 sample (Fig. S2.4a). These differences are clearly confirmed by the SADP for the two samples, whereby the *E*=100 J/mm^3 sample shows a single grain orientation (Figure S2.4b), in contrast with the visible diffraction rings from the *E*=100 J/mm^3 sample (Figure S2.4c). The diffraction pattern along <011> exclude the presence of FCC austenite. This is further confirmed by the diffraction pattern along <111>, on the basis of lattice parameters, although the resolution is insufficient to clearly disambiguate BCC ferrite from low-aspect ratio BCT martensite.

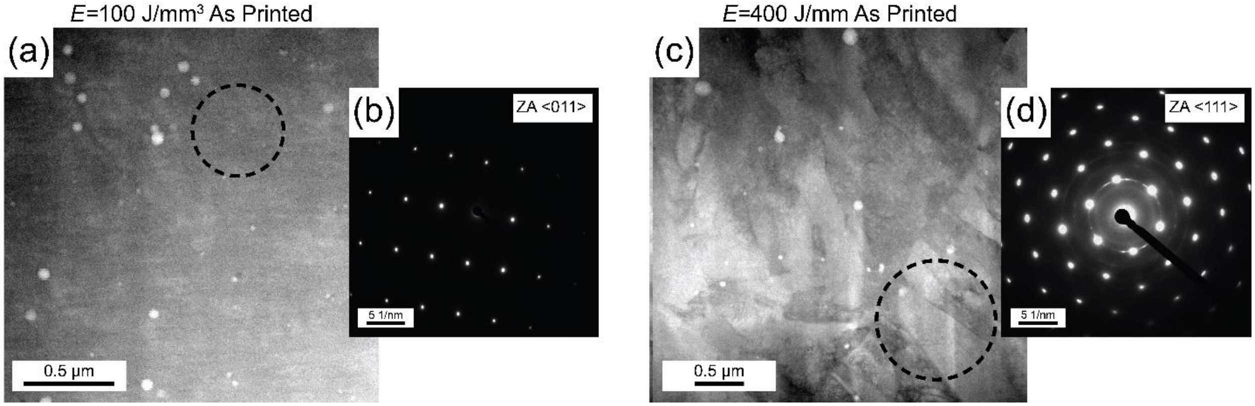

Figure S2.4. TEM micrographs of samples printed with (a) E=100 J/mm^3 and (c) 400 J/mm^3, in the as-printed condition. Selected Area Diffraction Patterns (SADPs) collected from (b) ferritic E=100 J/mm^3 sample and (d) martensitic

Chapter 3 Supplementary

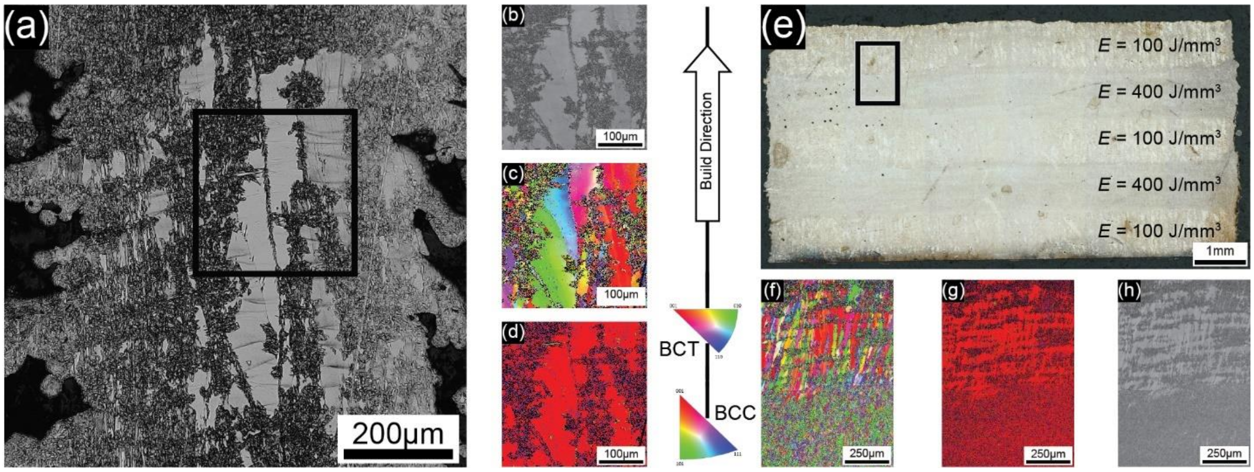

Figure S3.1. (a) Monochrome micrograph of dual-phase specimen processed with LED = 0.3 J/mm & VED=100 J/mm^3, and (b-d) EBSD band contrast, IPF-X, and phase maps respectively. (e) Optical color micrograph of an etched hybrid sample printed by alternating layers at VED=100 J/mm^3 and 400 J/mm^3, with IPF-X maps, phase maps, and band contrast maps shown in (f-h) for the inset in (e), respectively. Red indicates ferrite and blue indicates martensite in (d,g). The build direction is upwards throughout the figure.

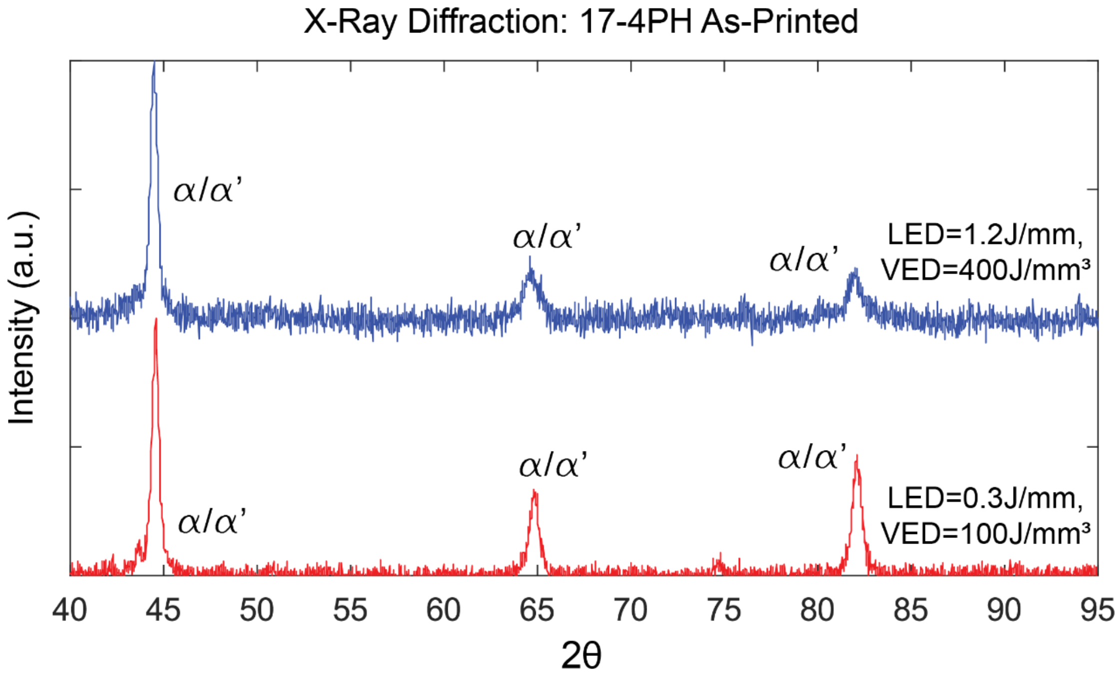

Figure S3.2. X-ray diffraction of bulk samples printed with (a) pure martensitic microstructure and (b) martensitic/ferritic microstructure. XRD alone cannot differentiate between BCC-ferrite (α) and low carbon, low aspect ratio BCT-martensite (α'). Peak strain broadening is larger than the difference in peak angles, with the VED=400J/mm^3 higher strained BCT microstructure having broader peaks than VED=100J/mm^3.

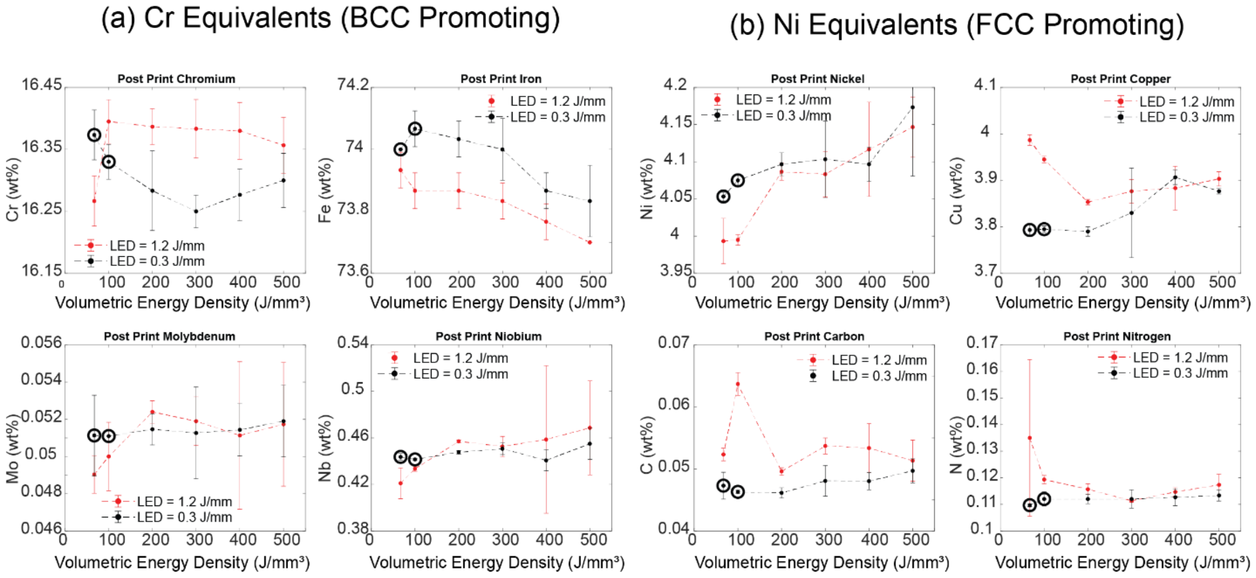

Figure S3.3. Individual contributing element compositions which are (a) chromium equivalent and promote δ-ferrite stability, (b) nickel equivalent and eliminate δ-ferrite.

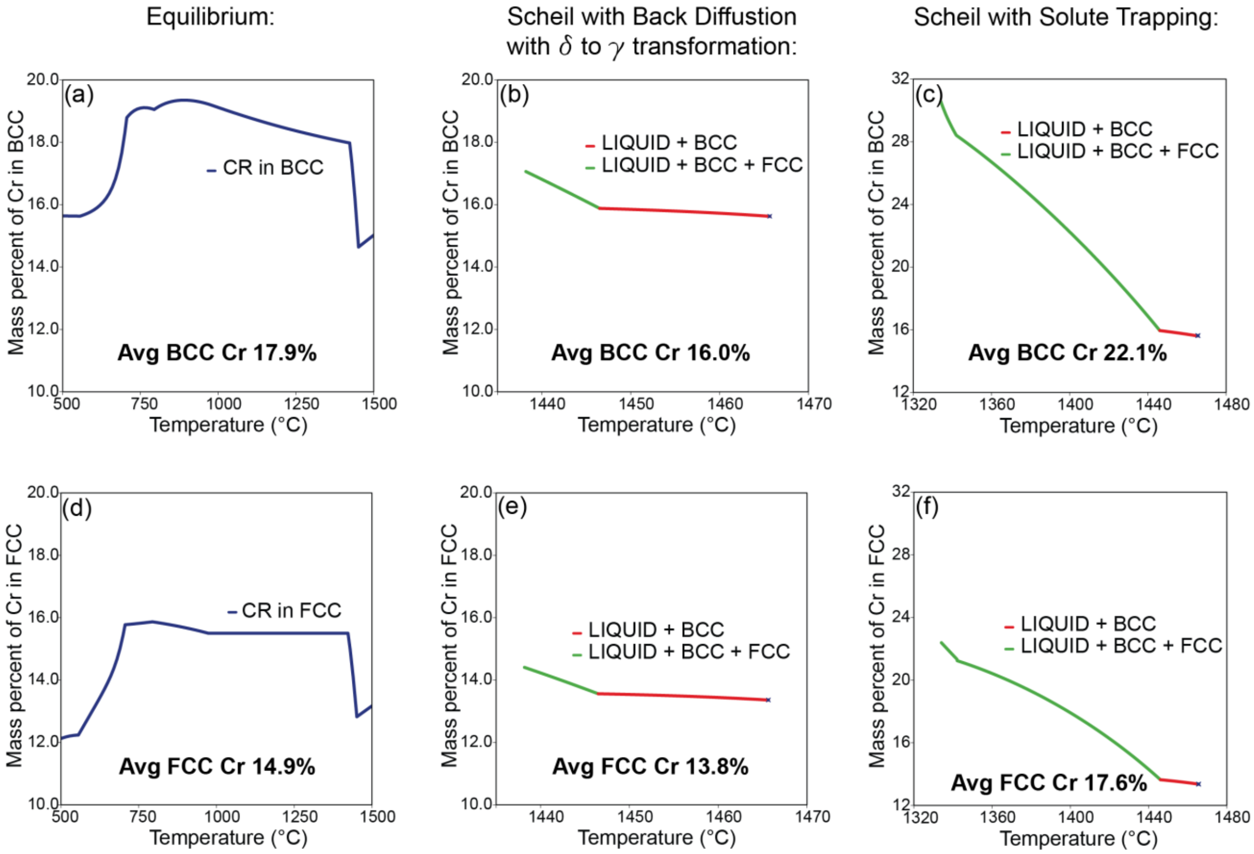

Figure S3.4. CALPHAD calculations of mass percent Cr in BCC under (a) equilibrium, (b) Scheil solidification with back diffusion and δ to γ transformation, (c) Scheil with solute trapping. Cr in FCC under (d) equilibrium, (e) Scheil solidification with back diffusion and δ to γ transformation, (f) Scheil with solute trapping.

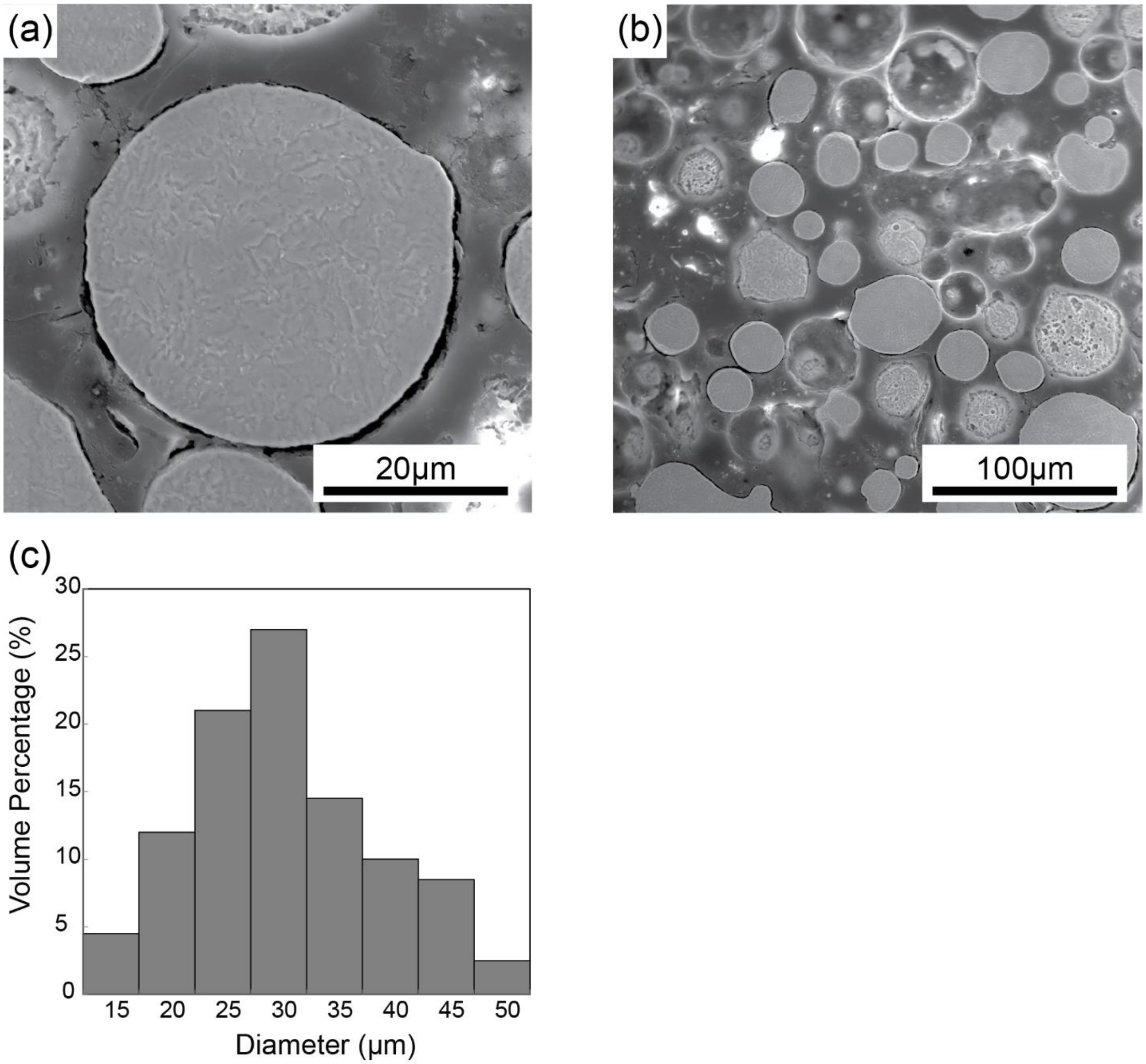

Figure S3.5. SEM image of (a) an individual etched 17-4PH powder particle, (b) multiple particles, and the corresponding (c) powder size distribution.

Table S3.1. Nominal and EDS measured composition of 17-4PH Carpenter powder feedstock.

	Fe	Cr	Ni	Cu	Nb	C	N
Nominal	Bal.	15.0-17.5%	3.0-5.0%	3.0-5.0%	0.15-0.45%	0.07%	0.1%
SEM-EDS	Bal.	16.2-17.0%	3.9-4.8	4.0-5.3%	0.4-0.6%	-	-

APPENDICES

Appendix 1: Analytical Estimation of Selective Elemental Evaporation

This appendix recalls the analytical models used for calculating the mass loss of each individual constituent element. We calculate the vaporization flux J_i for each element *i* using the Langmuir equation[118]:

$$J_i = \Phi_{\mathrm{con}} \cdot a_i \cdot p_{\mathrm{sat},i} \sqrt{\frac{M_i}{2 \cdot \pi \cdot R \cdot T}}, \tag{1}$$

where $p_{\mathrm{sat},i}$ is the saturated vapor pressure of element i, Φ_{con} is a non-dimensional factor accounting for condensation (Φ_{con}= 0.82 is its maximum value, routinely reached under LPBF conditions [211]), M_i and a_i are the molar mass and the activity of element *i*, respectively. a_i has been shown to be modeled accurately by the mole fraction (ideal solution model) [52], taken as 0.048 and 0.079 for Mg and Zn, respectively.

The saturated vapor pressure can be calculated from the Clausius-Clapeyron equation[118]:

$$p_{\mathrm{sat},i} = p_0 \cdot \exp\left(\frac{\Delta H_{v,i}}{RT} \cdot \frac{T - T_{b,i}}{T_{b,i}}\right), \tag{2}$$

where p_0 is the ambient or chamber pressure, $\Delta H_{v,i}$ is the latent heat of vaporization of element *i*, $T_{b,i}$ is the boiling point of element *i*, *R* is the gas constant, and *T* is the temperature of the melt pool. The thermophysical properties of our bulk material and constituent elements are reported in Table A1.1. A chamber pressure $p_0 = 4\ mbar$ is measured during printing. The melt pool temperature can be estimated from the Rosenthal equation as[134]:

$$T = \frac{\alpha \cdot P}{\pi \cdot \rho \cdot C_p \cdot \sqrt{D_t \cdot v \cdot r^3}} \tag{3}$$

with α the absorptivity of the powder bed, *P* the laser power, ρ, C_p and D_t the density, specific heat and thermal diffusivity of the alloy, respectively, *v* the scan speed, and *r* the laser spot radius. Temperature calculations for our process parameters result in melt pool temperatures much higher than the boiling point of the highest boiling point element, in our case aluminum. As this model does not account for the latent heat of vaporization, these predictions merely indicate that the temperature reaches the boiling point of aluminum. As the melt pool temperature cannot exceed this value[20,118], we take $T=T_{b,Al}$ = 2470°C.

With the known vaporization flux, the mass of evaporated element i, Δm_i, and the relative evaporation from its initial mass $m_{0,i}$ can be calculated as:[212]

$$\Delta m_i = \frac{L_{\mathrm{mp}} \cdot A_{\mathrm{s}} \cdot J_i}{v} \tag{4}$$

$$\frac{\Delta m_i}{m_{0,i}} = \frac{\Delta m_i}{\rho \cdot V_{\mathrm{mp}} \cdot f_i} \tag{5}$$

where L_{mp}, A_{s} and V_{mp} are the length, surface area and volume of the melt pool, respectively, J_i is the vaporization flux (Eq. (1)), v is the scan speed, ρ is the density, and f_i is the initial mass fraction of element i.

The melt pool cross section was estimated using the Rosenthal equations, which give analytical expressions of a semi-elliptical melt pool cross section. This has been shown to agree experimentally with LPBF melt pool width and depth measurements[133,134]. While the Rosenthal solutions only provide two-dimensional section predictions (width, W_{mp} and depth, D_{mp}), the pool length, L_{mp} can be estimated by empirical proportional scaling laws. Hence, we have[133,134]:

$$W_{\mathrm{mp}} = 2D_{mp} = \sqrt{\frac{8 \cdot \alpha \cdot P}{\pi \cdot \mathrm{e} \cdot \rho \cdot c_p \cdot v \cdot (T_{\mathrm{m}} - T_{\mathrm{s}})}} \tag{6}$$

$$L_{\mathrm{mp}} = \frac{r}{p^2} \cdot [0.0053 - 0.21 \cdot p \cdot B + 1.3 \cdot p^2 - (0.11 + 0.17 \cdot B) \cdot p^2 \cdot \ln(p) + \\ + B \cdot (0.75 \cdot p^2 + 0.23 \cdot p - 0.0062)] \tag{7}$$

where $p = \frac{D_t}{v \cdot r}$ and $B = T/T_m$ are dimensionless parameters used to characterize melt pool proportional scaling. We can readily extract:

$$A_\mathrm{s} = W_\mathrm{mp} \cdot L_\mathrm{mp}/1.75 \quad (8)$$

$$V_\mathrm{mp} = W_\mathrm{mp} \cdot D_\mathrm{mp} \cdot L_\mathrm{mp}/3.5 \quad (9)$$

Table A1.1. Thermophysical properties used in vaporization calculations.

Property	Value	Property	Value
Laser Power (P)	200 W	Boiling point Mg ($T_{b,Mg}$)	1091°C
Scan Speed (v)	125 – 1000 mm/s	Latent Heat Zn ($\Delta H_{v,Zn}$)	115 kJ/mol
Density ($\boldsymbol{\rho}$)	2900 kg/m^3	Latent Heat Mg ($\Delta H_{v,Mg}$)	134 kJ/mol
Thermal Diffusivity (D_t)	4.8x10^{-5} m^2/s	Laser spot radius (r)	40 µm
Substrate temp (T_s)	200°C	Powder Bed Absorption (α)	0.7
Boiling point Al ($T_{b,Al}$)	2470°C	Specific Heat (c_p)	960 J/kgK
Boiling point Zn ($T_{b,Zn}$)	901°C	Thermal Conductivity (k)	135 W/mK

Appendix 2: Analytical Modeling of Strengthening Mechanisms

This appendix recalls the analytical models used to estimate the impact of the strengthening mechanisms operating in the presently investigated Al 7xxx alloy, including: (i) grain boundary (Hall-Petch) strengthening ($\Delta\sigma_\mathrm{gb}$), (ii) solid-solution strengthening ($\Delta\sigma_\mathrm{ss}$), (iii) dislocation strengthening ($\Delta\sigma_\mathrm{dis}$), and (iv) precipitate/dispersoid (Orowan) strengthening ($\Delta\sigma_\mathrm{orowan}$). Table A2.1. provides the values of the parameters that are used to quantitatively describe these strengthening mechanisms. The strengthening mechanisms contribute to the yield strength so that:

$$\sigma_\mathrm{y} = \sigma_0 + \Delta\sigma_\mathrm{gb} + \Delta\sigma_\mathrm{ss} + \Delta\sigma_\mathrm{dis} + \Delta\sigma_\mathrm{orowan} \quad (10)$$

with σ_0 = 29 MPa taken as the yield strength of pure singe-crystal aluminum[213].

Table A2.1. Physical meaning and values used for theoretical strengthening mechanism calculations.

Symbol	Definition	Value [50]
$\boldsymbol{b}$	Burgers vector	0.286 nm

$\boldsymbol{k_y}$	Hall-Petch coefficient	0.12 $\mathrm{MPa}/\sqrt{\mathrm{m}}$
$\boldsymbol{M}$	Mean orientation factor	3.06
$\boldsymbol{G}$	Shear modulus	26.9 GPa
$\boldsymbol{\alpha}$	Constant for FCC metals	0.3
$\boldsymbol{\nu}$	Poisson ratio	0.33

(i) Grain boundary strengthening is governed by the Hall-Petch relationship, describing the strength of a polycrystalline metal as:[214]

$$\Delta\sigma_{\mathrm{gb}} = k_{\mathrm{y}} \cdot d^{-\frac{1}{2}} \tag{11}$$

The average grain diameter (d) can be measured from SEM and TEM image analysis (Figures 1.10 and 1.11) as 1.61μm and 1.71μm for the homogenized and aged samples, respectively. We obtain $\Delta\sigma_{\mathrm{gb}}$ = 95MPa and 92MPa for the homogenized and aged samples, respectively, in good agreement with reported values for fine-grained aluminum[215].

(ii) Solid-solution strengthening is governed by the Fleischer equation:[216]

$$\Delta\sigma_{ss} = M \cdot G \cdot b \cdot \varepsilon^{3/2} c^{1/2} \tag{12}$$

where M is the mean orientation factor, G the shear modulus, b the magnitude of the Burger's vector, c the solute concentration, and ε the micro-strain. Values for the parameter M, G, and b are given in Table A2.1. The micro-strain (ε) can be extracted through XRD measurements from the slope of a linear regression of the Williamson-Hall equation:

$$B_{HKL} \cdot \cos\theta_{HKL} = \frac{K \cdot \lambda}{d} + 4 \cdot \varepsilon \cdot \sin\theta_{HKL} \tag{13}$$

where the peak broadening (B_{HKL}) is extracted as the full-width-half-max (FWHM) from individual XRD peaks, using Cu K_α radiation with wavelength λ = 0.154nm, with the constant K = 0.9[213]. The power of ½ in Eq. 12 is empirically determined, however it has been verified for grains larger than 100nm[214,215].

Assuming that all the Zn, Mg, and Cu atoms in the alloy are found in solid-solution, Eq. (12) yields a theoretical upper-bound $\Delta\sigma_{ss}$ = 125MPa. This estimate is expected to be more accurate for the homogenized state than for the aged state.

(iii) Dislocation interaction strengthening is governed by the Bailey-Hirsch relation:[217]

$$\Delta\sigma_{dis} = M \cdot G \cdot \alpha \cdot b \cdot \rho^{1/2} \tag{14}$$

where M, G and b are defined as above, $\alpha = 0.3$ for FCC metals, and the dislocation density (ρ) is estimated from:

$$\rho = \frac{2\sqrt{3} \cdot \varepsilon}{d \cdot b} \tag{15}$$

where ε is extracted from Eq. (14), and d as defined previously. The calculated dislocation densities in the homogenized and aged states, are ρ = 1.9x10^{14} m^{-2} and ρ = 1.1x10^{14} m^{-2}, respectively leading to strength increases of $\Delta\sigma_{dis}$ = 99MPa and 75MPa, respectively. These high dislocation densities are comparable to those found in 7xxx Al alloys with ~1um grains[50,213,215]. Given that our samples are rapidly solidified under high thermal gradients, the high dislocation density, and thus significant dislocation strengthening, is expected.

(iv) Precipitate / dispersoid strengthening is governed by the Orowan dislocation bypassing mechanism, described as:[213,215].

$$\Delta\sigma_{\mathrm{orowan}} = M \frac{0.4 \cdot G \cdot b}{\pi\sqrt{1-\nu}} \cdot \frac{ln(\frac{2\bar{r}}{b})}{\lambda_{\mathrm{p}}} \tag{16}$$

with $G,\ b,\ M$ defined as above, and ν as the Poisson's ratio of the alloy (Table A2.1). Using the measured mean radius ($\bar{r}$) and mean inter-precipitate distance (λ_p) from TEM image analysis (Table 1.4), the total precipitate / dispersoid strengthening for the homogenized and aged condition are $\Delta\sigma_\mathrm{orowan} = 75$MPa and 232MPa, respectively. It is noted that HRTEM imaging (Figure A2.1) confirms the $MgZn_2$ precipitates to be incoherent, implying that the operative mechanism is indeed Orowan dislocation bypassing as opposed to dislocation shearing[218], the former being described by Eq. (16).

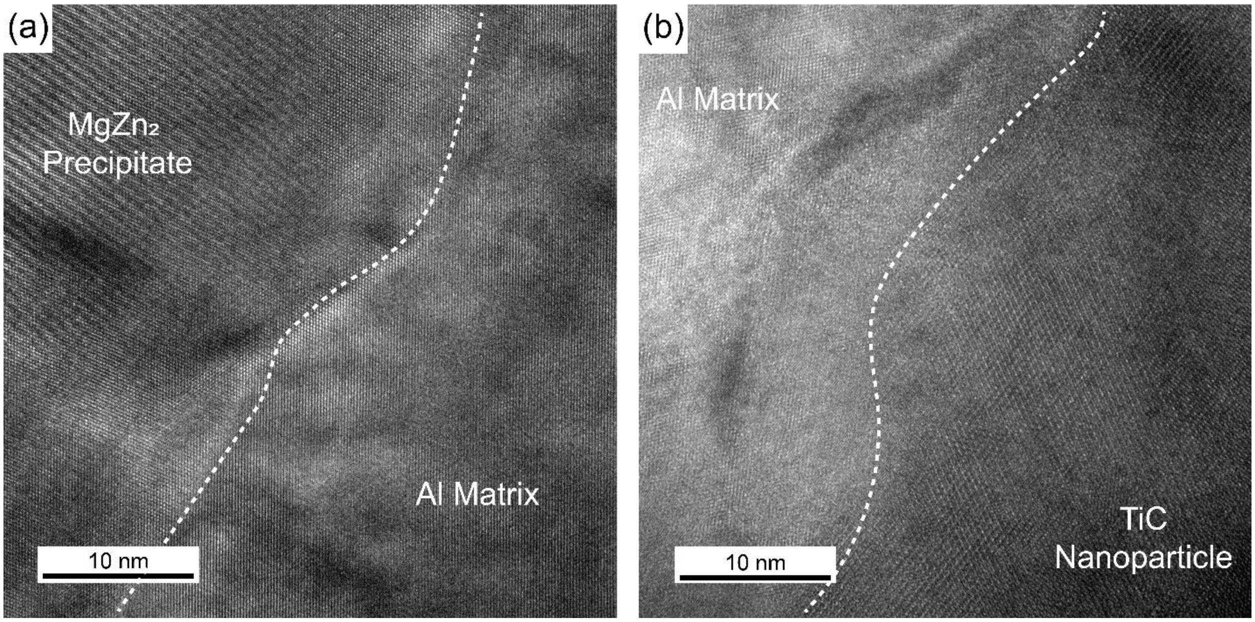

Figure A2.1. HRTEM of interfaces between (a) $MgZn_2$/FCC-Al and (b) TiC/FCC-Al.

The quantitative contributions of these four strengthening mechanisms are reported in Figure 1.14, in good agreement with experimental measurements.

Appendix 3. Finite Elements Analysis (FEA) Simulation of Thermal Histories

A finite element model is created to simulate the thermal history resulting from multiple laser scans and multiple build layers. The finite element method is chosen as the modeling technique of choice, due to its simultaneous ability to simulate a large amount of material with a sufficiently fine mesh, while still accounting for the most dominant heat transfer physics, including heat conduction through the material into the substrate and adjacent layers, radiation and convection to ambient, and latent heat of fusion/solidification. Higher fidelity models that include more specific physics such as the particle nature of the powder bed, Marangoni flow, material evaporation, or internal laser reflections in the melt pool, are not suitable for simulating large amounts of layers and laser scans. Experimental validation using melt pool dimensions and thermal cameras has shown that FEA is the most suitable modeling technique for simulating layer temperature [169,204,205,219].

Two samples are modeled, chosen as representative for fully martensitic microstructures (LED = 1.2 J/mm and VED = 400 J/mm^3) and dual-phase, ferritic/martensitic microstructures (LED = 0.3 J/mm and VED = 100 J/mm^3).

Table A3.1. Thermophysical properties and laser parameters used in simulations [5,220–222].

Density (ρ) @ 25°C	7800 kg/m^3	Heat of fusion (ΔH_{sl})	250 kJ
Density (ρ) @ 1500°C	6900 kg/m^3	Specific Heat (C_p) @ 25°C	600 J$/kg \cdot K$
Thermal Conductivity (κ) @ Thermal 25°C	25 $W/m \cdot K$	Specific Heat (C_p) @ 1500°C	1300 J$/kg \cdot K$
Thermal Conductivity (κ) @ Thermal 1500°C	70 $W/m \cdot K$	Convective Heat Transfer Coefficient	25 $W/m^2 \cdot K$
Laser Absorptivity	0.7	Emissivity	0.6
Ambient Temperature	25°C	Laser Power	200W
Laser Diameter	80μm	Laser Scan Speed	167, 667 mm/s
Hatch Spacing	100μm	Layer Thickness	30μm
Ambient Temperature	25°C		

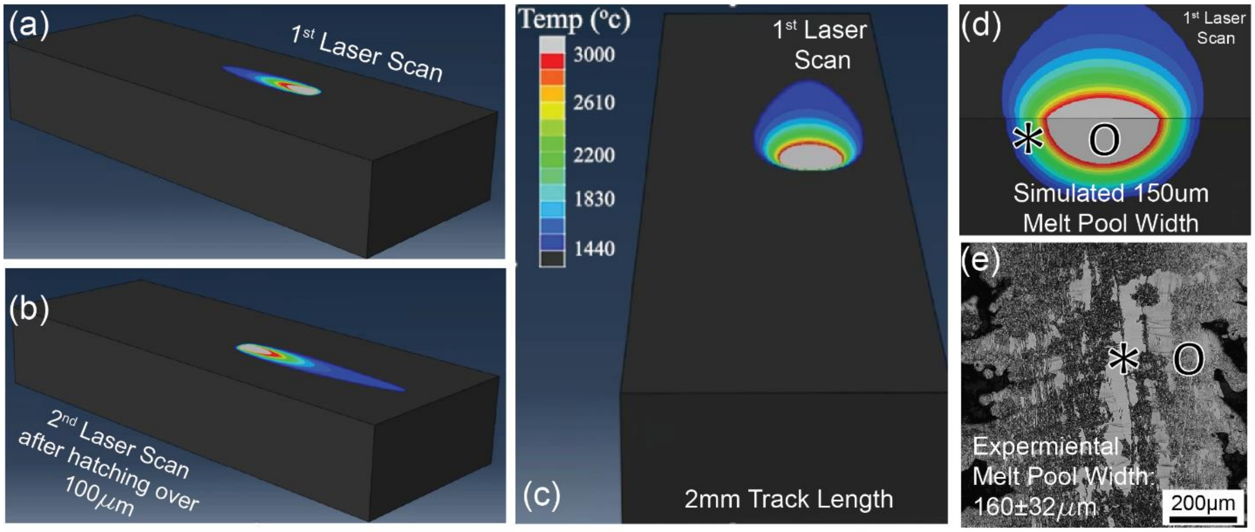

Figure A3.1 Overview of the dual scan simulation. (a) 1st laser scan (b) 2nd laser scan after hatched over 100µm. (c) Top view of the laser scan. (d) Cross-section of the melt pool, with the In-Track region directly in the track and the In-Hatch region in-between the 1st scan and 2nd scan, which would raster back on the left side in this point of view. (e) Experimental microstructure of the dual wall printed with energy density VED = 100 J/mm^3, consisting of a dual phase microstructure and corresponding In-Track and In-Hatch locations.

Finite element analysis (FEA) is performed with the Abaqus CAE software package. A customized DFLUX subroutine is used to create a moving Gaussian heat source, representing the laser. A 30µm build layer is initially deposited on the substrate. The laser scans over a length of 2mm, hatches over by 100µm, and subsequently scans back over the same 2mm length. The build plate is allowed to equilibrate for 1 sec (which is enough time to reach the build plate temperature of 200°C), before the second 30µm build layer is introduced and scanned with the same approach. This process is repeated for a total of 4 layers. The time for the DFLUX scanning steps are 6ms and 24ms, for the VED = 100 J/mm^3 and VED = 400 J/mm^3 samples, respectively, broken into 100 time steps. The mesh is biased from an element size of 3µm near the heat source to 30µm near the bottom of the base plate. A standard solid heat transfer linear brick (DC3D8) element is used for all simulations. Heat conduction, convection, and radiation are all accounted for in the simulation, with thermophysical values and print parameters reported in Table A3.1.

Thermophysical properties are temperature dependent to best account for the melting phase change, as well as laser absorptivity representative of the laser-powder interaction.

Temperature profiles from the simulations are reported in Figure A3.1, with thermal histories for the *In-track* and *In-hatch* regions of the two samples depicted in Figure 3.6. While the latent heat of evaporation is not included in the model, resulting in overprediction of the peak temperature upon melting, the rest of the thermal history is expected to be accurately predicted. To validate this statement, we compare predicted melt pool widths (Figure A3.d) with experimental observations (Figure A3.1e and Figure 3.2). The experimental melt pool widths of 158±20μm and 317±22μm for the VED = 100 J/mm^3 and VED = 400 J/mm^3 conditions, respectively, agree well with simulated values of 150μm and 290μm.

Appendix 4. From Thin Wall Samples to Larger Parts

While the simple dual-wall samples discussed in this work helped elucidate the mechanisms of phase evolution in 17-4 PH steel under LPBF, and in particular shed light on the localized appearance of ferrite exclusively in the *In-track* regions of low VED, low LED samples, the volume fraction of ferrite in all samples is significantly lower than reported in previous work [188], conducted on bulk samples consisting of dozens to hundreds of scan lines (for example, compare the microstructures depicted in Figure 3.1f with Figure 3.2h, obtained from samples printed with nearly identical values of LED and VED).

We attribute this discrepancy to the stochastic nature of certain physical phenomena (vaporization, spatter, balling, the discretized powder nature of the bed, Marangoni flow, etc.) occurring in the melt pool, and leading to noticeable differences across the same sample. This is highlighted in the dual-wall sample for LED = 0.3 J/mm and VED = 100 J/mm^3, shown in Figure

A4.2a (reproduced from Figure 3.2h): while columnar ferrite grains are observed in the *In-Hatch* region (in agreement with the microstructure of larger specimens (Figure 3.1f), they do not propagate through the entirety of the sample, with most of the *In-Hatch* region still consisting of martensite.

We surmise that these stochastic effects are amplified in small-scale samples, which are printed near the resolution of the machine, and become gradually less significant as sample size is increased. To support this interpretation, Figure A4.2 illustrates quad-wall samples printed with the same conditions as the dual-wall samples depicted in Figure 3.2. All quad-wall samples were printed with 4 laser scans, with the same 'borders inside-out' scan strategy used for bulk specimens from previous work [188]. The quad walls of the LED = 0.3 J/mm sample with hatch spacings of ≤50μm are still extremely thin as they are essentially remelted four times, without ever hatching beyond the size of the melt pool. Again, large amounts of lack-of-fusion porosity occur in the LED = 1.2 J/mm and VED = 67 and 100 J/mm^3, rendering these conditions useless in practicality. Notice that all microstructural observations on quad-wall samples (Figure A4.2) are in perfect agreement with those extracted from dual-wall samples (Figure 3.2), with only two conditions (LED = 0.3 J/mm with VED = 67 and 100 J/mm^3) yielding dual-phase microstructure with columnar ferrite observed.

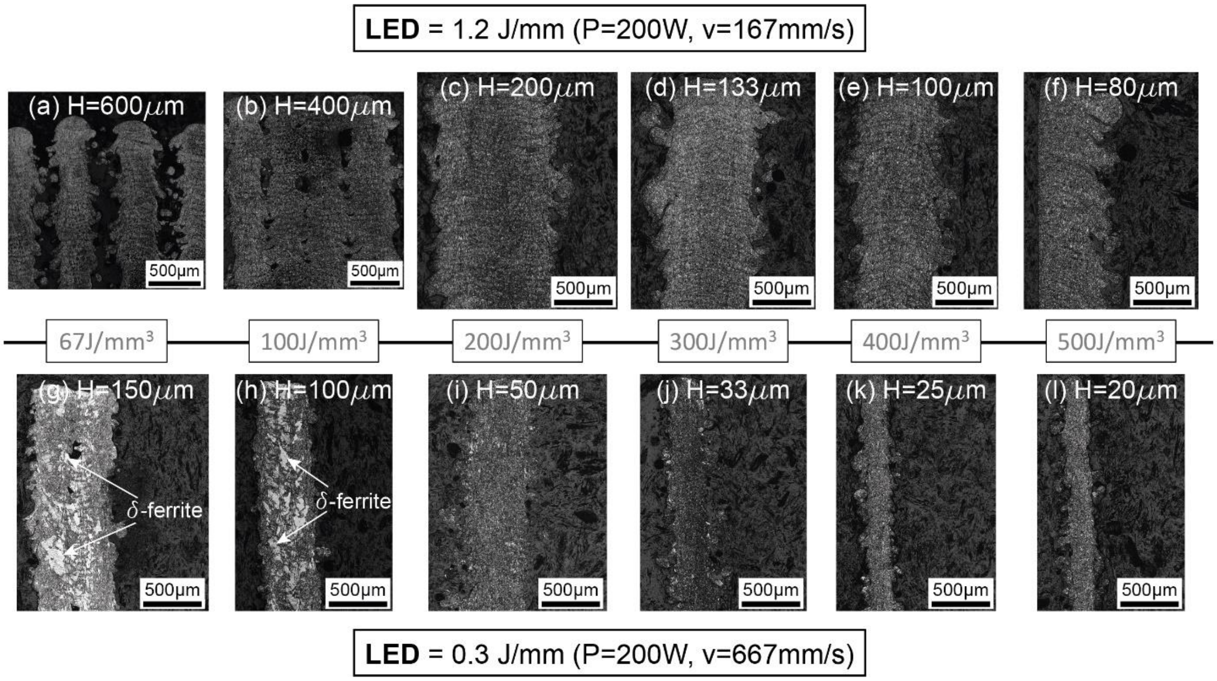

Figure A4.1. Effect of hatch spacing on Quad Walls, and thus VED, on (a) LED = 1.2 J/mm resulting in no columnar ferrite under any printing condition; and on (b) LED = 0.3 J/mm resulting in columnar ferrite forming under hatch spacings of 100 μm and 150μm.

However, there is a noticeably higher volume fraction ferrite in the quad-wall samples, compared to the dual-wall samples printed under the same conditions. This comparison is further illustrated in Figure A4.2, which also include a larger bulk sample composed of >20 walls. Image analysis shows that the volume fraction of ferrite increases with sample size, from 9% in the dual-wall sample, to 38% in the quad-wall sample and 68% in the bulk specimen. It should also be noted that each sample in Figure A4.2, is printed with the “Borders Inside-Out” scan strategy in which concentric borders are printed next to each other until the final outer outline. The outer border (and thus the final scan) for each part in Figure A4.2, is composed of martensite, as initially observed in our previously study [188]. Another reheating cycle is added for each adjacent layer printed. Thus, while the larger parts consistently have more ferrite, they still do not have ferrite at the border under any processing conditions.

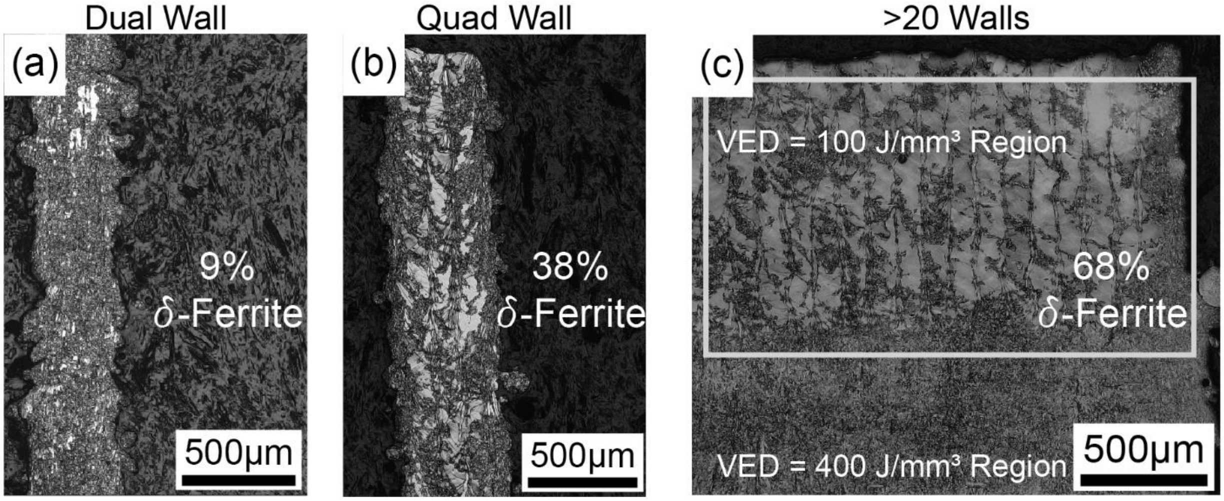

Figure A4.2 Evolution of ferrite phase fraction through (a) single walls (b) dual walls (c) quad walls) and (d) a full part with permission from reference [188]